FFI RAPPORT

SIMVEX 2001 TRIAL - RADIANT INTENSITY CONTRAST

STARK Espen, HEEN Lars Trygve, WIKAN Kjell

FFI/RAPPORT-2002/02568

FFIE/801/131

Approved
Kjeller 12th June 2002

Stian Løvold
Director of Research

SIMVEX 2001 TRIAL - RADIANT INTENSITY CONTRAST

STARK Espen, HEEN Lars Trygve, WIKAN Kjell

FFI/RAPPORT-2002/02568

FORSVARETS FORSKNINGSINSTITUTT
Norwegian Defence Research Establishment
P O Box 25, NO 2027 Kjeller, Norway

FORSVARETS FORSKNINGSINSTITUTT(FFI)
Norwegian Defence Research Establishment

P O BOX 25
NO 2027 KJELLER, NORWAY

UNCLASSIFIED

SECURITY CLASSIFICATION OF THIS PAGE
(when data entered)

REPORT DOCUMENTATION PAGE

1) PUBL/REPORT NUMBER	2) SECURITY CLASSIFICATION	3) NUMBER OF PAGES
FFI/RAPPORT-2002/02568	UNCLASSIFIED	131
1a) PROJECT REFERENCE	**2a) DECLASSIFICATION/DOWNGRADING SCHEDULE**	
FFIE/801/131		

4) TITLE

SIMVEX 2001 TRIAL - RADIANT INTENSITY CONTRAST

5) NAMES OF AUTHOR(S) IN FULL (surname first)

STARK Espen, HEEN Lars Trygve, WIKAN Kjell

6) DISTRIBUTION STATEMENT

Approved for public release. Distribution unlimited. (Offentlig tilgjengelig)

7) INDEXING TERMS

IN ENGLISH	IN NORWEGIAN
a) Infrared signature	a) Infrarød signatur
b) Ship signature modelling	b) Signaturmodellering
c) Infrared measurements	c) Infrarøde målinger

THESAURUS REFERENCE:

8) ABSTRACT

FFI project 801 “IR-missiles” participated in the SIMVEX (Ship Infrared Model Validation EXperiment) trial organized by NATO RTO/SET/TG16 “Infrared measurements and modeling for ship self defense” in September 2001 in Halifax, Canada. The aim of the trial was to evaluate the ship signature model ShipIR/NTCS and to evaluate and improve the methodology used by the participating countries. A complete ShipIR/NTCS model of the unclassified target ship, CFAV Quest, was distributed to all participating countries. The main FFI instrumentation included a spectroradiometer, two IR cameras, blackbodies, two weather stations, and a GPS system transmitting the ship position to the shore station. This report contains results on apparent radiant intensity contrast obtained during the SIMVEX trial using an MW and an LW infrared camera, and also presents parts of the weather data. Apparent radiant intensity contrast results are compared with predictions from the ShipIR/NTCS model for selected runs. In addition, ShipIR/NTCS temperature predictions are compared with on-board temperature sensor readings for these runs. The quality of the weather data obtained during the trial is believed to be good, while the image data is of more varying quality. The comparison with the model results indicates that the model overpredicts the apparent radiant intensity contrast and temperatures for the day runs and underpredicts for the night runs.

9) DATE	AUTHORIZED BY This page only	POSITION
12th June 2002	Stian Løvold	Director of Research

ISBN-82-464-0620-5

UNCLASSIFIED

SECURITY CLASSIFICATION OF THIS PAGE
(when data entered)

CONTENTS

PAGE

SIMVEX 2001 TRIAL - RADIANT INTENSITY CONTRAST

1 INTRODUCTION

In September 2001 project 801 at FFI, IR-missiles, participated in the SIMVEX trial (Ship Infrared Model Validation EXperiment) in Halifax, Canada. FFI (Espen Stark) has been a member of the NATO RTO/SET/TG16 group; "Infrared measurements and modeling for ship self defense" since year 2000. This group was organizing the SIMVEX trial. The TG16 group (and its predecessors TG06, RSG-5, and RSG-8) has selected the ship signature model ShipIR/NTCS as a NATO standard. As a member of this group, the project has received the ShipIR model and has started using it for generation of synthetic infrared images of ships and backgrounds.

For several years, the participating countries in TG16 have been exchanging validation data and results on the ShipIR model. This has resulted in a demonstrable improvement in prediction accuracy of the model. The project has contributed to this work with spectral measurements of ship plume signatures. The plume measurements were obtained during the NATO SWG/4 EW Trial in Stavanger, Norway in August 1999 (1). The improved ShipIR model will predict the ship signature more accurately under various conditions. On board a military ship with sufficient computing power this could provide real time information on the ship's vulnerability to threat IR sensors (e.g incoming missiles with infrared seekers). The improved model will also provide more accurate information on the IR signature of a ship under design, or for an existing ship on the success of passive IR countermeasures in a set of standard environmental conditions.

The SIMVEX trial had two objectives:

1. Comparison of radiometric measurements from the various participating NATO countries in order to validate their methodology.
2. Collection of high quality UNCLASSIFIED radiometric data on a test ship for subsequent collaborative validation of the ShipIR model.

If measurements obtained by different countries do not agree, one can not assume the model to agree with the measurements. To fully understand the comparison, it is important that the same quantities are compared. During the trial, comparisons were performed on a panel painted with high emissivity paint, and for the ship, CFAV Quest.

The quantities to be compared during the trial were; 3–5 μm and 8–12 μm equivalent blackbody temperature (corrected for atmosphere, e.g temperature at the target plane) for the panel comparisons.

For the ship, 3–5 μm and 8–12 μm equivalent blackbody temperature of a part of the port hull was compared. In addition, the full-ship apparent radiant intensity contrast (not corrected for atmosphere) was calculated from the measured IR-images. The apparent

radiant intensity contrast is not wholly comparable between different sensors due to differences in optical bandwidth. However, the results of different nations will be compared to some extent.

For the trial, a ship named CFAV Quest was made available by Canada. CFAV Quest is a research vessel belonging to the Defence Research & Development Canada Atlantic (DRDCA) in Halifax. The ship normally does acoustic, hydrographic and general oceanographic work. Figure 1.1 shows an image of the ship.

Figure 1.1 Image of the test ship, CFAV Quest.

Chapter 2 of this report describes the methodology used by FFI to calculate both the equivalent blackbody temperature at the target and the apparent radiant intensity contrast at the sensor. In chapter 3 a description of the measurements FFI performed is given. This chapter also gives results based on IR images. Chapter 4 describes ShipIR simulations that have been performed, and presents the results of the simulations and comparisons with the measurements. A summary of the work with some suggestions for future work is given in chapter 5.

Appendix A presents a simplification of an equation presented in chapter 2. In appendix B a list of all the runs performed during the SIMVEX trial is given. The meteorological data recorded by FFI during the trial is presented in appendix C. Measurements of the reflectance of the two different paints on the ship were performed in advance of the trial, these results are presented in appendix D. A list of all the figures and tables presented in this report is given in appendix E.

2 THEORY

This chapter presents the theory for calculation of the target total radiant intensity in the target plane, and the apparent radiant intensity contrast as measured by the sensor. A method for finding the equivalent blackbody temperature is given, and this temperature is used to calculate the radiant intensity. Further, a method is presented where the equivalent blackbody temperature is used to calculate the radiant intensity contrast using a virtual

spectral response. This virtual spectral response is slightly different than the spectral response of the camera the measurement is performed with. The sensor in this report is assumed to be an infrared camera using a staring focal plane array.

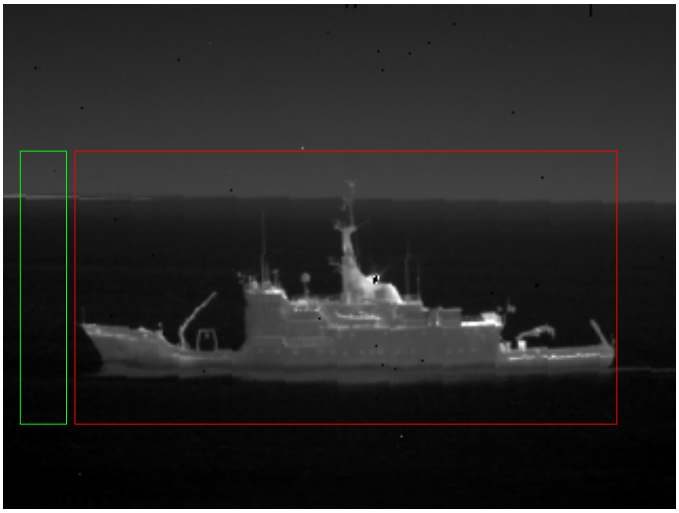

Figure 2.1 Illustration of scene with target area marked with red, and background area marked with green. Illustration image recorded by NRL with Indigo Merlin (MW) IR camera.

Figure 2.1 gives an example of a scene with a defined target area (red and background area (green). In addition to this scene, two blackbody sources at known temperatures are needed to calculate radiant intensity contrast or equivalent blackbody temperature.

2.1 Equivalent blackbody temperature

In this section a method to find the equivalent blackbody temperature is given. The definition of equivalent blackbody temperature in this context is the temperature of a blackbody which has a radiance $[W/cm^2sr]$ (within the sensor's optical bandwidth) equal to the radiance from the target at the target location. This means that the measurement must be corrected for the influence of the atmosphere between camera and target.

The signal received at the sensor from one target pixel is given by:

$$S_{tgt} = S_0(T_s, t_i, O_{TIA}) + A_s\,\Omega_s \int_0^\infty \left\{N_{tgt}(\lambda)\tau_{atm}(\lambda, x_t) + N_{atm}(\lambda, x_t)\right\} R_s(\lambda)\,d\lambda \quad (2.1)$$

where

S_0	-	Camera DC-offset
T_s	-	Operational temperature, $[K]$
t_i	-	Integration time, $[s]$
O_{TIA}	-	Pre-amplifier offset
A_s	-	Area of camera aperture, $[cm^2]$
Ω_s	-	Instantaneous field of view (solid angle) (IFOV), $[sr]$
$N_{tgt}(\lambda)$	-	Radiance from the target (emitted plus reflected), $[W/cm^2 sr\ \mu m]$
τ_{atm}	-	Atmospheric transmittance
$N_{atm}(\lambda, x_t)$	-	Radiance from the path between sensor and target, $[W/cm^2 sr\ \mu m]$
x_t	-	Range to target, $[m]$
$R_s(\lambda)$	-	Camera spectral responsivity

The spectral responsivity for the infrared sensor referred to the A/D-converter's output is given by:

$$R_s(\lambda) = \tau_s(\lambda)\, R_d(\lambda)\, G(t_i, O_{TIA})\, F(t_i, O_{TIA}) \tag{2.2}$$

where

$\tau_s(\lambda)$	-	System transmittance
$R_d(\lambda)$	-	Spectral responsivity of the detector
G	-	Electronic gain
F	-	Sensitivity of A/D-converter

The camera spectral responsivity in equation (2.2) can be written as:

$$R_s(\lambda) = R_s\, r_s(\lambda) \tag{2.3}$$

where

$r_s(\lambda)$	-	Relative spectral responsivity
R_s	-	Maximum spectral responsivity

The spectral radiance from the atmosphere between the target and the sensor (assuming horizontal path with constant temperature) is given by:

$$N_{atm}(\lambda, x_t) = (1 - \tau_{atm}(\lambda, x_t))\ N_{bb}(\lambda, T_{atm}) \tag{2.4}$$

where

T_{atm}	-	Atmospheric temperature
x_t	-	Range to target

and $N_{bb}(\lambda, T)$ is the spectral radiance $[W/cm^2 sr\ \mu m]$ from a blackbody:

$$N_{bb}(\lambda, T) = \frac{2\, c^2 h}{\lambda^5 \left(e^{\frac{hc}{k_b \lambda T}} - 1 \right)} \tag{2.5}$$

where

T	-	temperature $[K]$
c	-	vacuum speed of light, $3 \cdot 10^8\, m/s$
h	-	Planck's constant, $6.63 \cdot 10^{-34}\, Ws^2$
k_b	-	Boltzmann's constant, $1.38 \cdot 10^{-23}\, Ws/K$

Equation (2.1) can be simplified:

$$S_{tgt} = S_0(T_s, t_i, O_{TIA}) + K \int_0^\infty \left\{ N_{tgt}(\lambda)\tau_{atm}(\lambda, x_t) + N_{atm}(\lambda, x_t) \right\} r_s(\lambda)\, d\lambda \tag{2.6}$$

where

K - Camera constant, $K = A_s\, \Omega_s\, R_s$

To utilize these equations, the camera in use must be calibrated (i.e S_0, K, and $r_s(\lambda)$ must be known). A method for spectral and radiometric calibration is given in (2).

If the relative spectral responsivity of the camera is known, two blackbodies can be used during the measurement to find the missing parameters. The two blackbodies are radiating at known temperatures, T_a and T_b, at a distance of x_r. The difference between the measured signals from the two blackbodies is (refer to equation (2.6)):

$$S_a - S_b = K \int_0^\infty \{\epsilon_a(\lambda)\, N_{bb}(\lambda, T_a) - \epsilon_b(\lambda)\, N_{bb}(\lambda, T_b)\}\, \tau_{atm}(\lambda, x_r)\, r_s(\lambda)\, d\lambda \tag{2.7}$$

where $\epsilon_a(\lambda)$ and $\epsilon_b(\lambda)$ are the emissivities of the two blackbodies.[1]

From equation (2.7) the camera constant, K, is found easily. The atmospheric transmittance is calculated using MODTRAN (3). S_0 is now given by:

$$S_0(T_s, t_i, O_{TIA}) = S_a - K \int_0^\infty \{\epsilon_a(\lambda) N_{bb}(\lambda, T_a)\tau_{atm}(\lambda, x_r) + N_{atm}(\lambda, x_r)\}\, r_s(\lambda)\, d\lambda \tag{2.8}$$

The target radiance (within the sensor's optical bandwidth) at the sensor's position is:

$$\int_0^\infty N_{tgt}(\lambda)\, \tau_{atm}(\lambda, x_t)\, r_s(\lambda)\, d\lambda = \frac{S_{tgt} - S_0}{K} - \int_0^\infty N_{atm}(\lambda, x_t)\, r_s(\lambda)\, d\lambda \tag{2.9}$$

The equivalent temperature, T_{eq}, of a blackbody (with $\epsilon = 1$) giving the same radiance is determined by solving the following equation numerically with respect to T_{eq}:

$$\int_0^\infty N_{bb}(\lambda, T_{eq})\, \tau_{atm}(\lambda, x_t)\, r_s(\lambda)\, d\lambda = \frac{S_{tgt} - S_0}{K} - \int_0^\infty N_{atm}(\lambda, x_t)\, r_s(\lambda)\, d\lambda \tag{2.10}$$

In equation (2.10) the spectral radiance from the atmosphere is given by equation (2.4).

Since the target emissivity generally is less than unity, the spectral radiance from the target is a sum of emitted and reflected radiation. The calculated equivalent temperature from equation (2.10) may therefore be affected by other sources than the target temperature.

If the equivalent blackbody temperature is close to the atmospheric temperature, equation (2.10) can be simplified. This is presented in appendix A. The simplification gives an equation that can be solved explicitly, but in most cases the equation is still solved by a computer and the more accurate equation (2.10) is preferred.

[1] The emissivities $\epsilon_a(\lambda)$ and $\epsilon_b(\lambda)$ must either be equal to or very near unity in order to disregard reflected radiation.

2.2 Radiant intensity in the target plane

The radiant intensity in the target plane is defined as the total radiance from the target, corrected for the atmosphere between the sensor and the target.

When the equivalent blackbody temperature of one pixel is found, by solving equation (2.10) or (A.4), the radiant intensity $[W/sr]$ in the target plane of that pixel can be found:

$$J_{tp} = \Omega_s {x_t}^2 \int_0^\infty N_{bb}(\lambda, T_{eq})\, r_s(\lambda)\, d\lambda \tag{2.11}$$

The total radiant intensity of the target is found by adding all pixels belonging to the target.

$$J_t = \sum_{p=1}^{N} J_{tp} \tag{2.12}$$

The above method is used when the radiant intensity of the target is to be found. If the radiant intensity contrast at the target plane was to be found, the radiant intensity from the background should be subtracted.

2.3 Apparent radiant intensity contrast

The apparent radiant intensity contrast is defined as the total radiance difference between the target and the background, received at the sensor. The apparent radiant intensity contrast is *not* corrected for the influence of the atmosphere.

The calculation of the apparent radiant intensity contrast at the sensor is a much easier task than computing the radiant intensity at the target plane. The method described below is identical to one suggested in (4). The scene is still defined as in figure 2.1. The target is outlined by a rectangular box including *all* target pixels, and it may also include background pixels.

In the previous section the target pixel signal was described by equation (2.6). In this section we want to find the apparent radiant intensity contrast at the sensor. The radiance received by one pixel, $N_{rec,tgt}(\lambda)$, can be written as:

$$N_{rec,tgt}(\lambda) = N_{tgt}(\lambda)\, \tau_{atm}(\lambda, x_t) + N_{atm}(\lambda, x_t) \tag{2.13}$$

The difference in signal (contrast) between a target pixel and a background pixel is now given by:

$$S_{tgt} - S_{bkg} = K \int_0^\infty \left\{ N_{rec,tgt}(\lambda) - N_{rec,bkg}(\lambda) \right\} r_s(\lambda)\, d\lambda \tag{2.14}$$

The radiant intensity contrast for one pixel is defined as:

$$J_{cp} = \Omega_s\, {x_t}^2 \int_0^\infty \left\{ N_{rec,tgt}(\lambda) - N_{rec,bkg}(\lambda) \right\} r_s(\lambda)\, d\lambda = \frac{\Omega_s\, {x_t}^2 \left(S_{tgt} - S_{bkg} \right)}{K} \tag{2.15}$$

The total apparent radiant intensity contrast is found by adding all pixels in a rectangle surrounding the target:

$$J_c = \sum_{p=1}^{M_{tgt}} J_{cp} \tag{2.16}$$

where

M_{tgt} - number of pixels in rectangle surrounding target

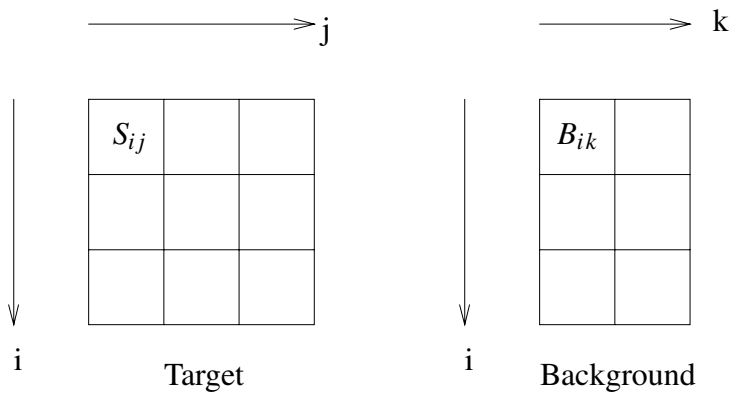

Figure 2.2 Definition of background and target pixels.

In figure 2.2 an outline of how the target and background area are defined is given. The signal from a pixel in the target box is called S_{ij}, and the signal from a pixel in the background box is called B_{ik}. The range in elevation must be exactly the same for the target and background boxes. Assuming a horizontally uniform background, the subtracted background for each target pixel will be the mean value of the background line, $\overline{B_i}$, from the same line as the target pixel. The apparent radiant intensity contrast for target pixel (i, j) is then given by:

$$J_{cij} = \frac{\Omega_s \, {x_t}^2 \, \left(S_{ij} - \overline{B_i}\right)}{K} = \frac{\Omega_s \, {x_t}^2 \, \left(S_{ij} - \frac{1}{M_k} \sum_k B_{ik}\right)}{K} \tag{2.17}$$

where

M_k - number of pixels in each background line

From equation (2.16) the total apparent radiant intensity contrast is given by:

$$J_c = \sum_{p=1}^{M_{tgt}} J_{cp} = \sum_{ij} J_{cij} \tag{2.18}$$

This gives:

$$J_c = \frac{\Omega_s \, {x_t}^2}{K} \sum_{ij} \left\{ S_{ij} - \frac{1}{M_k} \sum_{k} B_{ik} \right\} \tag{2.19}$$

$$= \frac{\Omega_s \, {x_t}^2}{K} \left\{ \sum_{ij} S_{ij} - \frac{M_j}{M_k} \sum_{ik} B_{ik} \right\}$$

$$= \frac{\Omega_s \, {x_t}^2}{K} \left\{ \sum_{ij} S_{ij} - \frac{M_{tgt}}{M_{bkg}} \sum_{ik} B_{ik} \right\}$$

$$= \frac{\Omega_s \, {x_t}^2 \, M_{tgt} \left(\overline{S} - \overline{B} \right)}{K} \tag{2.20}$$

where

M_i	-	number of lines
M_j	-	number of pixels in each target line
M_k	-	number of pixels in each background line
$M_{tgt} = M_i \, M_j$	-	number of pixels in target area
$M_{bkg} = M_i \, M_k$	-	number of pixels in background area

The equation to be used to calculate the apparent radiant intensity contrast, J_c, is thus given by:

$$J_c = \frac{\Omega_s \, {x_t}^2 \, M_{tgt} \left(\overline{S} - \overline{B} \right)}{K} \tag{2.21}$$

2.4 Virtual radiant intensity

During the SIMVEX trial, measurements were performed by several countries simultaneously. The apparent radiant intensity contrast obtained by the various participants is not directly comparable due to the differences in the spectral response of cameras. In order to compare the results obtained by the different countries, a way to scale the results from the spectral band of each separate measurement to a virtual band is needed.

Figure 2.3 illustrates the spectral response of the Inframetrics MilCam camera used by FFI during the trial, a typical transmittance curve for a 1 km path, and a virtual spectral response. The idea is to transfer the measurements from the original spectral response to the new virtual response. The virtual response indicated in figure 2.3 is 1 between 3.0 μm and 5.0 μm.

From equation (2.10) the equivalent blackbody temperature, T_{eq}, can be found for each pixel. By using this equivalent blackbody temperature and applying a virtual spectral response, $r_{s,virt}(\lambda)$, to equation (2.11), the radiant intensity of one pixel is found:

$$J_{tp} = \Omega_s \, {x_t}^2 \int_0^\infty N_{bb}(\lambda, T_{eq}) \, r_{s,virt}(\lambda) \, d\lambda \tag{2.22}$$

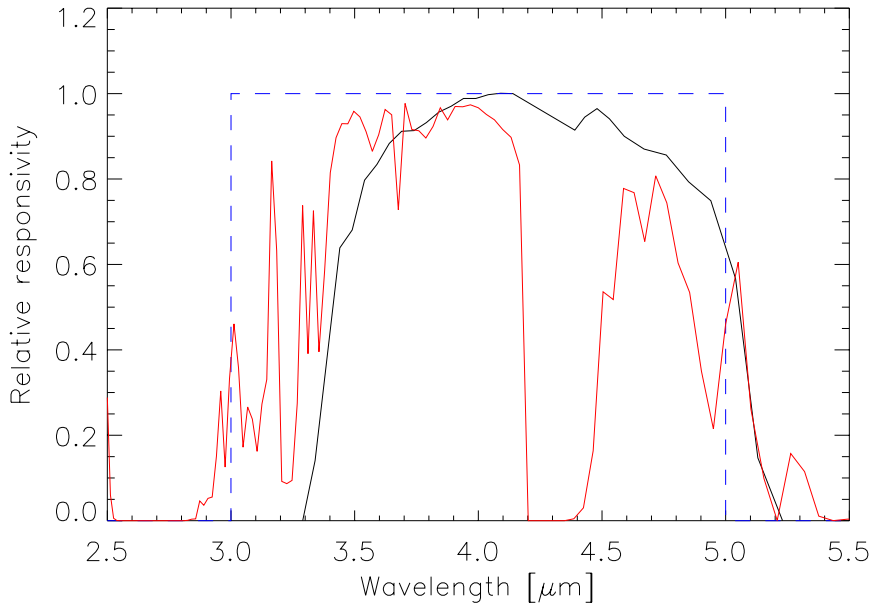

Figure 2.3 Spectral responsivity for MilCam IR sensor (black) and virtual response (blue). The red line indicates a typical transmittance of a 1 km atmospheric path.

Using equation (2.12) the total radiant intensity of the target, J_t, is found:

$$J_t = \sum_{p=1}^{N} J_{tp} \tag{2.23}$$

where

N - Number of pixels in the outlined target

To find the virtual radiant intensity contrast, a background must be defined. This background is typically the sea or the sky just above the horizon, at the same distance as the ship. Assuming this background has an equivalent blackbody temperature, $T_{eq,bck}$, the radiant intensity from a one pixel background can be found:

$$J_{bck,p} = \Omega_s \, {x_t}^2 \int_0^\infty N_{bb}(\lambda, T_{eq,bck}) \, r_{s,virt}(\lambda) \, d\lambda \tag{2.24}$$

The virtual radiant intensity contrast is now defined as:

$$J_{vc} = J_t - \sum_{p=1}^{N} J_{bck,p} = J_t - N \, J_{bck,p} \tag{2.25}$$

The equivalent blackbody temperature of the sea background can be found for an area close to the ship for a sea background. For the sky just above the horizon the atmospheric temperature can be used. This very simple method to define the background is used due to

the difficulties involved in finding the equivalent blackbody temperature to a complete vertical background profile in an image. Usually the distance to the ship is known, and the equivalent blackbody temperature can be found, refer to equation (2.10). For a vertical background profile the distance to each background pixel varies and is not known. The background is thus defined in one of two ways; using a small sea background near the ship (probably at the same distance as the ship), or the sky just above the horizon (atmosphere temperature).

To use this method to compare different results from the different measurement teams, it is important that the background is defined in the same manner. An example of a virtual band calculation is given in section 3.3.

3 MEASUREMENTS

The measurements were performed at the FMF Cape Scott test facility (NESTRA) at Osborne Head (near Halifax), Canada. The time period for the test was September 6–21 2001. This includes the time spent on mounting of the equipment and packing. The participating countries were: Canada, USA, France, Italy, Poland, Denmark, The Netherlands, and Norway. Figure 3.1 shows the facility with all the different measurement teams in position.

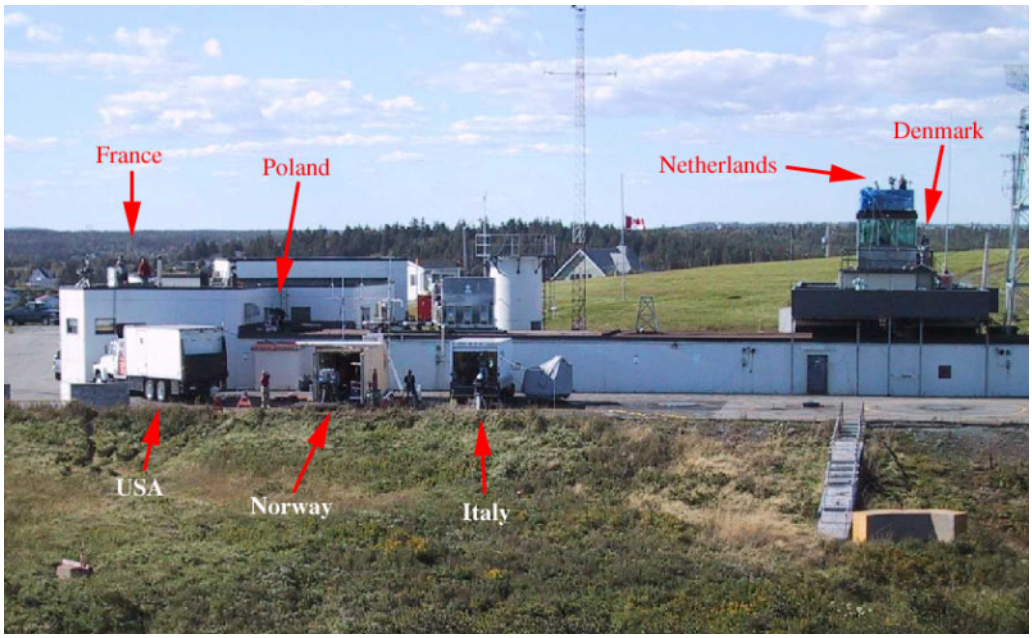

Figure 3.1 The NESTRA facility at Osborne Head, with all the different measurement teams in position.

Each country (except Canada) contributed with different IR cameras for the measurement. Canada contributed with the test site, and the ship to be measured. The ship used was CFAV Quest, this ship is used by DRDCA. Canada equipped the ship with a meteorology station and a lot of temperature sensors for ship surface temperature measurements. Several thermocouples were mounted on the ship and a gas analyzer was rented for plume

measurements. The instrumentation on board the ship is described in (5). FFI provided a GPS system, capable of transmitting the position to the shore site. At the shore site the position was distributed to all measurement stations through the local area network at NESTRA.

3.1 Run geometry

During the trial, mainly four different types of runs were performed (see figure 3.2). For all four types of runs the ship sailed with a constant speed and heading for 30 minutes before the point of closest approach (see table 3.1), where the measurements ideally should be taken. This point is on a 1 km arc from the measurement station, and is marked on the map in figure 3.2. The NESTRA waypoint in table 3.1 is actually the position of the FFI instrumentation. The ship used a speed of 10 knots, which means that the ship started 5 Nm from the point of closest approach. The reason for using a constant speed and heading for 30 minutes, was to allow the ship to reach thermal equilibrium before the measurement was taken.

The different run types were:

- Type A. In a type A run the heading of the ship was 270 (west). The starboard side of the ship was measured, and it was in shaded conditions. These runs were performed approximately 18:30 UTC. A total of 4 runs performed.
- Type B. In a type B run the heading of the ship was 0 (north). The port side of the ship was measured, in sunlit conditions. These runs were performed approximately 17:00 UTC. A total of 5 runs performed.
- Type C. In a type C run the heading of the ship was 32 (north-east). The port side of the ship was measured, in sunlit conditions. These runs were performed approximately 21:00 UTC. A total of 8 runs performed.
- Type D. A type D run was identical to a C run, except that the ship made a turn and passed the measuring point in the other direction as well. The heading of the ship was 32 and 212. This means that both the port and starboard side were measured, during night-time conditions at approximately 23:30 and 00:30 UTC. A total of 13 runs performed.

In addition to these run types, a few other runs were performed. Two different types of plume runs were performed; at the shore site and off-shore. The shore site runs were performed similar to a type D run, but using a different power setting. The off-shore runs were measured by the US team using a helicopter, different power settings for the engines were used. A run testing a panel with different paints for Defence Research & Development Canada Valcartier (DRDCV)[1] was also performed. A list of all the runs is presented in appendix B.

Figure 3.3 shows the position of the sun on September 17 at Osborne Head.

[1]Prior to April 1 2002 the name was Defence Research Establishment Valcartier (DREV).

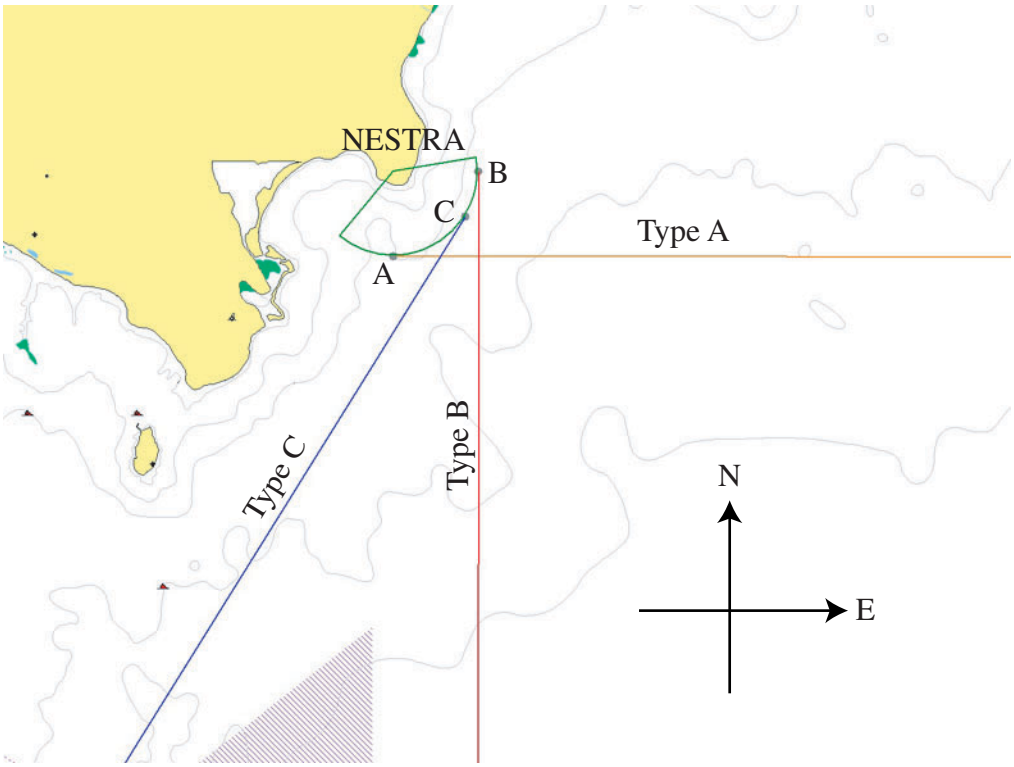

Figure 3.2 Map of measurement area with indication of the three different tracks and waypoints.

Waypoint	Latitude	Longitude
NESTRA	$44°36.720'N$	$63°25.317'W$
A	$44°36.187'N$	$63°25.317'W$
B	$44°36.727'N$	$63°24.559'W$
C	$44°36.441'N$	$63°24.674'W$

Table 3.1 Waypoints used during the trial.

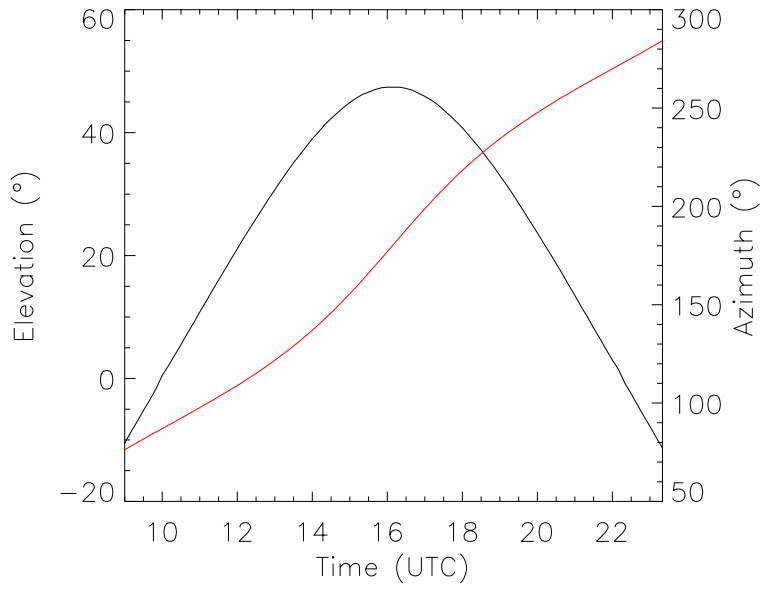

Figure 3.3 Position of the sun on September 17 at Osborne Head. Black line: elevation, red line: azimuth.

3.2 Instrumentation

The equipment that was supposed to be used during the SIMVEX trial is described in detail in (6). An Amber Aurora IR camera was supposed to be our main camera. Unfortunately, this camera broke down before the trial, and was not repaired in time for the trial. As a replacement for this camera an Inframetrics MilCam MW (3–5 μm) camera, was kindly provided to FFI by Naval Research Laboratory (NRL). The camera had an InSb detector with 256 $\times$ 256 pixels and the field of view was 4.4°. The camera had video output only (PAL format). The images were recorded on DVCAM video tape, and some images were digitized from the DVCAM system. The relative spectral response of the camera is shown in figure 2.3.

In addition to this camera we used an Amber Sentinel camera. This camera is an uncooled microbolometer LW (8–12 μm) camera. The detector size is 320 $\times$ 240 pixels. The relative spectral response has not yet been measured for this camera. The calculations in this report assume a spectral response equal to 1 from 8 to 12 μm. A photo of the two cameras is shown in figure 3.4.

In addition to the infrared cameras, FFI operated a Bomem DA5 FTIR spectroradiometer. With this spectroradiometer spectral measurements of the plume, locations on the ship hull, and background measurements (sea and sky) were performed. These results will be presented in a separate report (7).

As described in chapter 2, two blackbodies are used to find the camera constant, K, which is needed to find the apparent radiant intensity contrast. Recordings of the two blackbodies were made shortly before and after the run. The settings of the camera were not altered during this time period (approximately 8 minutes).

Figure 3.4 Amber Sentinel (LW) camera to the left, and Inframetrics MilCam (MW) camera to the right.

The temperatures of the two blackbodies were adjusted to fit the expected scene radiation. The Inframetrics MilCam camera was assumed to be fairly stable, so that we might use either one of the blackbody recordings. Analysis has shown that this is not the case, during an 8 minute period there is a fairly large drift in the camera. An example of pixel levels is shown in table 3.2. This example is valid for run 8, but the effect is similar in all runs.

	Hot BB $25°C$	Cold BB $15°C$
Image 1	142.7	46.4
Image 2 (8 min later)	155.6	56.0

Table 3.2 Blackbody calibration readings (mean pixel values) for run 8, Inframetrics MilCam (MW) camera.

The best way to avoid problems like these is to have the blackbodies present in the image at all times. This was not possible during this trial. For image analysis in this report, a linear interpolation between the two blackbody measurements will be used to fit the calibration to the time of the analyzed image. This unstability of the camera will increase the measurement error, see section 3.4.

The Amber Sentinel camera is even more unstable than the MilCam camera. The camera is very sensitive to heating (sun) of the optics. The camera must be recalibrated frequently to

give good images. It is not possible to recalibrate during a run, if the settings of the camera should be kept during the run. For the daytime runs it seems that none of the recordings with the Sentinel camera are valid, due to this unstability. Table 3.3 shows the pixel levels for the two black-bodies for the Sentinel camera during run 8.

	Hot BB $25°C$	Cold BB $15°C$
Image 1	122.8	43.4
Image 2 (8 min later)	201.4	121.1

Table 3.3 Blackbody calibration readings (mean pixel values) for run 8, Amber Sentinel (LW) camera.

The drift in the Sentinel camera does not seem to be linear, so it is difficult to make an interpolation similar to the one performed for the MilCam camera.

	Hot BB $17°C$	Cold BB $13°C$
Image 1	120.6	81.3
Image 2 (8 min later)	135.6	95.3

Table 3.4 Blackbody calibration readings (mean pixel values) for run 34, Amber Sentinel (LW) camera.

For the night time recordings, the drift is much smaller, see table 3.4.

In addition to the cameras used by FFI, several other countries had different types of IR cameras. The following countries participated with one or more IR cameras: USA, Italy, Denmark, The Netherlands, Poland, and France. USA used an Indigo Merlin MW IR camera during the trial. Some calculations based on images from this camera will be presented in this report. The spectral response for the camera is presented in figure 3.5. The camera has a 320×256 pixel InSb detector (320×240 pixels used), and the instantaneous field of view is $8.35 \cdot 10^{-8}\, sr$.

3.3 Apparent radiant intensity contrast calculations

In this section, the results from the analysis of apparent radiant intensity contrast is presented. Two of the runs are analyzed and presented in more detail. The first one is run 8, which is a type B run, performed during daytime on September 14. The second one is run 34, which is a type D run, performed during night-time on September 19.

The results are based on images from three different IR cameras; the MilCam MW camera, the Sentinel LW camera, and the Indigo Merlin MW camera.

For comparison, results from the two Italian cameras (MW and LW) are also included for run 8 and 34. The calculation on the Italian images are performed by Mariteleradar (8). The

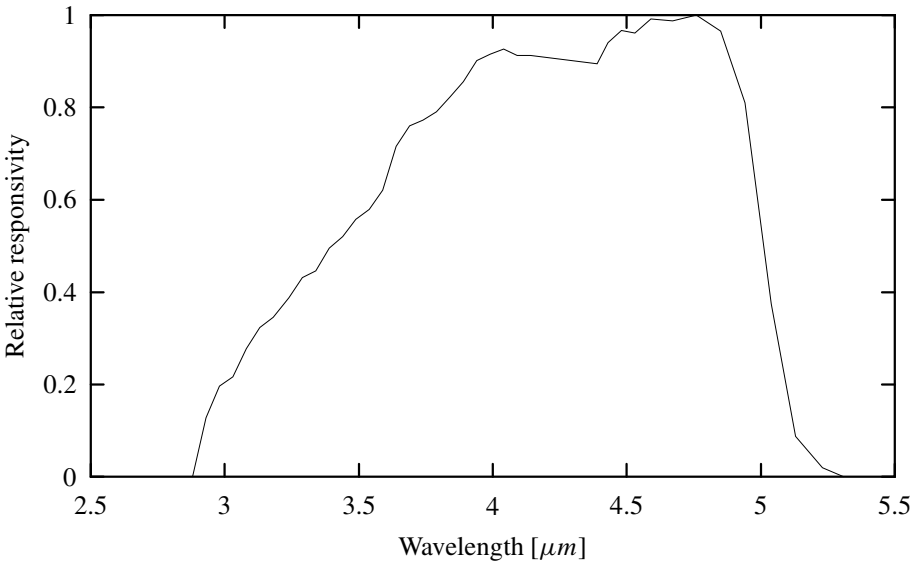

Figure 3.5 Relative responsivity for Indigo Merlin camera used by NRL.

relative spectral responses of the two cameras are presented in figure 3.6. Even though the results from the different systems can not be compared directly, it is interesting to compare the different measurements.

3.3.1 Run 8

Run 8 was a type B run performed on September 14. Passing of the waypoint was at time 16:56:12 (UTC). At that time, the ship had a speed of 9 knots and the heading was 0° (north). This run is chosen as the team from NRL was still at the shore site, and an image from the Indigo Merlin IR camera is available for analysis. NRL moved the IR cameras from the shore site to a helicopter, and performed helicopter based measurements later in the trial.

In table 3.5 the meteorology for the time at the waypoint is shown. In figures C.9 – C.13 in appendix C, detailed plots for the different meteorological data are presented. The meteorological data presented in the table are based on meteorological data from the shore site. This is valid for all data except air temperature and humidity, those are based on an average between the shore site and on board ship data. The reason for choosing these meteorological data is explained in section C.3 in appendix C. These meteorological data are used in all theoretical calculations, including the simulations in chapter 4.

Transmittance for an 1105 m path for run 8 is presented in figure 3.7. The transmittance is calculated using MODTRAN4, with the meteorological data from table 3.5.

To verify whether the ship had reached thermal equilibrium, the temperature from the on board temperature sensors can be studied. Figure 3.8 shows the temperature of selected thermocouples on board the ship. The location of the thermocouples is identified in chapter 4. Figure 3.8 indicates that the thermocouples placed on the bridge and the hull is in

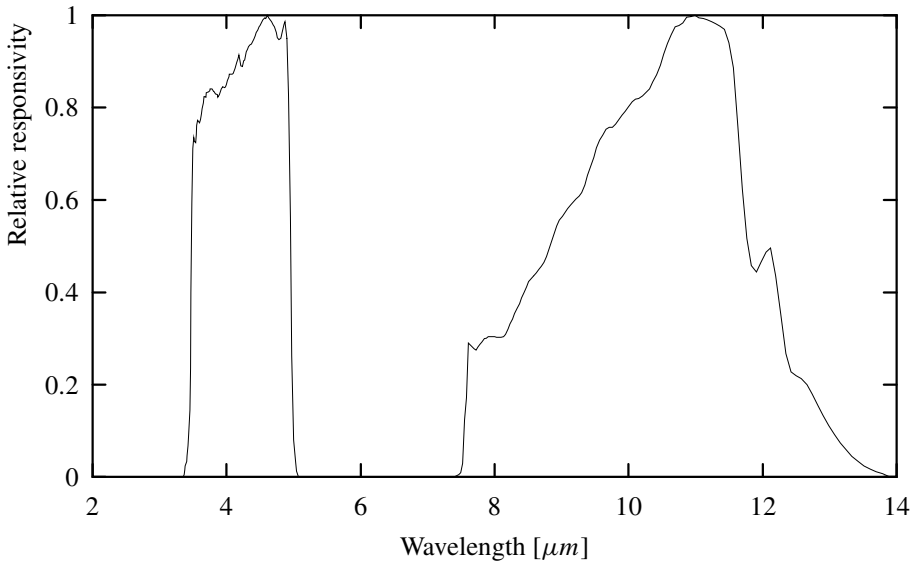

Figure 3.6 Relative responsivity for the two systems (MW and LW) used by Mariteleradar, Italy.

Parameter	Data
Air temperature	$19.6°C$
Relative humidity	48.8%
Wind speed	$4.9\,m/s$
Wind direction	337°
Wind speed (24 hrs average)	$3.8\,m/s$
Pressure	$1010.3\,mBar$
Sea temperature	$15.2°C$
Solar irradiance	$733.5\,W/m^2$
Aerosol model	NAM
AMP	9

Table 3.5 Meteorological data for run 8, 14.09.2001, 16:56 (UTC).

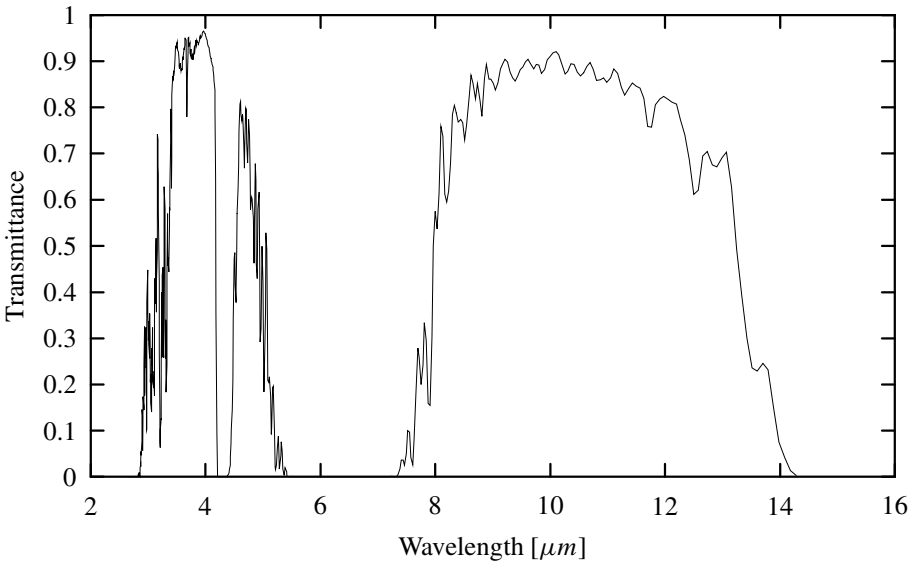

Figure 3.7 Transmittance for 1105 m path, run 8.

reasonable equilibrium at the time of the measurement. The air temperature in the figure is recorded on board the ship.

Table 3.6 shows the calculated radiant intensity contrast based on images from run 8. The distance to the ship is slightly different for the different images, and one should keep in mind that the spectral response of the different cameras is different. For the Indigo (MW) image, the calculation is performed both by FFI and NRL. During the trial and in the post analysis we have compared the methods for calculation of radiant contrast intensity. The results in table 3.6 show that FFI and NRL get the same answer from the same image. The method has to some extent also been verified by comparing calculations performed by FFI and DRDCV on the MilCam (MW) images. In section 3.4, an error analysis is performed which gives an estimate for the error in the measured radiant intensity contrast.

System (IR camera)	Distance (m)	Contrast (W/sr)
MilCam (MW)	1105	125.0
Indigo (MW) FFI calculation	1005	110.9
Indigo (MW) NRL calculation	1005	111.0
Italy (MW)	1010	115.0
Sentinel (LW)	1105	2168.1
Italy (LW)	1010	1374.0

Table 3.6 Radiant intensity contrast calculations performed on images from run 8, 14.09.2001, 16:56 (UTC).

The IR images used in the calculation for run 8 are shown in figure 3.9 – 3.11, for the MilCam (MW), Sentinel (LW), and Indigo (MW) cameras. The average of the pixels inside the red box gives the mean value of the signal from the target, $\overline{S}$ in equation (2.21). The average of the pixels inside the green box gives the mean value of the signal from the

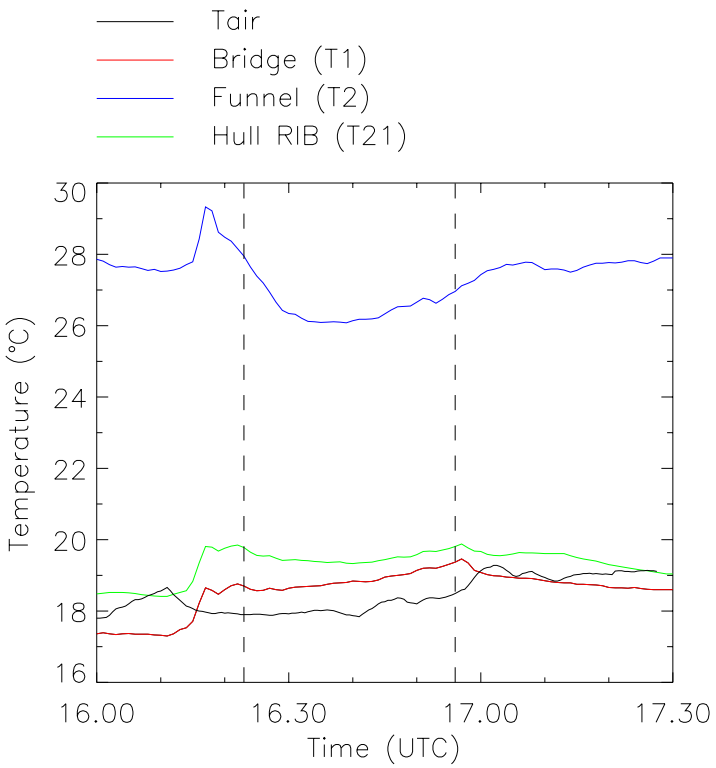

Figure 3.8 Temperature for several thermocouples on board the ship, and air temperature for run 8.

background, $\overline{B}$ in equation (2.21). The levels in all IR images are adjusted for the printed report, the images are thus not directly comparable.

The IR images from the MilCam (MW) camera are not suitable for calculation of equivalent blackbody temperature (see error analysis in section 3.4). Figures 3.12 and 3.13 show the results from a calculation of equivalent blackbody temperature from the Indigo Merlin IR image recorded by NRL during run 8.

Figure 3.13 indicates equivalent blackbody temperatures up to approximately $55°C$. In figure 3.12 all temperatures above $26°C$ are set to $26°C$ (white color). In figure 3.12 this is done to illustrate the temperature differences in the hull and the superstructure.

In figure 3.14 and 3.15, measurements performed by Mariteleradar (Italy) for run 8 are included. The temperatures in the figures are the measured values. The emissivity is assumed to be equal to 1. In both figures all temperatures above $26°C$ are set to $26°C$ (white color). Since the relative response of the different systems are not identical, it is not possible to directly compare the results. The relative response for the Italian system is presented in figure 3.6. The total apparent radiant intensity contrast calculated by Mariteleradar for run 8 is presented in table 3.6. It is not clear why the measured temperature in the sea background and the sky just above the horizon is son different in the two images (figure 3.14 and 3.15).

By using the method in section 2.4, the radiant intensity contrast for a virtual sensor with relative spectral response equal to 1 from 3.0 μm to 5.0 μm can be calculated. The calculation is performed for both the MilCam camera and the Indigo Merlin camera. The

Figure 3.9 IR image (MilCam MW) of CFAV Quest, distance 1105 m, run 8, 16:54:43 (UTC).

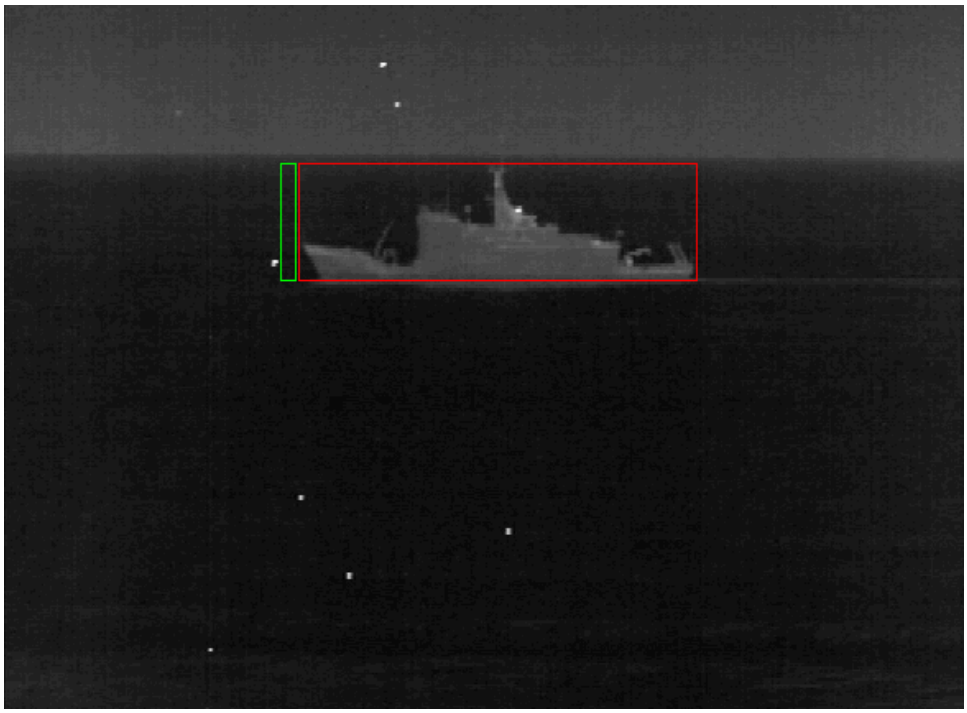

Figure 3.10 IR image (Sentinel LW) of CFAV Quest, distance 1105 m, run 8, 16:54:43 (UTC).

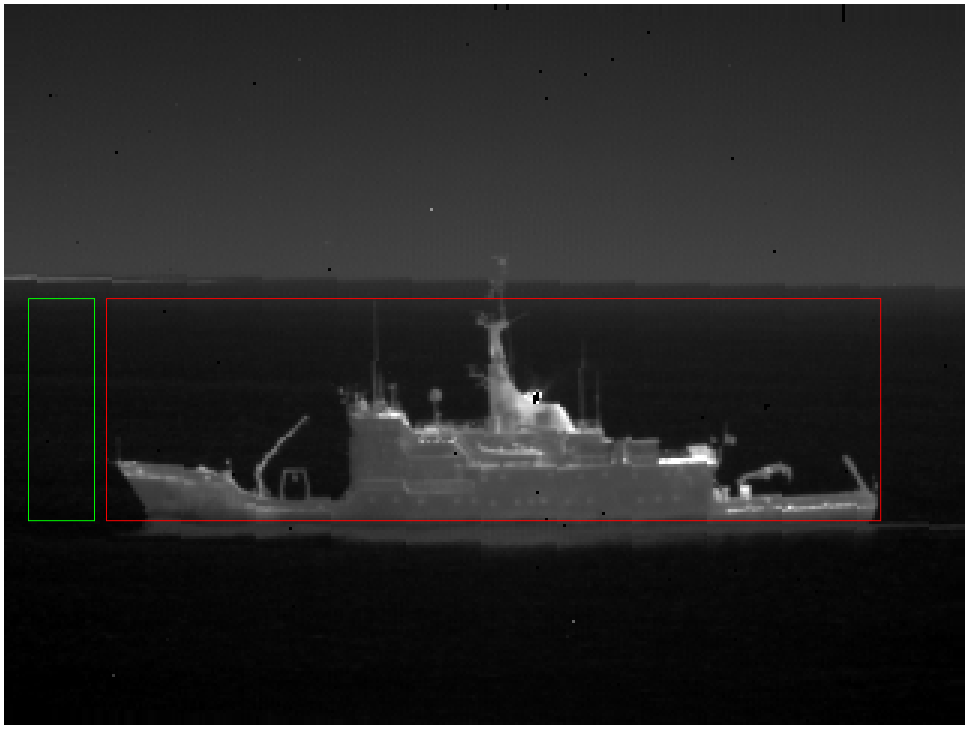

Figure 3.11 IR image (Indigo Merlin MW) of CFAV Quest, distance 1005 m, run 8.

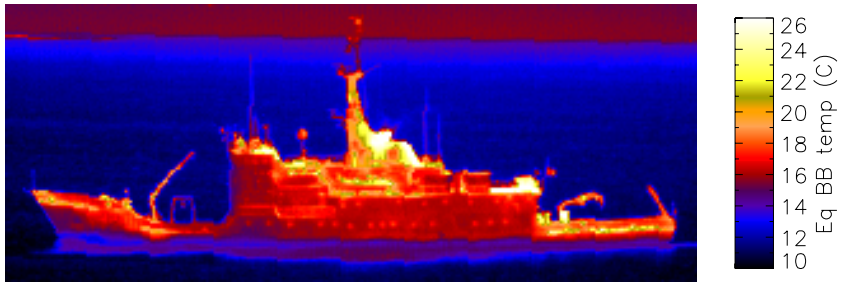

Figure 3.12 Equivalent blackbody temperature for CFAV Quest. Based on Indigo Merlin IR image, distance 1005 m, run 8. Temperatures higher than 26°C are not shown.

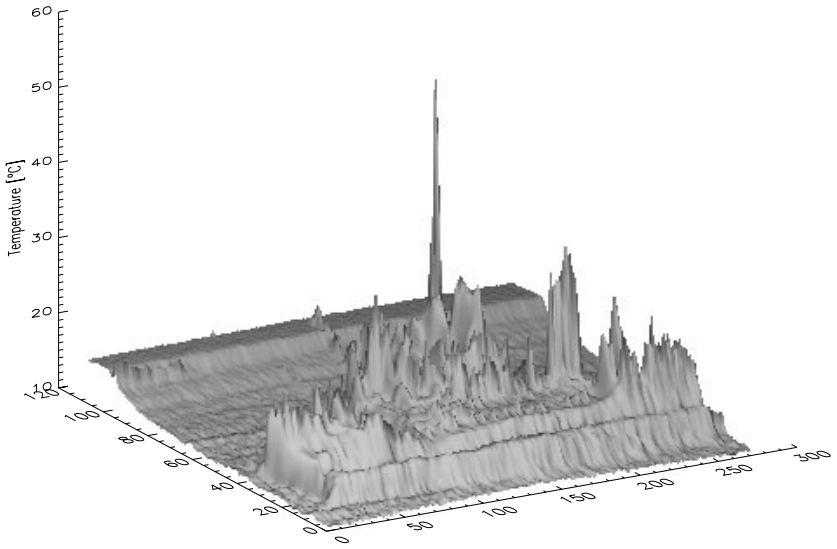

Figure 3.13 *Equivalent blackbody temperature for CFAV Quest. Based on Indigo Merlin IR image, distance 1005 m, run 8.*

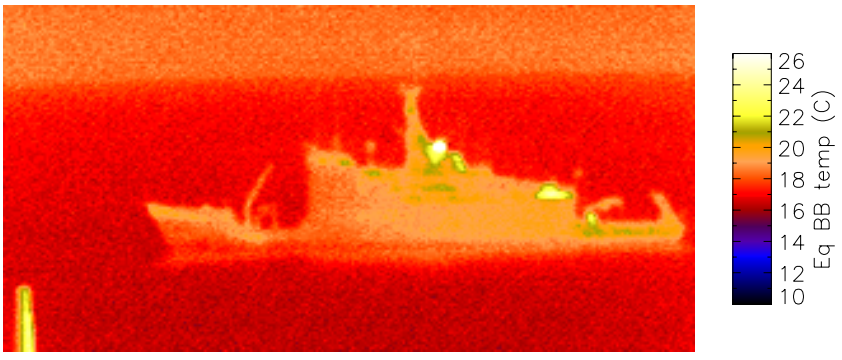

Figure 3.14 *Measured blackbody temperature for CFAV Quest. Measured by Maritelera-dar (Italy) with an Agema 900 MW system, distance 1010 m, run 8. Tempe-ratures higher than* $26°C$ *are not shown.*

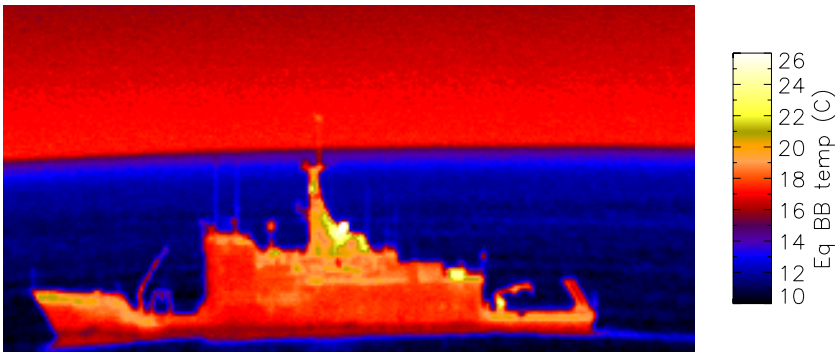

Figure 3.15 Measured blackbody temperature for CFAV Quest. Measured by Maritelera-dar (Italy) with an Agema 900 LW system, distance 1010 m, run 8. Temperatures higher than $26°C$ *are not shown.*

virtual radiant intensity contrast based on an image from the MilCam camera is 139.2 W/sr, and based on the Indigo Merlin camera 142.0 W/sr.

3.3.2 Run 34

Run 34 was a type D run, performed on September 19. The ship passed the waypoint twice, at 23:31:24 (UTC) measuring the port side of the ship, and 23:39:15 measuring the starboard side. The analysis in this section is performed for the first passing, the port side of the ship.

Parameter	Data
Air temperature	$13.6°C$
Relative humidity	55.3%
Wind speed	$3.1\,m/s$
Wind direction	$1°$
Wind speed (24 hrs average)	$4.5\,m/s$
Pressure	$1023.4\,mBar$
Sea temperature	$16.7°C$
Solar irradiance	$0\,W/m^2$
Aerosol model	NAM
AMP	8

Table 3.7 Meteorological data for run 34, 19.09.2001, 23:31 (UTC).

The meteorological data valid for run 34, and used in the simulations, are shown in table 3.7. In this case all of the meteorological data are from the shore site (no averaging with ship data). Detailed plots for the different meteorological data are presented in figure C.14 – C.18 in appendix C. The MilCam (MW) image used for the analysis is recorded at 23:29:45 (UTC), when distance to the ship was 1103 m. The Sentinel (LW) image used is recorded at 23:31:25 (UTC), at a distance of 1000 m.

Figure 3.16 shows temperature measurements of parts of the ship during run 34. The figure indicates a decreasing temperature during the run. The air temperature also has a decreasing tendency, see also figure C.14. The temperature measured on the funnel, shows that this part of the ship is clearly not in thermal equilibrium for the starboard measurement.

System (IR camera)	Distance (m)	Contrast (W/sr)
MilCam (MW)	1103	47.1
Italy (MW)	1010	32.5
Sentinel (LW)	1000	2658.7
Italy (LW)	1010	1450.0

Table 3.8 Radiant intensity contrast calculations performed on images from run 34, 19.09.2001, 23:31 (UTC).

The results for run 34 are summarized in table 3.8. The Italian results are included for comparison, but can not be compared directly with the FFI results due to differences in

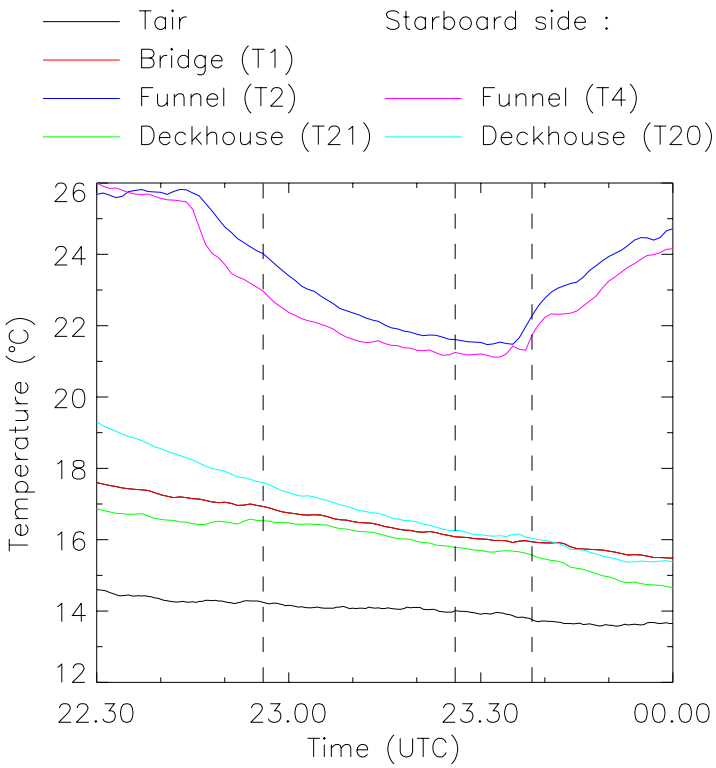

Figure 3.16 *Temperature from several thermocouples on board the ship, and air temperature for run 34.*

spectral response. The MilCam (MW) image used for calculation is shown in figure 3.17, and the Sentinel (LW) image used is shown in figure 3.18.

In figure 3.19 an image from the MilCam (MW) camera of the starboard side of the ship is shown. The distance to the ship is 1056 meter, and the measured apparent radiant intensity contrast for this image is 51.5 W/sr. Figure 3.17 and 3.19 are visually comparable.

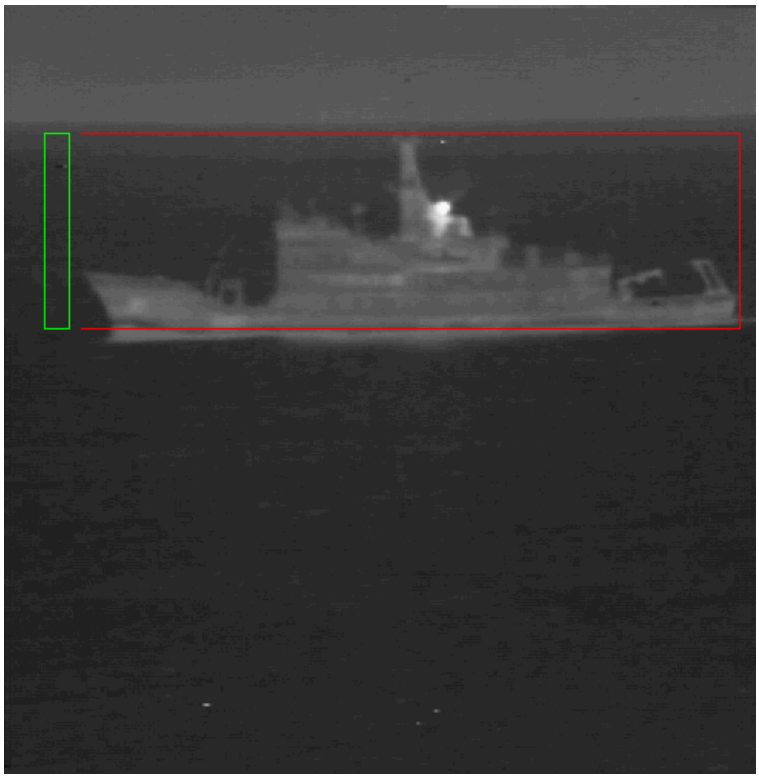

Figure 3.17 IR image (MW) of CFAV Quest, distance 1100 m, run 34, 23:29:45 (UTC).

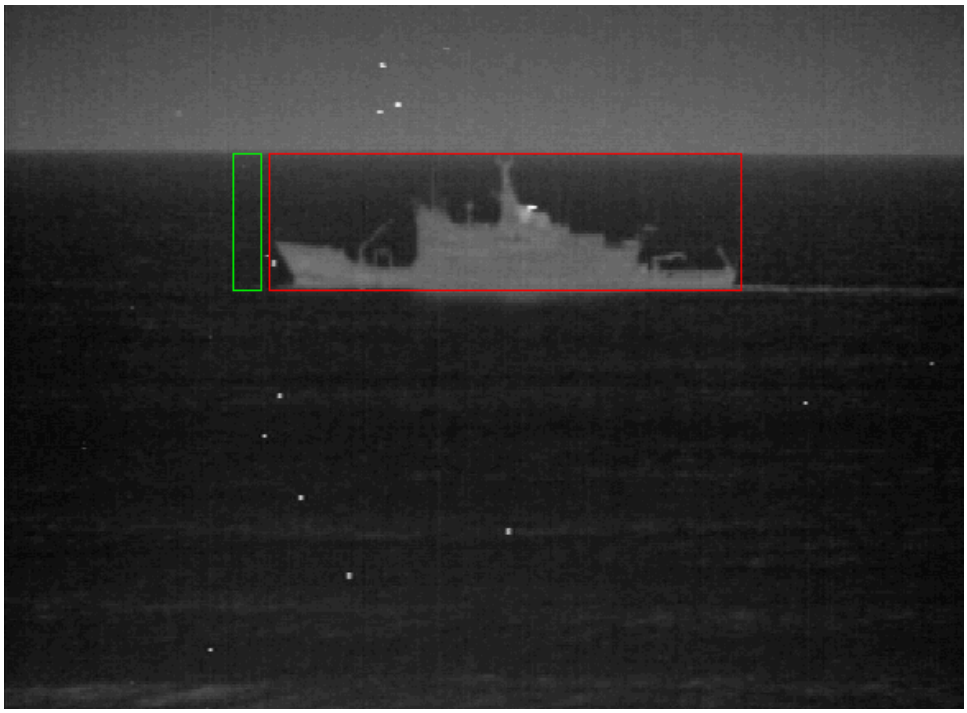

Figure 3.18 IR image (LW) of CFAV Quest, distance 1000 m, run 34, 23:31:25 (UTC).

Figure 3.19 IR image (MW) of CFAV Quest, distance 1056 m, run 34, 23:37:52 (UTC). A and B indicates hot areas that don't have counterparts on the port side.

3.3.3 Day and night variations

During the trial several measurements were performed for the different run types. Tables 3.9 – 3.12 give a summary of the results for the different run types. The results presented in this section are all based on images from the MilCam (MW) camera. Due to the instability of the Sentinel (LW) camera it is chosen not to analyze all runs from that camera. There is quite a large difference in measured apparent radiant intensity contrast between the day runs (A, B, and C) and the night runs (D). Figure 3.20 and 3.21 gives an illustration of a night and day time run recorded with the MilCam (MW) camera.

Figure 3.20 Night time illustration, run 15 (type D run), distance 1185 m. MilCam (MW) IR camera.

Figure 3.21 Day time illustration, run 24 (type C run), distance 1065 m. MilCam (MW) IR camera.

In table 3.9 the results from the type A runs are summarized. For run 13 there are no valid data due to blackbody saturation in the calibration image. Three runs are not a large data set to verify the data. Run 31 is the best of these runs for ShipIR validation, since run 18 has a poorly performed calibration and there are some clouds during run 9.

The results from the type B runs in table 3.10 show to some degree a variation in the contrast. Due to the fact that an image from the NRL Indigo Merlin (MW) camera was available for run 8, this run was chosen for detailed analysis.

The results for the type C runs in table 3.11 indicate a much lower contrast in run 24 than the other runs. This is probably due to differences in the weather. Run 24 had a very

Run	Distance (m)	Contrast (W/sr)
9	1075	92.8
13	1120	-[2]
18	1175	78.7[3]
31	1100	71.3

Table 3.9 Apparent radiant intensity contrast for A type runs. Measurements performed with MilCam (MW) IR camera.

Run	Distance (m)	Contrast (W/sr)
8	1105	125.0
17	1125	91.9[3]
22	1085	83.1
29	1100	71.3
36	1180	107.4

Table 3.10 Apparent radiant intensity contrast for B type runs. Measurements performed with MilCam (MW) IR camera.

extensive cloud cover with scattered areas of clear sky (see table C.4). This means that the sea background will have a higher equivalent blackbody temperature and thus a higher radiant intensity for this run than the runs with a totally clear sky. This is due to the fact that the sea very much reflects the sky. This is illustrated in figure 3.22. In this figure, the equivalent blackbody temperature is calculated from the images. Due to the partly clouded sky run 24 is not recommended for ShipIR validation.

Run	Distance (m)	Contrast (W/sr)
10	1152	143.8
14	1177	148.1
19	1119	145.6
24	1065	77.0
32	1063	120.5

Table 3.11 Apparent radiant intensity contrast for C type runs. Measurements performed with MilCam (MW) IR camera.

The type C runs are very sensitive regarding sun reflection. At 21:00 (UTC) the position of the sun is about 14° in elevation and 260° in azimuth, see figure 3.3. With a typical heading of the ship of 32°, the sun reflection in the ship hull and superstructure changes rapidly.

The apparent radiant intensity contrast for the night runs, presented in table 3.12, varies to some extent (between 20 W/sr and 58 W/sr). The starboard measurements give higher

[2]Saturation in blackbody calibration image

[3]Poorly performed non-uniformity correction

Run	Aspect	Distance (m)	Contrast (W/sr)
11	Port	1166	26.7
12	Port	1161	20.1
15	Port	1190	28.8
16	Port	1115	39.8
20	Port	1081	39.5
21	Port	1118	42.6
26	Port	1083	39.0
27	Port	1120	34.3
34	Port	1103	47.1
39	Port	1105	30.1
40	Port	1160	26.0
11	Starboard	1066	40.7
12	Starboard	1066	20.2
15	Starboard	1085	40.0
16	Starboard	1078	41.0
20	Starboard	1069	46.4
21	Starboard	1137	43.3
26	Starboard	1154	55.7
27	Starboard	1105	58.0
34	Starboard	1056	51.5
35	Starboard	1060	43.5
39	Starboard	1100	52.2
40	Starboard	1105	51.8

Table 3.12 Apparent radiant intensity contrast for D type runs. Measurements performed with MilCam (MW) IR camera.

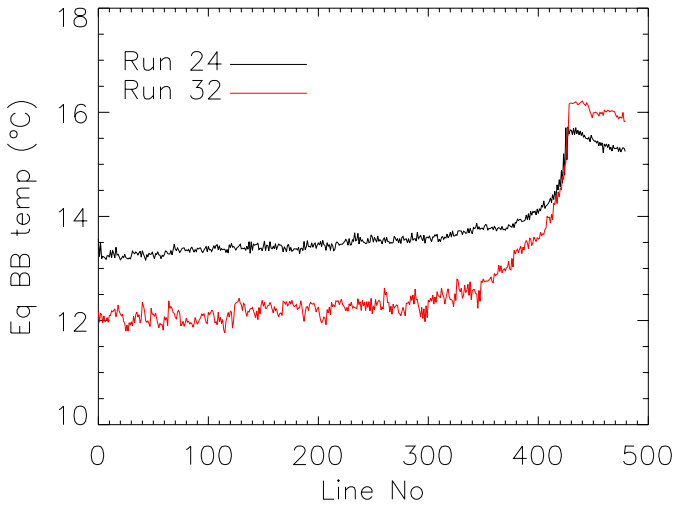

Figure 3.22 Calculated equivalent blackbody temperature for background in runs 24 and 32, based on MilCam (MW) images.

values than the port measurements.

Figure 3.23 presents the apparent radiant intensity contrast for all the night runs (type D) based on the MilCam (MW) images. For the type D runs, both the port and starboard side of the ship were measured. The distance between the shore station and the ship varies slightly, see table 3.12. In figure 3.23, the uncertainty of the measurement is marked with dashed lines. The relative uncertainty is based on the calculation for run 8 presented in section 3.4.

Since these are night time recordings, there should not be any variation due to the sun. Then there is basically only two things left to give the variation of the starboard and port side of the ship. These are the variation of wind speed and direction, and differences of the port and starboard sides of the ship (including the viewing angle from the shore site). There are some constructional differences between the port and the starboard side of the ship. On the starboard side there is a “walkway” next to the superstructure, while on the port side this “walkway” is partly inside the superstructure. There is also an outlet for ventilation air from machine room on the starboard side, marked with “A” in figure 3.19. According to the instrumentation plan (5) there should be an intake for the air cooled condenser room, marked with “B” in figure 3.19, and an outlet on the port side. From the images it seems like this is the other way around. This means that there are two areas with hot air coming out at the starboard side of the ship.

From the meteorological data in tables C.7 and C.8, it is clear that the wind speed does not vary a lot, but the wind direction varies to some degree. Figure 3.24 shows an illustration of the wind direction during some of the type D runs. The ship course is indicated with the blue line.

For all night-time (type D) runs, except 11, 12, 39, and 40, there is an almost totally clear sky. In a night-time situation (or no sun heating) with a clear sky and no wind, the ship will lose heat due to radiation cooling. Increasing wind speed reduces the radiation cooling due

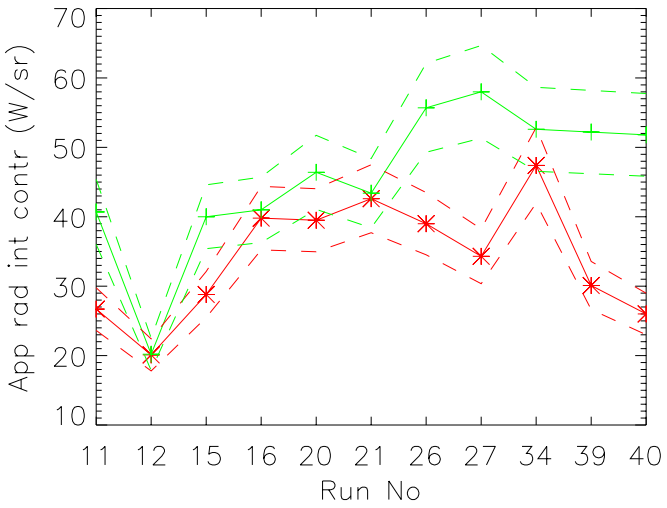

Figure 3.23 *Apparent radiant intensity contrast for all D (night) runs. Measurements of both port (red line) and starboard (green line) sides of the ship performed with the MilCam (MW) IR camera. The uncertainty of the measurement is indicated with dotted lines.*

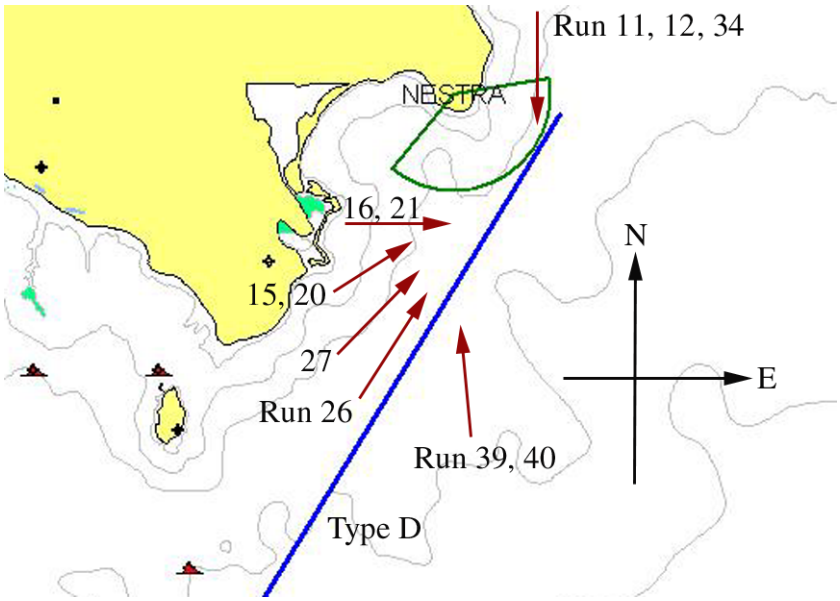

Figure 3.24 *Indication of wind direction for some of the night time runs.*

to convective heat transfer from the air. The increased ship radiation in a windy situation compared to the no wind situation is dependent on the wind speed and the meteorological situation (i.e the transmittance to space).

This effect is due to convective transfer of heat from one place to another by the motion of a fluid. In this case the fluid is air. In (9) the following approximation for convective loss is given:

$$Q = h\,A\,(T_s - T_{ambient}) \tag{3.1}$$

where

Q	-	Quantity of heat supplied
T_s	-	Surface temperature
$T_{ambient}$	-	Fluid temperature, $T_{ambient} = T_{air}$
h	-	Convective heat-transfer coefficient
A	-	Cross-sectional area

In a no wind situation, the convective heat-transfer coefficient is small and the surface temperature is lower than the ambient temperature due to radiation cooling. In a windy situation, the convective heat-transfer coefficient is larger. The heat flux from atmosphere to surface will then be larger than the heat flux from the surface due to radiation. The net result is that the surface temperature is almost the same as the air temperature in a windy situation. In a clear sky situation, the radiant intensity of the ship may thus increase due to wind compared to a no wind situation.

For runs 15, 20, 26, and 27, the wind speed is very close to the ship speed, which gives almost no relative wind at the ship when the ship heading is close to the wind direction.

Following the arguments above, the contrast should be higher for the starboard side than for the port side for runs 15, 20, 26, 27, 39, and 40. In figure 3.23 this is really the case for all these runs. With wind almost directly towards the side of the ship, which is the case in runs 16 and 21, the difference between the starboard and port sides should be small. This is also the case in the measurements. Run 11, 12, 39, and 40, could be difficult to use because of clouds.

The differences between port and starboard side measurements can be due to the described wind effect or the differences that has been observed in the ship configuration.

3.4 Error analysis

When measurements are to be used for model validation, it is very important that the uncertainty of the measurements are known.

The calculation of apparent radiant intensity contrast from the measurements are based on equation (2.21):

$$J_c = \frac{\Omega_s\, {x_t}^2\, M_{tgt}\, \left(\overline{S} - \overline{B}\right)}{K} = \frac{\Omega_s\, {x_t}^2\, M_{tgt}\, \Delta}{K} \tag{3.2}$$

In (4) it is shown that the error term is given by:

$${U_{J_c}}^2 = {U_{\Omega_s}}^2 + 4\,{U_{x_t}}^2 + {U_K}^2 + {U_{M_{tgt}}}^2 + {U_\Delta}^2 \tag{3.3}$$

Where U is relative standard deviation (i.e σ_x/x).

The individual terms must then be estimated. A list of the different terms, and how they can be estimated is given below:

U_{Ω_s}: Due to optical distortion and error in the spatial calibration.

U_{x_t}: Due to errors in range measurement and variation of range over target.

U_K: This term is due to error in the calibration. This includes several aspects like; thermal stability, uniformity over filed of view, uncertainty in temperature of blackbody, uncertainty in emissivity of blackbody, errors in spectral response. Is is *possible* to estimate the term. (See section below.)

$U_{M_{tgt}}$: Error due to selected box size. If all target pixels are inside the target box, the term can be estimated by (4):

$$U_{M_{tgt}} \approx \frac{0.2}{\sqrt{M_{tgt}}} \tag{3.4}$$

U_Δ: The accuracy of the difference of the means (signal and background). Can be estimated by standard statistical sampling theory:

$$U_\Delta = \frac{\sqrt{\frac{{\sigma_S}^2}{M_{tgt}} + \frac{{\sigma_B}^2}{M_{bck}}}}{\overline{S} - \overline{B}} \tag{3.5}$$

The terms U_{Ω_s} and U_K should be computed for each calibration. While the terms U_{x_t}, $U_{M_{tgt}}$, and U_Δ should be computed for each analyzed image.

An example calculation based on run 8 for the Inframetrics MilCam camera has been performed, and the following values for the different terms have been found: $U_{\Omega_s} = 0.02$, $U_{x_t} \approx (10+10)/1100 = 0.018$, $U_K \approx 0.11$, $U_{M_{tgt}} \approx 0.0007$, $U_\Delta \approx 0.017$. For this run the total uncertainty is given by $U_{J_c} \approx 0.115$. For run 8 this shows that the apparent radiant intensity contrast is:

$$J_c = 125.0 \pm 14.3 \ W/sr \tag{3.6}$$

The error analysis shown is an example for the apparent radiant intensity contrast for run 8. There is however no reason to believe that there is a big difference between this run and the other runs. The reason is that the main contributor to the total error is U_K, which is due to calibration of the camera. There could be a slight variation in this value, since a new calibration is done for each run. However, this variation is expected to be small.

As shown in section 3.2, there is a drift in the camera. This only affects the U_K value to a very small degree. This is due to the fact that contrast calculations are always based on radiation differences in a given image.

NRL has performed the same error analysis based on run 8, and the reported result from NRL (for the Indigo Merlin MW image) is:

$$J_c = 111 \pm 10 \ W/sr \tag{3.7}$$

For calculation of equivalent blackbody temperature using equation (2.10), the error term is somewhat different. In this case there is a term from the offset value in addition, U_{S_0}. The drift in the camera that is identified will cause quite a large U_{S_0} term. This means that calculations of equivalent blackbody temperature will have a larger error term than the apparent radiant intensity contrast. As shown in section 3.2, the drift in the camera is quite large, which will cause a considerable uncertainty to the calculated equivalent blackbody temperature from the MilCam (MW) images. Based on this no calculations of equivalent blackbody temperature from the MilCam (MW) images are performed.

3.4.1 Calibration error

One of the terms in the error analysis is the error term from the calibration, U_K. This term consists of several contributions. Some of the contributions are identified by NRL (10), and some are identified in (11) and some by FFI. Below is a list of these terms, and the estimated error for each term based on the Inframetrics MilCam camera and data from run 8.

Signal-to-noise in the calibration: To quantify the signal-to-noise term, equation (3.5) is used. For this case this term is 0.54%.

Spectral response: The estimation of uncertainty due to the spectral response can be done by taking the original spectral response curve and adding random noise. NRL has used 5% in response and 1% in wavelength. Using this new spectral response, the camera factor in equation (2.7) is recalculated and the error is found from the change in K. For this case the error is 8.2%.

Blackbody temperature error: The effect of the error in the temperature measurement for the blackbodies can be found from equation (2.7). The error in temperature measurement for the Mikron blackbodies used is $x^\circ C$, and this gives an error which is 3.3%.

Blackbody emissivity error: The emissivity of the blackbodies are usually measured, and the error is based on an analysis of the uncertainty of these measurements. Figure 3.25 shows the emissivity of the different blackbodies we have at FFI. The blackbodies used in the SIMVEX trial for camera calibration were the Mikron blackbodies. The emissivity of these blackbodies has not been measured in the 3–5 μm region, we therefore have to rely on the specification, $\epsilon = 0.97 \pm 0.02$. (The absolute emissivity has not been measured, but comparative measurements with other blackbodies show that this is correct.)

Stability: This is how the responsivity drifts with time. The value is based on subsequent calibrations, to see how K changes. At the SIMVEX trial we did a new set of calibrations both before and after each measurement. The typical time between these two calibrations was 8 minutes. The error caused by the drift during this time is 3.3%.

Uniformity: This is quantified by repeating calibrations with the blackbody in different parts of the field of view. A simple approach is to divide the field of view into 9 rectangles and perform 9 calibrations. This term is dependent on the uniformity of the detector, the camera non-uniformity correction, and the optics. This term was not measured during the SIMVEX trial for the MilCam camera, and it is guessed to be 5%.

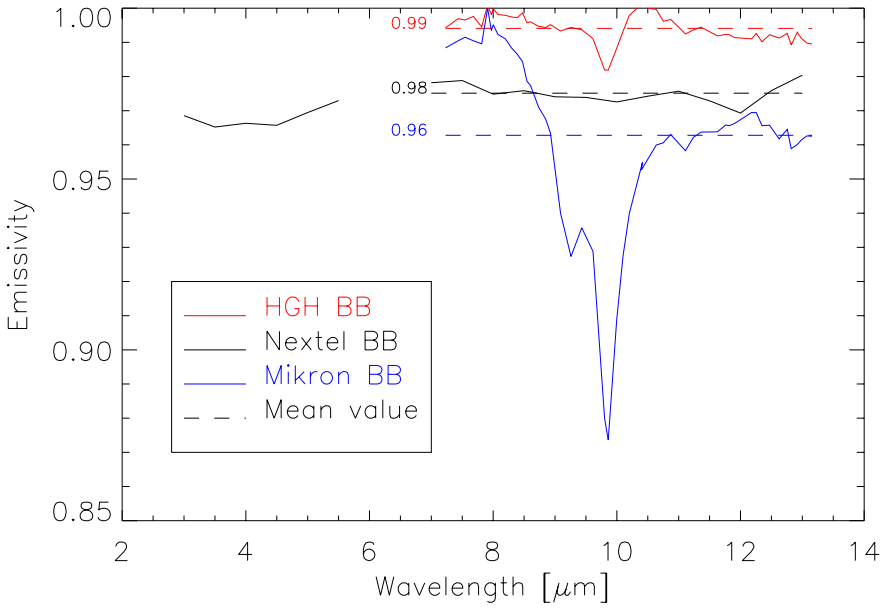

Figure 3.25 Emissivity for the different FFI blackbodies.

The total uncertainty of the calibration is approximated as:

$$U_K{}^2 \approx \sum_i U_{K_i}{}^2 \tag{3.8}$$

where

U_{K_i} - uncertainty of the different parts in the calibration

3.4.2 Sentinel (LW) error analysis

Since the spectral response of the Sentinel (LW) camera is unknown, the uncertainty from the spectral response will be the biggest contributor to the calibration uncertainty, U_K. This part will also dominate the total uncertainty.

As shown in section 3.2, the drift in the Sentinel camera is much larger during day-time measurements than during night-time measurements.

3.5 Discussion

The measurement setup for this trial was very successful, and the trial was carried out in a very satisfying way. The FFI measurements with the infrared cameras, are not of the wanted quality. The uncertainty for the MilCam MW camera is estimated to 11.5% for run 8, and there is no reason to believe that this uncertainty is lower for other runs. For run 13 there is saturation in the MW calibration image, and for run 17 and 18 a poorly non-uniformity correction is performed. These 3 runs will thus not be used for ShipIR validation.

The Amber Sentinel LW camera has worse performance. The uncertainty for the LW camera is much bigger than the MW camera, this is due to a large drift in the camera. At present time the exact relative spectral response is not known, and this adds to the error. The measured LW data is not suitable for ShipIR validation. There will still be showed some ShipIR LW results in section 4.1.2. Keep in mind the quality of the LW camera when comparing LW simulations and LW measurements.

The main focus of the comparison between simulation and measurement will be based on the results from the MilCam MW camera.

4 SIMULATIONS

This chapter consists of simulation results obtained by the ShipIR/NTCS (Naval Threat/Countermeasure Simulator) modeling package, and comparisons with the measurements presented in the previous chapter. ShipIR/NTCS was originally developed by W. R. Davis Engineering Ltd. with funding from the Canadian Department of National Defence, through the Defence Research and Development Canada Valcartier (DRDCV). ShipIR/NTCS was chosen as a NATO standard by RSG-5, and version 2.3 was released in 1997 as a NATO version and distributed to RSG-5 countries. Several improved versions have since been released, with funding mainly from DRDCV and NRL.

ShipIR/NTCS provides the steady state infrared signature of a target (as plate temperatures or patch radiance values[1]) in an infrared maritime background given by the input weather data. The target must be specified through a 3D CAD model with further optional specifications of plume gas pressures and temperatures, internal heat sources and ventilation, and spectral emissivity of ship surface materials.

The latest version of ShipIR/NTCS, version 2.9b running on an SGI Octane computer, was used to simulate the temperature of selected portions of the CFAV Quest and the total infrared apparent radiant intensity contrast of the ship for selected SIMVEX trial runs. The SIMVEX trial was set up to facilitate model validation. The ship was supposed to hold a steady course for 30 minutes prior to the measurement to ensure thermal equilibrium. Only runs that had reasonably stable weather conditions during this period were chosen for further analysis[2]. Thermocouple and I-button temperature data from various locations on the ship facilitated validations of the plate temperatures computed by ShipIR/NTCS, while the measured apparent radiant intensity contrast could be compared with the contrast derived from the scene radiance computed by the model.

A very comprehensive CAD model of CFAV Quest, see figure 4.1, and a complete ShipIR/NTCS input target file was developed for the trial by NRL and W. R. Davis Engineering Ltd. respectively. (For simplicity, ShipIR/NTCS will be referred to as ShipIR in the rest of the chapter). In addition, W. R. Davis Engineering Ltd.[3] also performed a detailed analysis of the ship's ventilation system. Measurements of the reflectivity of selected paint from CFAV Quest (performed by FFI and NRL) and analysis of plume gases were also performed and were input into the model. The Norwegian paint measurements are described in appendix D. Figure 4.2 shows the specular reflectivity in the infrared wavelength range of the two main paints on the CFAV Quest. For a description of how to get this result from the measurement, see (12). The figure is based on the Quest_white.mtl and Quest_yellow.mtl files supplied with the SIMVEX data set distributed by DRDCV. There seems to be an inconsistency in the long wavelength end of the white paint data set, this is tentatively corrected in this work (by FFI) and shows up as the dotted line in the figure. The effect of this change seems to be minimal.

[1] Patches are the smallest entities used by ShipIR/NTCS, while plates are a collection of patches that are assumed to have the same temperature.

[2] The model only supports clear sky background or a total overcast sky background. Runs with a partial cloud cover are thus not ideally suited for model validation, and are thus not used.

[3] With funding from DRDCV.

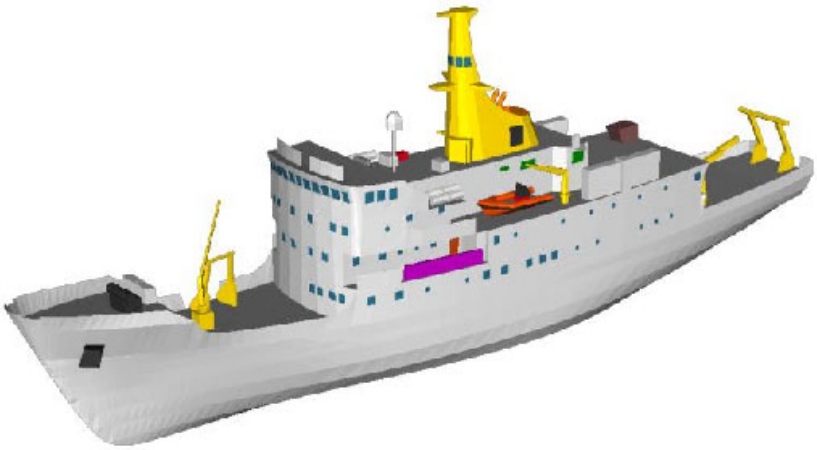

Figure 4.1 *The CAD model of CFAV Quest used in the ShipIR simulations. Different colors indicate surface materials with different IR properties. The colors are adjusted to fit the visible appearance of the ship, see figure 1.1.*

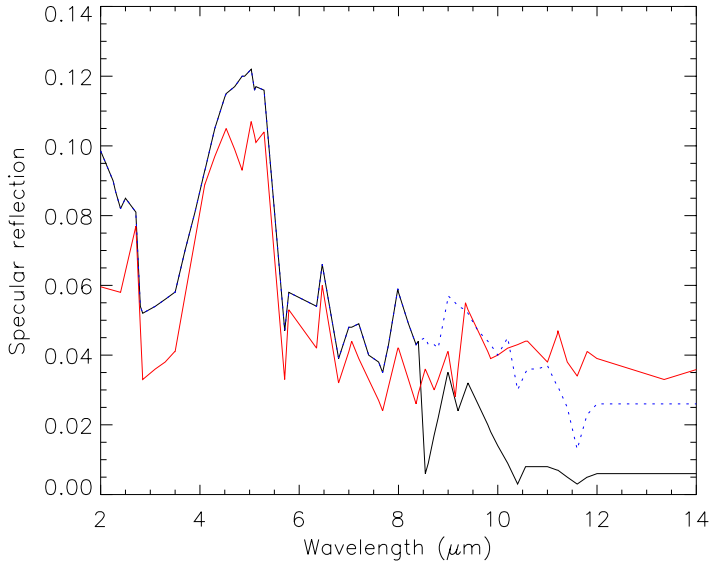

Figure 4.2 *The modeled specular reflectivity of the white (black curve) and the yellow (red curve) paint of the Quest is shown. The data are based on spectral paint measurements. The dashed blue curve is a correction to the white paint curve introduced to make it fit the measured data in the long wavelength region.*

4.1 ShipIR calculations

Simulations were performed both in the MW and in the LW infrared bands. The spectral responsivity for the two cameras operated by FFI during the trial, the MilCam MW and the Sentinel LW were input to ShipIR. The relative response of the Sentinel camera is unknown and set to 1.0 in the 8–12 μm range and 0.0 outside this range. This means that the received radiance values computed by ShipIR for the LW-case will be upper limits. The measured relative response of the MilCam camera is shown in figure 2.3. In addition, one image from the Indigo Merlin MW camera operated by NRL that was analyzed in chapter 3 was simulated in ShipIR, using the corresponding relative response (figure 3.5).

Complete meteorological data, the observer height and distance, field of view of the cameras, ship speed, heading and bearing were input into ShipIR for the calculations. We used the Norwegian data sets for these inputs except where noted. The standard MODTRAN mid latitude summer atmospheric profile scaled with the measured meteorological data was used throughout the simulations. The Navy Aerosol Model (NAM) was used for the aerosols, Cox and Munk roughness parameters were used for the sea model and sea glint was set to normal. The sky is assumed to be clear for all runs. Despite a lot of good weather, this is not always the case, see table C.4. Simulation results from runs with clouds will therefore have higher uncertainty. The full spectral option in ShipIR was used for the target processing due to the rather large variation of emissivity in the two main paint materials, see figure 4.2. The thermal boundary conditions and the plume data were taken from the SIMVEX data set distributed by DRDCV.

As pointed out in appendix C, the value of the measured meteorological parameters varies between the shore site and the ship. This may be due to a real variation of the meteorological data as the ship approaches the shore, or due to measurement uncertainty or error. Such variation may change from day to day and between night and day. For two of the night runs studied, separate calculations have been performed using the shore air temperature and relative humidity and using the corresponding parameters measured by the weather station on the ship. The other weather parameters were not seen to vary significantly (at least not from a modeling perspective) between the shore and the ship.

The wind speed enters the model in the transmission calculation, where an average wind speed along the transmission path at the time of measurement would be optimal. It is also used to account for wind convection, where a time-averaged wind speed is probably needed. The wind speed for the transmission calculation may be somewhat different from the ship convection wind speed. However, the wind speed is probably not very important for the transmission calculation. In any case, different wind speeds may be needed for the background and the target processing within ShipIR. An option to use two different wind speeds exists within the latest version of ShipIR.

In ShipIR one can use LOWTRAN, MODTRAN3 or MODTRAN4 for background and target processing. Figures 4.3 and 4.4 show the difference in the MW and LW bands between using MODTRAN4 with LOWTRAN resolution (20 cm^{-1}) and using the LOWTRAN (20 cm^{-1}) option in MODTRAN4 (the new ShipIR LOWTRAN implementation). It is seen from the figure that the results for the transmission may differ by as much as 10 % from 3.3 –4.0 μm in the MW band, while the agreement is generally

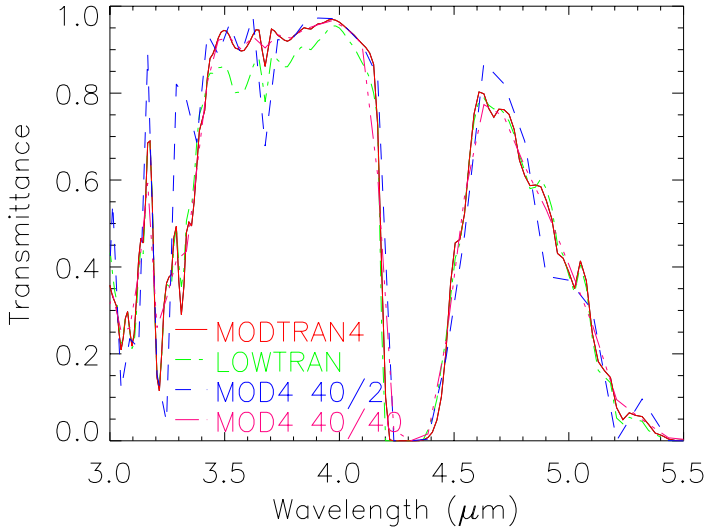

Figure 4.3 *Transmission in the MW band for an 1105 m path with meteorological data given by Table 3.5. The red curve shows the MODTRAN4 result with resolution reduced to LOWTRAN resolution (20 cm^{-1}), while the green curve shows the result of using the LOWTRAN flag in MODTRAN4. The blue and purple dashed curves show the result of a 2 cm^{-1} vs a 40 cm^{-1} slit function with 40 cm^{-1} sampling.*

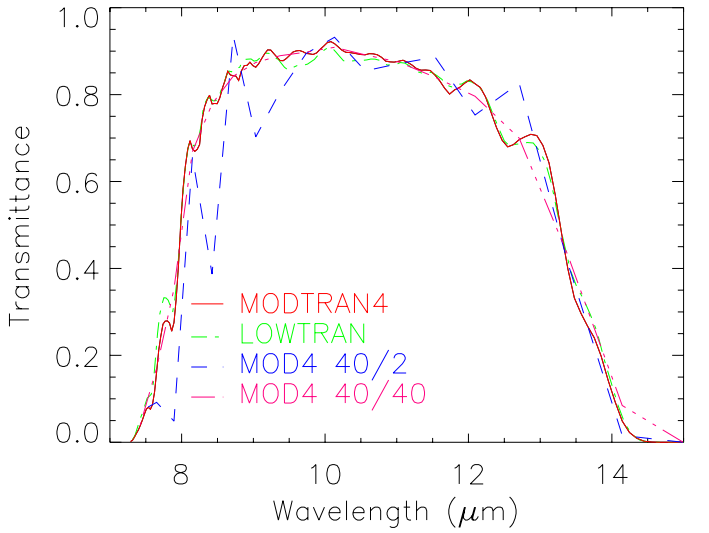

Figure 4.4 *Transmission in the LW band for an 1105 m path with meteorological data given by Table 3.5. The red curve shows the MODTRAN4 result with resolution reduced to LOWTRAN resolution (20 cm^{-1}), while the green curve shows the result of using the LOWTRAN flag in MODTRAN4. The blue and purple dashed curves show the result of a 2 cm^{-1} vs a 40 cm^{-1} slit function with 40 cm^{-1} sampling.*

better in the LW band. Using the MODTRAN option in ShipIR, one additionally gets the added accuracy of the MODTRAN4 2 cm^{-1} band model resolution. To take advantage of the better resolution, one must specify a similar or higher resolution in the observer related parameters. Referring to the previous figures, we chose to use the more time-consuming MODTRAN option for the background and target processing. As a minimum, a spectral resolution of 2 cm^{-1} is used throughout the simulations. However, note that for the total thermal calculation which ranges from 0.3 to 250 μm, one has no control over the wavenumber increment used – it is found to be 40 cm^{-1}, while 2 cm^{-1} slit functions are used, resulting in a severe undersampling of the spectra. See figures 4.3 and 4.4 for an example of the effect of this undersampling in the MW and LW bands, but keep in mind that the full range in the total thermal calculation is from 0.3 to 250 μm.

Some day runs are simulated, and almost all the night runs. For the night runs, one calculation is made for each set of weather parameters, but results are obtained for both port and starboard aspect by simply changing the ship heading in ShipIR. This way, one accounts for the measurements taken of both port and starboard aspect of the ship during the night runs. The two measurements are only separated by a few minutes, so the slight change in weather parameters during this time is thought to be negligible. The distances are nearly the same for the port and starboard images, so no new calculation of the atmospherical propagation is performed. This could of course not be done for a day run when the influence of solar radiation is large. How to treat the wind is the only remaining issue. Assuming the wind direction is fairly constant during the runs, the ship will be exposed to wind from one angle for 30 minutes, but after the ship turns, only a few minutes pass until the measurement. Still, it is assumed that wind cooling works quickly enough to restore thermal equilibrium in this amount of time. The qualitative agreement with measurements (to be dealt with later in the chapter) regarding which side of the ship has the largest contrast, supports this assumption.

The computed scene and background radiances were exported from ShipIR and analyzed using an Interactive Data Language (IDL)[4] code. This way, the contrast could be computed using equation (2.21) as described in section 2.3. The ShipIR 'analyze image option' gives the contrast as the absolute value of the difference between the scene and the background and was therefore not used in our analysis. The model background was found to be highly isotropic horizontally, and therefore the contrast was found by subtracting the background from the scene directly without using different image areas as was done in the image analysis in chapter 3. It was found, however, that this operation had to be performed on a region of the simulated scene that excluded the horizon. The reason for this is that the horizon was always a straight line in the exported background image, but this was not always the case in the exported scene image. According to Davis, this is caused by the subimage procedure used to get better results for small targets. This effect caused a difference in the computed contrast of some W/sr.

ShipIR does not compute the target reflection in the sea or the ship wake. For the comparison with the camera images, the effect of these omissions is minimized by excluding the regions of the images where these effects are seen from the region used in the calculation of the apparent radiant intensity contrast. This is illustrated by looking at the

[4]IDL is a trademark of Research Systems, Inc

boxes in figure 3.9.

The computed ship temperatures were mainly read directly from the screen image in ShipIR, but could also be exported and analyzed in the manner described above.

The distance to the ship and the ship heading and bearing relative to the observer was computed using the Norwegian GPS-data. The data originally distributed assumed that the measurement platform was at the position quoted in (6), but the correct position turned out to be the position given in table 3.1. This discrepancy was corrected in our calculation. The resulting corrections are quite small.

4.1.1 MW apparent radiant intensity contrast comparisons

In the following sections, MW band ShipIR apparent radiant intensity contrast results are presented, and compared with available MW image data. We have chosen to run ShipIR simulations on runs with good image data and favorable weather conditions. The latter is mainly defined as clear sky. Some exceptions do exist. First, run 8 and run 31 are presented, then several C runs are presented in a separate section. There are 13 night runs in all, with two measurements obtained for each run, therefore the MW band D (night) run results will be presented separately.

4.1.1.1 A and B runs

Run 8 is a B run of particular interest due to additional MW image data from NRL, while run 31 is an A run from a day with a particularly clear sky. No more A or B runs were studied due to problems with several of the images, or poor weather conditions.

The weather data used to specify the background for run 8 is given by table 3.5. The air temperature and relative humidity values used are the average between the values measured on the shore and on the ship. Run 8 is a B-run (day run, sun-lit port side of ship visible, sun high in the sky) with a nominal ship course of 0°, see figure 3.2. The Norwegian MW image was obtained at a range[5] of 1105 m, see figure 3.9. The image from the Indigo Merlin camera (figure 3.11) was taken at 1005 m. Run 31 is an A run (shaded starboard side visible). A summary of the geometrical conditions for the simulations covered here is given in table 4.1.

The resulting ShipIR images for run 8 are shown in figures 4.5 and 4.6, while the image for run 31 is shown in figure 4.7.

The ShipIR images can not be directly compared visually with the camera images presented earlier since there is a lot of scaling involved in making the images (both camera and ShipIR) viewable after printing. Thus, only the relative brightness of each image can to a certain degree be compared. The brightness of the horizon may be the most useful guide to the relative brightness of the various images. Qualitatively, the images generated by ShipIR show many of the features that can be found in the camera images.

[5]The field of view of the MilCam camera was too narrow to allow images of CFAV Quest to be taken at the waypoint.

Run	IR sensor	Distance	Ship Speed	Nominal	True	Bearing
		(m)	(m/s)	heading	heading	
8p	MilCam (MW)	1105	5.1	0°	0.8°	112°
8p	Indigo (MW)	1005	4.8	0°	358.6°	89.2°
31s	MilCam (MW)	1100	5.1	270°	269.1°	152.1°

Table 4.1 A summary of the scenario geometries used in the MW band ShipIR calculations for runs 8 and 31.

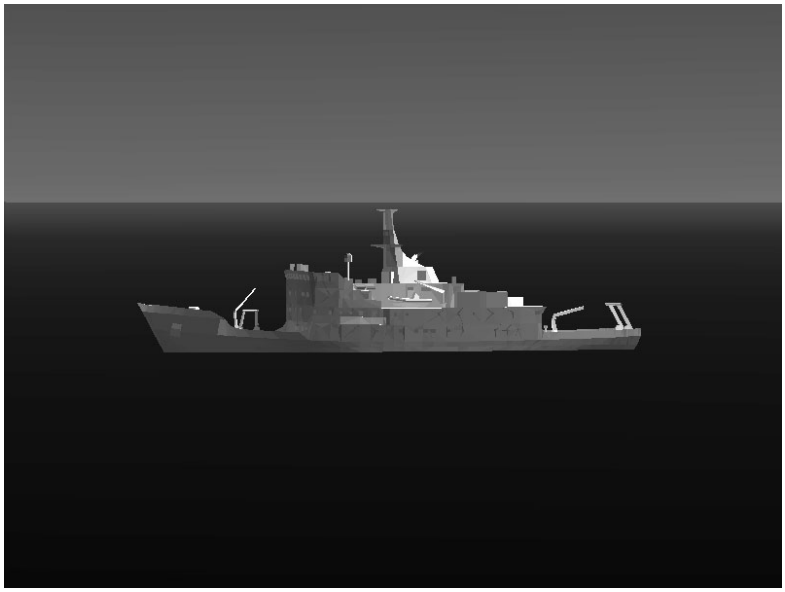

Figure 4.5 The ShipIR image of CFAV Quest for run 8 in the MW case with single scattering for the background calculation. The distance is 1105 m, and the field of view of the image is $5.9° \times 4.4°$.

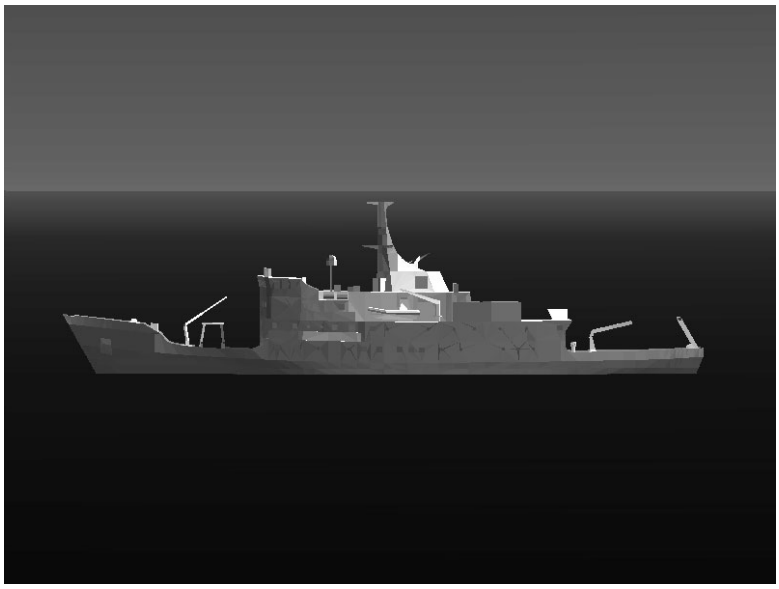

Figure 4.6 MW ShipIR image of CFAV Quest for run 8 be compared with the NRL Merlin data. The distance is 1005 m and the field of view of the image is $5.3° \times 4.0°$.

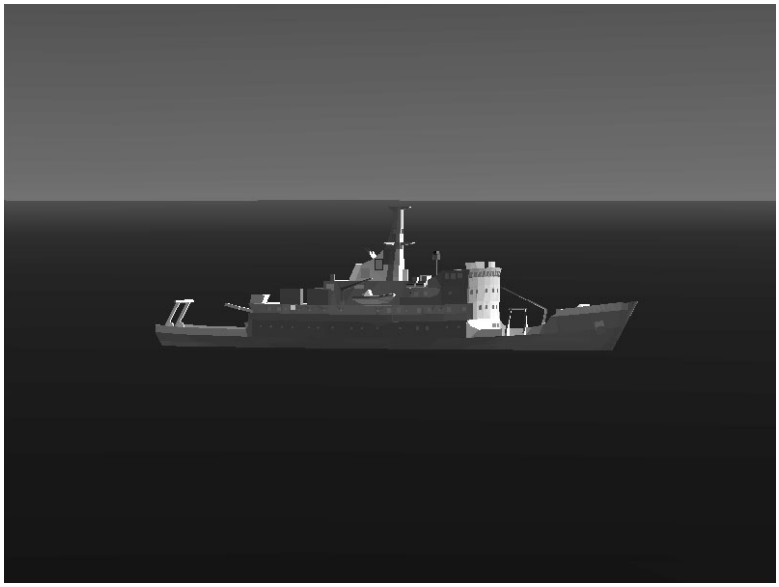

Figure 4.7 MW ShipIR image of CFAV Quest for run 31. The distance is 1100 m, and the field of view of the image is $5.9° \times 4.4°$

A comparison of the results obtained for the apparent radiant intensity contrast using the infrared images and using ShipIR is given in table 4.2. The contribution to the apparent

Run	IR sensor	Distance	Meas. contr.	Simulated contrast			
		(m)		no scattering		single scattering	
8p	MilCam	1105	125 W/sr	83 W/sr	-34 %	89 W/sr	-29 %
8p	Indigo	1005	111 W/sr	87 W/sr	-22 %	96 W/sr	-14 %
31s	MilCam	1100	99 W/sr	72 W/sr	-27 %	78 W/sr	-21 %

Table 4.2 Comparison of measurements and ShipIR simulations of the apparent radiant intensity contrast for run 8 (p indicates port aspect). The effect of scattered sunlight in the background calculation was investigated. The relative difference between the measurements and the ShipIR results is also included in the table.

radiant intensity contrast from solar radiation scattered on the background is shown in the table. For run 8 and run 31, scattering increases the apparent radiant intensity contrast by 7-10 %.

The ShipIR contrast intensity for run 8 is about 29 % lower than the contrast intensity computed for the MilCam MW image, and 14 % lower for the Indigo Merlin image.

To identify the sources of the contrast discrepancies, the contrast contributions of various parts of the ship were analyzed. The ship is divided into three horizontal areas, hull, superstructure and funnel. Figure 4.8 shows the superstructure region (defined by a red box)

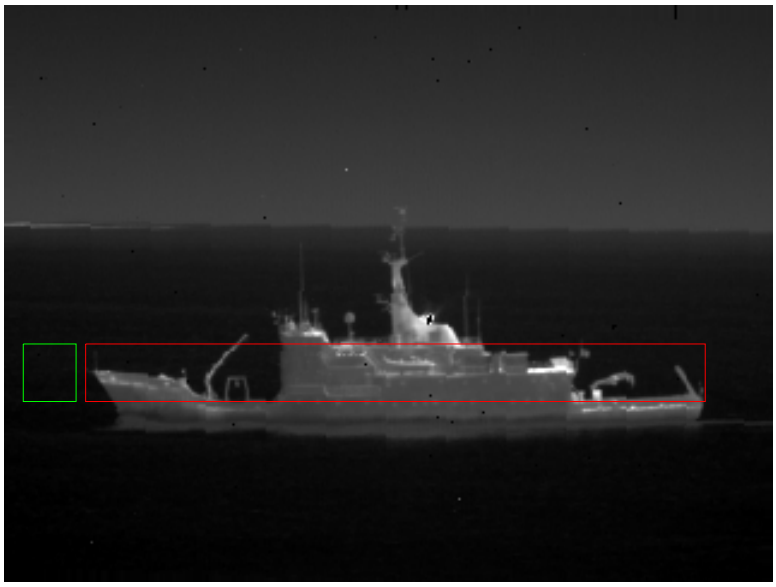

Figure 4.8 The red box defines the superstructure region used in the division of the ship in three parts. The hull is below this region while the funnel is above the superstructure region.

using the NRL run 8 image. The other two regions comprise the rest of the ship. The hull is below this region and the funnel above it. The contributions to the contrast from the

different parts of the ship are summarized in table 4.3. The contributions don't always add up exactly to the total contrast, especially for the contributions from the images. This is due to small positioning errors for the boxes defining the contributions.

Run	Part of ship	MW	
		Image	ShipIR
8p	Hull	33 W/sr	-18 %
8p	Superstructure	57 W/sr	-32 %
8p	Funnel	39 W/sr	-56 %
8p NRL	Hull	33 W/sr	-21 %
8p NRL	Superstructure	57 W/sr	-11 %
8p NRL	Funnel	21 W/sr	-10 %
31s	Hull	24 W/sr	-20 %
31s	Superstructure	57 W/sr	-35 %
31s	Funnel	21 W/sr	3 %

Table 4.3 Relative contributions to the apparent radiant intensity contrast from different parts of the ship from measurements and ShipIR simulations including scattering for run 8 and run 31.

For run 8, the hull and superstructure contrasts are fairly well described by the ShipIR predictions in both cases studied, while the funnel area contrast is more than 50 % lower than the contrast measured from the MilCam image. For the Indigo image, the funnel area contrast is very well represented by the ShipIR result. The overall agreement is quite good for run 8 in the MW band, the ShipIR predictions are 29 % lower than the measurements for the MilCam case and 14 % lower for the Indigo case.

For run 31, the overall agreement is quite good with predictions about 20 % lower than the observations. The funnel result is especially good in this case, while the predicted superstructure contrast is 35 % lower than the observed value.

4.1.1.2 C runs

In addition to the runs presented in the preceding paragraph, ShipIR calculations and comparisons with measurements were performed for several C runs (sun-lit port side, evening). The detailed run geometries are presented in table 4.4.

Meteorological data measured by the shore weather station were used in these simulations, see table C.6. Slightly different air temperature and relative humidity were measured on board the ship, but this effect is not considered for the C runs. For the D runs (night runs) some runs are simulated using both the shore and the ship values.

The results for the apparent radiant intensity contrast for the C runs are given in table 4.5, and illustrated in figure 4.9. The effect of solar scattering on the background is investigated. Single and multiple scattering calculations are performed for all the C runs.

Run	Distance	Ship speed	Nominal	True	Bearing
	(m)	(m/s)	heading	heading	
10	1152	5.1	32°	33.3°	152.1°
14	1177	5.4	32°	32.4°	155.1°
19	1119	5.3	32°	33.4°	149.9°
32	1063	4.9	32°	32.7°	142.5°

Table 4.4 A summary of the scenario geometries used in the MW C run ShipIR calculations. Runs included are 10, 14, 19 and 32.

Run	Dist	Measured	ShipIR with scattering (W/sr)		
	(m)	(W/sr)	none	single	multiple
10p	1152	144	146	169	176
14p	1177	148	184	214	220
19p	1119	146	175	209	217
32p	1063	121	175	193	198

Table 4.5 Comparison of measurements and ShipIR simulations for the C runs. The effect of including scattering in the background calculation was investigated. Runs include 10, 14, 19 and 32. Port or starboard side is indicated with a p or an s after the run number.

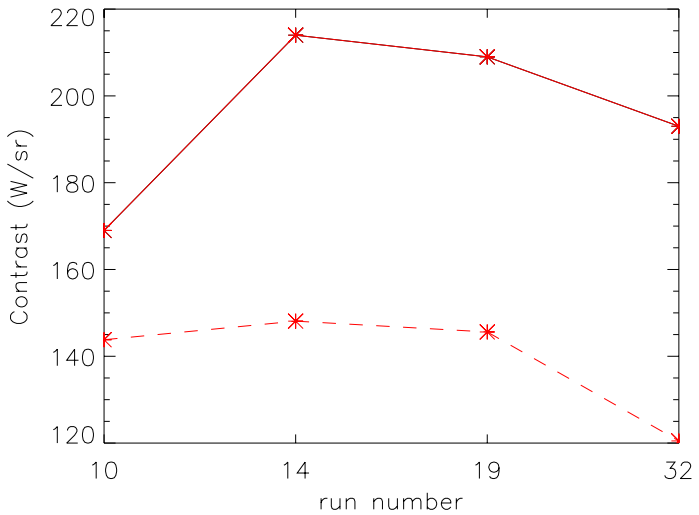

Figure 4.9 The calculated contrast (solid line) using single scattering and the measured contrast (dashed line) for runs 10, 14, 19 and 32 (C runs) are shown.

The deviations between the measured and the simulated contrast intensities are summarized in table 4.6. From the tables and figure 4.9, one sees that the calculated contrast is higher

Run	Measured	ShipIR with scattering		
	(W/sr)	none	single	multiple
10p	144	1 %	17 %	22 %
14p	148	24 %	45 %	49 %
19p	146	20 %	43 %	49 %
32p	121	45 %	60 %	64 %

Table 4.6 Deviations between measurements and ShipIR simulations for the C runs. The effect of including scattering in the background calculation was investigated. Runs include 10, 14, 19 and 32.

for all the C runs studied. With an exception for run 10, the deviation is almost the same for the runs studied.

The relative contributions to the contrast from the hull, superstructure and funnel regions for runs 10, 14, 19 and 32 are summarized in table 4.7. For run 10, the funnel area contrast

Run	Part of ship	MilCam	ShipIR
10	Hull	45 W/sr	49 %
10	Superstructure	75 W/sr	3 %
10	Funnel	32 W/sr	-24 %
14	Hull	42 W/sr	100 %
14	Superstructure	80 W/sr	20 %
14	Funnel	31 W/sr	6 %
19	Hull	44 W/sr	82 %
19	Superstructure	71 W/sr	34 %
19	Funnel	33 W/sr	3 %
32	Hull	49 W/sr	55 %
32	Superstructure	57 W/sr	53 %
32	Funnel	23 W/sr	30 %

Table 4.7 Relative contributions from parts of the ship to the apparent radiant intensity contrast from measurements and ShipIR simulations using the single scattering option for the C runs.

prediction is 24 % lower than the measurement, while the run 32 prediction is 30 % higher than the measurement. The funnel area prediction is in good agreement with the measurements for run 14 and 19. The hull predictions are between 50 % (run 10)–100 % (run 14) higher than the measured results. The superstructure predictions are 3 % (run 10) – 53 % (run 32) higher than the measured results.

4.1.1.3 D runs

During D runs (night runs), the ship made a 180° turn after the first way-point so that the other side of the ship could be measured a few minutes after the first measurement. Although the ship does not hold a steady course for 30 minutes, it is felt that the wind convection probably reaches steady state conditions fast enough that one can do a new simulation for this course. In day-time with sunshine, this would probably have led to greater problems. The effect of scattering is negligible at night, therefore scattering is not used in the calculation of night runs.

A summary of the geometrical conditions for the simulations covered here is given in table 4.8. The weather data used to specify the background for run 34 are given by table 3.7,

Run	Distance	Ship speed	Nominal	True	Bearing
	(m)	(m/s)	heading	heading	
11p	1166	5.2	32°	31.3°	155.2°
11s	1066	4.9	212°	222.5°	105.0°
12p	1161	5.1	32°	31.9°	153.5°
12s	1066	4.9	212°	215.4°	102.0°
15p	1190	5.3	32°	34.3°	156.6°
15s	1085	4.7	212°	213.0°	97.8°
16p	1115	5.2	32°	31.5°	149.9°
16s	1078	4.8	212°	209.5°	97.5°
20p	1081	5.2	32°	32.5°	145.1°
20s	1069	4.7	212°	214.2°	99.7°
21p	1118	5.3	32°	33.7°	149.5°
21s	1137	4.6	212°	216.8°	95.5°
26p	1083	5.2	32°	33.0°	143.0°
26s	1154	4.6	212°	217.7°	94.9°
27p	1120	5.2	32°	33.0°	148.7°
27s	1105	4.6	212°	214.4°	96.1°
34p	1103	4.9	32°	34.0°	147.5°
34s	1056	5.0	212°	212.8°	97.6°

Table 4.8 A summary of the scenario geometries used for the ShipIR night run calculations. Runs included are 11, 12, 15, 16, 20, 21, 26, 27 and 34. Only the MW band is simulated for most of these runs. Port and Starboard refers to contrast simulated for port and starboard aspects respectively.

while the meteorological data for the rest of the D runs studied are given in tables C.7 and C.8. The resulting port aspect ShipIR image of the ship for run 34 is shown in figure 4.10. The corresponding camera image is shown in figure 3.17.

For run 21 and 34, two different scenarios are studied using slightly different weather parameters. The base-line scenario, called the 'Shore' scenario, uses the weather data given

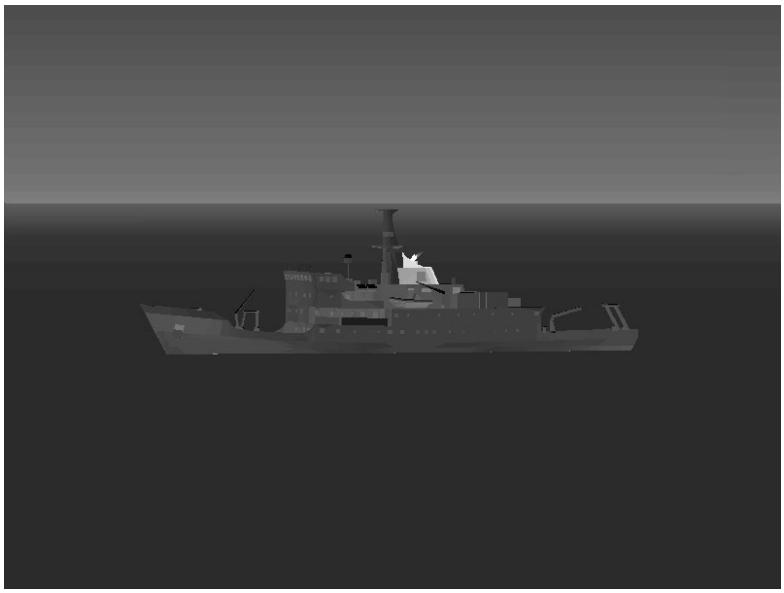

Figure 4.10 The ShipIR image of CFAV Quest for run 34 in the MW case. The distance is 1100 m, and the field of view of the image is $5.9° \times 4.4°$.

Parameter	Run 21	Run 34
Air temperature	15.8 °C	15.6 °C
Relative humidity	84.8 %	51.4 %

Table 4.9 Alternative meteorological parameters used for runs 21 and 34. The parameters are air temperature and relative humidity measured on the ship.

in table 3.7 and C.8 obtained at the shore station. The second scenario, the 'Ship' scenario uses air temperature and relative humidity as obtained by the weather station on board the CFAV Quest, but otherwise uses the shore station data. The 'Ship' scenario meteorological parameters employed for run 21 and 34 are given in table 4.9.

The reason for using different sets of input parameters is to study the effect of varying some of the meteorological parameters. It is not always clear which set of parameters would be the best to use in a given situation, therefore using several different parameter sets will cover some of the possibilities, and will indicate a range of uncertainty for the simulation results pertaining to the meteorological data. This is only done for the night runs, where we expect that our cameras perform best, the calculation time is much shorter since we don't have to worry about scattered sunlight, and we also expect the interpretation of ShipIR results to be easier without sunshine.

A comparison of the results obtained for these two runs for the apparent radiant intensity contrast using the infrared images and using ShipIR is given in table 4.10.

For run 21 and 34, the MW ShipIR results for port aspect are about 50–60 % lower than the result found from the corresponding camera image (slightly larger discrepancy for the starboard aspect). The agreement is slightly better when using the temperatures measured

Run	IR sensor	Dist	Meas.	ShipIR contrast			
		(m)	(W/sr)	Shore		Ship	
21p	MilCam (MW)	1118	42	16 W/sr	-62 %	19 W/sr	-55 %
21s	MilCam (MW)	1137	43	16 W/sr	-63 %	22 W/sr	-49 %
34p	MilCam (MW)	1103	47	20 W/sr	-57 %	24 W/sr	-49 %
34s	MilCam (MW)	1056	52	10 W/sr	-81 %	13 W/sr	-75 %

Table 4.10 Comparison of measurements and ShipIR simulations of the apparent radiant intensity contrast in the MW band for runs 21 and 34. Shore and Ship refers to meteorological parameters measured on the shore, and on the ship respectively. The additional input data for the latter case are given in table 4.9. p or s indicates port or starboard aspect respectively.

on board the ship in the simulations.

To identify the sources of the contrast discrepancies, the contrast contributions of various parts of the ship were analyzed. The contributions to the contrast from the different parts of the ship are summarized in table 4.11. The contributions don't always add up exactly to the total contrast, especially for the contributions from the images. This is due to small positioning errors for the boxes defining the contributions.

Run	Part of ship	MilCam	ShipIR	
		W/sr	Shore	Ship
21p	Hull	16	-75 %	-75 %
21p	Superstructure	17	-76 %	-71 %
21p	Funnel	8	13 %	13 %
34p	Hull	15	-67 %	-53 %
34p	Superstructure	22	-68 %	-59 %
34p	Funnel	12	-25 %	-17 %

Table 4.11 Relative contributions to the apparent radiant intensity contrast from different parts of the ship from measurements and ShipIR simulations for runs 21 and 34. Two different scenarios are included, 'Shore' and 'Ship'.

The results for the two night runs are quite similar. ShipIR predicts much lower contrasts 50–75 % in the MW band than observed for the hull and the superstructure regions, while the agreement is better for the funnel area, where the prediction is about 15 % higher than the measured contrast for run 21 and 20 % lower than the measured contrast for run 34. The overall agreement is poor in the MW band for these runs. The ShipIR prediction is 50–60 % lower than the measured contrast for the port aspect and 50–80 % lower for the starboard aspect depending on which input scenario one studies. The effect of changing the meteorological input is seen to be small.

In addition to the runs presented in the preceding paragraphs, ShipIR calculations and comparisons with measurements were performed in the MW band for all the night runs with

exception of run 39 and 40. The detailed run geometries of the night runs were presented previously in table 4.8.

The appropriate weather data are given in table C.7 and C.8. A summary of the simulated apparent radiant intensity contrasts in the MW band for the night runs is given in table 4.12. The simulations show that except for run 11, 12 and 34, starboard aspect has a higher

Run	11	12	15	16	20	21	26	27	34
Port (W/sr)	21	23	7	16	16	16	12	14	20
Starboard (W/sr)	15	16	26	22	22	16	28	24	10

Table 4.12 A summary of the simulated contrasts for the night runs. Port and Starboard refers to contrast simulated for port and starboard aspects respectively.

contrast than port aspect. Runs 11 and 12 are the only simulated runs where there was substantial cloud cover. Clouds were not taken into account in these simulations, and therefore the results for these two runs may deviate from the rest of the runs when compared with the measured data.

The simulated results are compared with the measured contrasts in figure 4.11. In general,

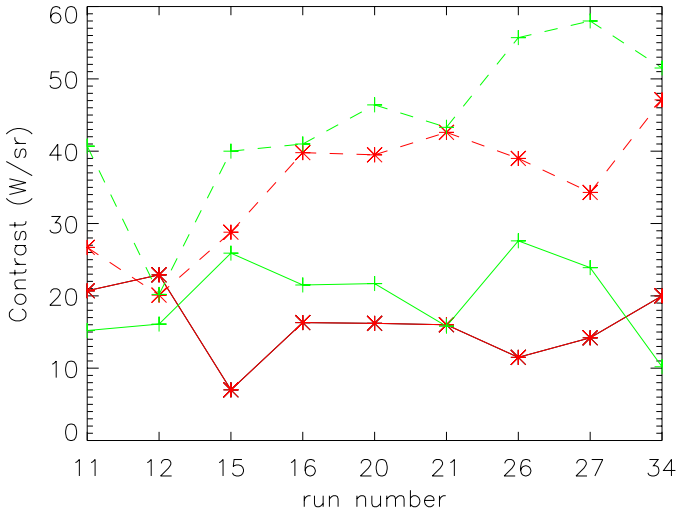

Figure 4.11 Measured contrasts (dashed lines) are compared with simulated contrasts for most of the SIMVEX night runs. The figure shows results for port (red) and starboard (green) aspects.

one can see that the simulated contrast is lower than the measured contrast for all runs with a near exception for run 12. Both measurements and simulations show higher contrast for the starboard side of the ship for most runs. Assuming that the inherent ship contrast should be virtually equal for the two sides, one has to look for an explanation for this behavior. During night runs, the only azimuth dependent heat contribution (neglecting the moon) can be attributed to the wind. The wind is found to blow from SW to N during the various night

runs. The ship has a course about NNE for the port measurement and SSW for the starboard measurements. The net wind felt by the ship is higher when the ship is heading in the direction of the wind, and this is most often the case for the starboard part of the runs since the wind is blowing from the west of south west for most of the runs. The exceptions are run 11, 12 and 34 when the wind is blowing from the north. As mentioned, these are the only runs when the contrast on the port side is higher than on the starboard side. This also illustrates that the wind does not have a net cooling effect on the ship during the night runs. The air temperature is higher than the temperature that would have been achieved by the cold parts of the ship if radiation was the only way of balancing the energy and no convection was present. The ship thus experiences a net wind warming effect. This is further discussed in chapter 3. A summary of the relevant wind directions is given in figure 3.24.

In addition to wind, the heading of the ship relative to the measurement site may introduce a slight variation in the effective area seen from NESTRA from one measurement to the next. Also, different parts of the ship may be visible, which may have different contrasts. This will introduce a variation in contrast from run to run independent of the wind convection. This variation may also be different for the two measurements taken of the ship for each run.

4.1.2 LW apparent radiant intensity contrast comparisons

LW ShipIR results were obtained for a few runs only, due to the LW camera instability and lack of relative response mentioned earlier. These runs are presented briefly in this section. It is not known what effect the ideal response assumed in the LW band has on the calculated contrast of the various parts of the ship. The instability of the camera during day-time operation further adds to the uncertainty of the comparison. The results presented in this section must therefore be interpreted with caution.

A summary of the geometrical conditions for the simulations covered here is given in table 4.13.

Run	Distance (m)	Ship Speed (m/s)	Nominal heading	True heading	Bearing
8p	1105	5.1	0°	0.8°	112°
21p	1118	5.3	32°	33.7°	149.5°
21s	1137	4.6	212°	216.8°	95.5°
31s	970	5.1	270°	268.9°	180.0°
32p	990	4.9	32°	32.0°	122.0°
34p	1000	4.9	32°	29.8°	120.9°
34s	992	5.1	212°	209.4°	121.3°

Table 4.13 A summary of the scenario geometries used in the LW band ShipIR calculations.

4.1.2.1 Day runs

Run 8 is one of the runs covered in chapter 3, and is therefore also simulated in the LW band. Run 8 is a B-run (day run, sun-lit port side of ship visible) with a nominal ship course of 0°, see figure 3.2. The resulting ShipIR image for run 8 is shown in figure 4.12 and can be compared with the Sentinel image, figure 3.10.

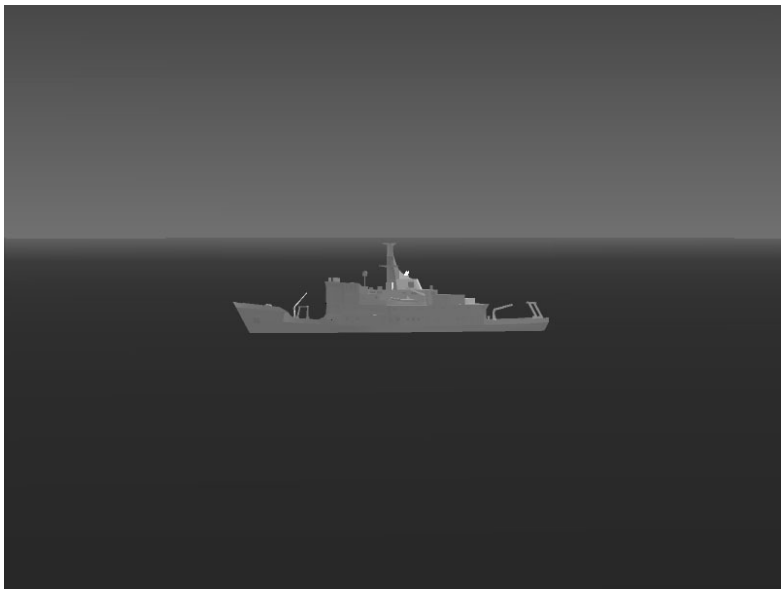

Figure 4.12 The ShipIR image of CFAV Quest for run 8 in the LW case. The distance is 1105 m, and the field of view of the image is $9.33° \times 7.0°$.

LW band ShipIR calculations and comparisons with measurements were also performed for run 31 (A run, shaded starboard side) and 32 (C run, sun-lit port side). Thus, one day run of each type is featured. The results for the apparent radiant intensity contrast for runs 8, 31 and 32 are given in table 4.14.The contribution to the apparent radiant intensity contrast

Run	Distance	Meas. contr.	Simulated contrast (W/sr)	
	(m)	(W/sr)	no scatt	single scatt
8p	1105	2168	3702	3920
31s	970	1681	4839	-
32p	990	3812	5925	6317

Table 4.14 Comparison of measurements and ShipIR simulations of the apparent radiant intensity contrast for the LW day runs (p indicates port aspect, s indicates starboard aspect). The effect of scattered sunlight in the background calculation was investigated.

from solar radiation scattered on the background is also shown in this table.

The relative differences between the measurements and the ShipIR results for the day runs are summarized in table 4.15.

Run	Measured	ShipIR with scattering	
	(W/sr)	none	single
8p	2168	71 %	81 %
31s	1681	188 %	- %
32p	3812	55 %	66 %

Table 4.15 Relative differences between day-time LW band measurements and ShipIR simulations. The effect of including scattering in the background calculation was investigated.

For runs 8, 31 and 32, the effect of solar scattering on the background is investigated. For run 8, scattering increases the apparent radiant intensity contrast by 5 % in the LW band. The deviations between the measured and the simulated contrast intensities are summarized in table 4.15. The Sentinel camera results from run 31 must be dismissed. It is thus impossible to say anything about the agreement for this case.

To identify the sources of the contrast discrepancies, the contrast contributions of various parts of the ship were analyzed. The relative contributions to the contrast from the hull, superstructure and funnel regions for runs 8, 31 and 32 are summarized in table 4.16. The contributions don't always add up exactly to the total contrast, especially for the contributions from the images. This is due to small positioning errors for the boxes defining the contributions.

Run	Part of ship	Sentinel	ShipIR
8p	Hull	628 W/sr	140 %
8p	Superstructure	1315 W/sr	48 %
8p	Funnel	305 W/sr	54 %
31s	Hull	-	-
31s	Superstructure	-	-
31s	Funnel	-	-
32p	Hull	1224 W/sr	95 %
32p	Superstructure	2059 W/sr	54 %
32p	Funnel	649 W/sr	15 %

Table 4.16 Relative contributions from parts of the ship to the apparent radiant intensity contrast from measurements and ShipIR simulations using the single scattering option.

For run 8, the hull contribution seems grossly exaggerated by ShipIR, being 140 % larger than the image contrast. Both the superstructure and the funnel regions are predicted to have a contrast that is about 50 % higher than the measured contrast. The overall agreement is poor, with predictions being 81 % higher than the image value.

For run 32, the agreement is poor. The predictions are 55–95 % higher than the observations for the hull and superstructure contrasts. The predicted funnel contrast is about

15 % higher than observed.

4.1.2.2 Night runs

A summary of the geometrical conditions for the night run simulations covered here is given in table 4.13. For the night runs, both port and starboard aspects are covered in the measurements as the ship made an 180° turn shortly after passing of the waypoint. Although the ship does not hold a steady course for 30 minutes, it is felt that the wind convection reaches steady state fast enough that one can do a new simulation for this course. To save calculation time, the weather data are assumed to be the same as for the port measurement. With reasonably stable weather conditions, this simplification should not greatly influence the results.

For run 21 and 34, as for the MW band, two different scenarios are studied using slightly different weather parameters. The base-line scenario, called the 'Shore' scenario, uses the weather data obtained at the shore station which are given in table 3.7 and C.8. A second scenario, the 'Ship' scenario uses air temperature and relative humidity obtained by the weather station on board the CFAV Quest, but otherwise uses the shore station data. The 'Ship' scenario meteorological parameters employed for run 21 and 34 are given in table 4.9.

The resulting images of the ship for both aspects for run 34 are shown in figure 4.13 and 4.14. The corresponding port aspect camera image is shown in figure 3.18.

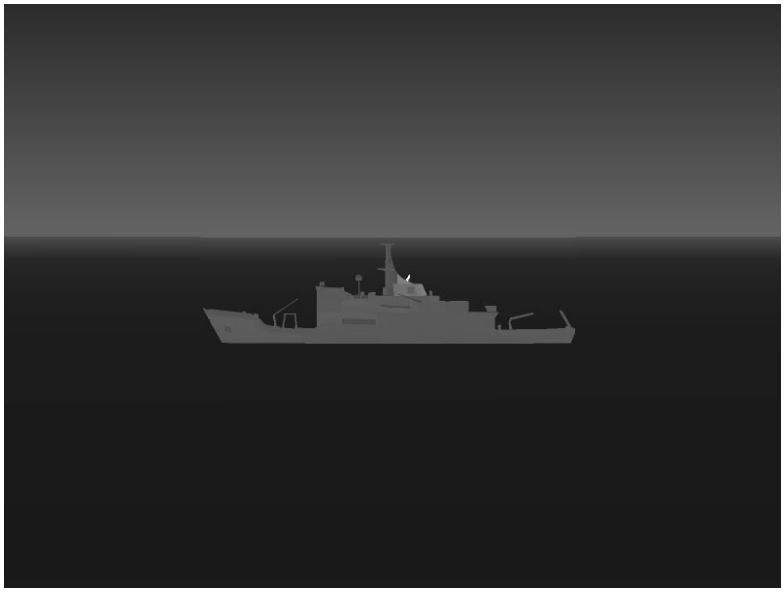

Figure 4.13 The port aspect ShipIR image of CFAV Quest for run 34 in the LW case. The distance is 1000 m, and the field of view of the image is $9.3° \times 7.0°$.

The comparison of apparent radiant intensity contrast for the night runs are presented in table 4.17.

The effect of scattering is negligible for night runs, therefore scattering is not used in the

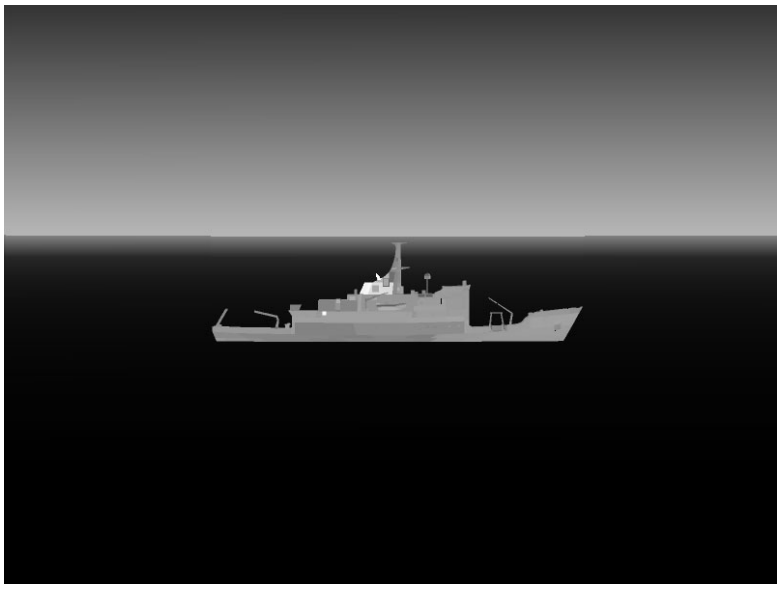

Figure 4.14 The starboard aspect ShipIR image of CFAV Quest for run 34 in the LW case. The distance is 1000 m, and the field of view of the image is $9.3° \times 7.0°$.

Run	Distance	Meas. contr.	Sim contr.(W/sr)	
	(m)	(W/sr)	Shore	Ship
21p	1118	1988	1272	1257
21s	1137	1878	1336	1327
34p	1000	2659	2979	3077
34s	992	2453	2764	2823

Table 4.17 Comparison of measurements and ShipIR simulations of the apparent radiant intensity contrast for runs 21 and 34 in the LW band. Shore and Ship refers to meteorological parameters measured on the shore, and on the ship respectively. The additional input data for the latter case are given in table 4.9. p or s indicates port or starboard aspect respectively.

calculation of night runs. The relative differences between the measurements and the ShipIR results are summarized in table 4.18. The effect of changing the meteorological

Run	Meas. contr.	Sim. contr.(W/sr)	
	(W/sr)	Shore	Ship
21p	1988	-36 %	-37 %
21s	1878	-29 %	-29 %
34p	2659	12 %	16 %
34s	2453	13 %	15 %

Table 4.18 Relative differences between measurements and ShipIR simulations of the apparent radiant intensity contrast in the LW band for runs 21 and 34. Two different scenarios are presented, 'Shore', 'Ship'.

input is seen to be small.

For run 34, the ShipIR LW contrast intensity is 13–26 % higher than the contrast intensity computed for the Sentinel image. It can be noted that for run 21, the ShipIR result is 35 % *lower* than the contrast intensity computed from the Sentinel image.

The contributions to the contrast from the different parts of the ship are summarized in table 4.19 for port aspect only.

Run	Part of ship	Sentinel	ShipIR	
		W/sr	Shore	Ship
21p	Hull	554	-4 %	-5 %
21p	Superstructure	1124	-50 %	-49 %
21p	Funnel	330	-48 %	-52 %
34p	Hull	729	72 %	86 %
34p	Superstructure	1490	-5 %	-6 %
34p	Funnel	429	-21 %	-19 %

Table 4.19 Relative deviations between measurements and ShipIR simulations of contributions to the apparent radiant intensity contrast in the LW band from different parts of the ship for runs 21 and 34. Two different scenarios are included, 'Shore' and 'Ship'.

The predicted port aspect contrast for run 34 for the superstructure is in close agreement with the measurements, while the predicted hull contrast is about 70–85 % higher than the observed contrast. The funnel area is underpredicted by about 20 %. Overall, the results agree fairly well with ShipIR predictions being about 15 % higher than the observed contrast.

The run 21 predictions, on the other hand, agree well with the observations for the hull part. The superstructure and funnel parts are predicted to be about 40–50 % lower than the observed values. For run 34, the hull prediction was about 70–85 % higher than the

observations, and the superstructure prediction was in good agreement. Thus, the run 21 predictions are lower relative to the measured results for all three regions of the ship.

4.1.3 Effect of the subimage procedure

In order to improve accuracy, targets smaller than half the window size in any direction can be enlarged in ShipIR using a procedure called subimage. The user can choose whether to use subimage or not. The default setting in ShipIR on SGI platforms is to have subimage on. For the distances and fields of view in this report, the subimage procedure will only take effect in the LW images.

In the contrast calculations, the subimage procedure introduces false contrasts in the background since the subimage is only used for the scene background, and not for the background image that is subtracted from the scene. The improved resolution of the background in the scene image means that the subtracted backgrounds aren't the same, and one gets a contrast in the net background. This is illustrated in the following two images, figures 4.15 and 4.16.

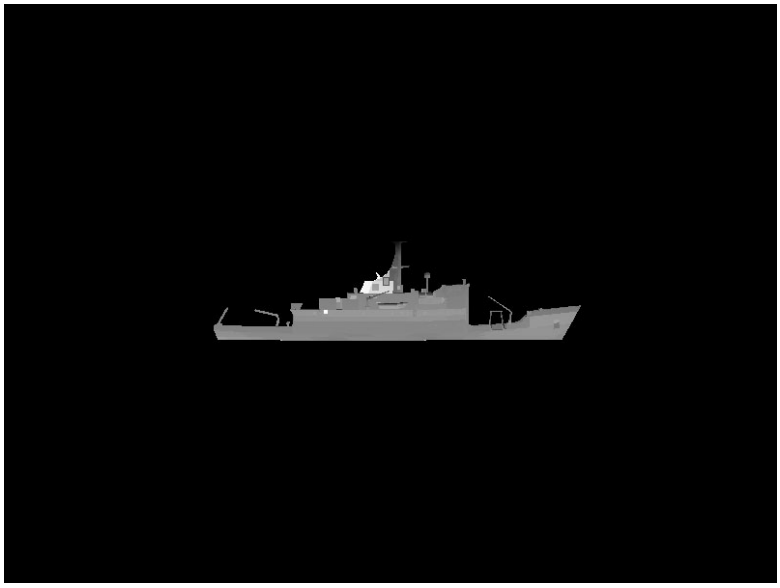

Figure 4.15 Contrast image of run 34 starboard aspect with ship temperature and relative humidity. Subimage off.

The background should of course have been completely black in this image, and is if the subimage procedure is not invoked.

The line over the ship is the main contrast contributor and is due to a problem with the position of the horizon caused by the subimage procedure. If one overexposes the ship, one can see that there is structure in the background (figure 4.16). The ship is close to the horizon in all the images used in the analysis in this report. Therefore, the radiance gradient in the sea near the horizon will show up strongly in the subimage contrast images. Table 4.20 gives the contrast computed by ShipIR with subimage on and off.

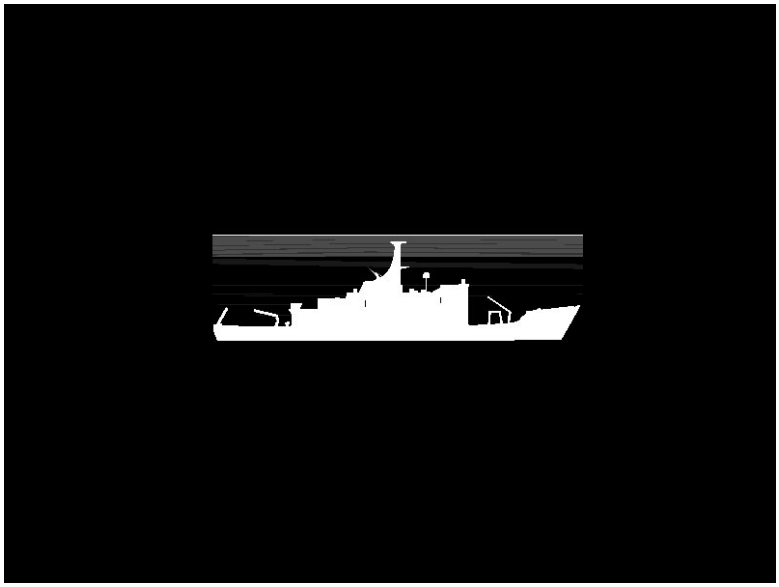

Figure 4.16 *Contrast image of run 34 starboard aspect with ship temperature and relative humidity. Subimage on. The ship is heavily overexposed to show fine detail in the background caused by the subimage procedure.*

Run	Distance	Meas. contr.	Sim. contrast (W/sr)	
	(m)	(W/sr)	Subimage on	Subimage off
8p	1105	2168	3735	3702
21p	1118	1988	1291	1272
21s	1137	1878	1341	1336
31s	970	1681	4889	4839
32p	990	3812	5953	5925
34p	1000	2659	3040	2979
34s	992	2453	2718	2720

Table 4.20 *Comparison of measurements and ShipIR simulations in the LW band of the apparent radiant intensity contrast with and without using the subimage procedure. p or s indicates port or starboard aspect respectively. No scattering, and meteorological parameters are measured at the shore station, except for run 8 where the average between shore and ship values is used.*

All the calculations in the table are performed without taking scattering into account. The effect is noticeable for all the runs, although not highly important.

4.2 Temperature comparisons

In addition to the comparison of the apparent radiant contrast intensity computed by ShipIR with that obtained directly from the IR images, the plate temperatures computed by ShipIR can be compared with the temperatures measured at several different locations on the ship. The measurement setup has been described in the Davis SIMVEX Trial Instrumentation plan (5). I-buttons and high- and low-temperature thermocouple wires are used for the temperature measurements. I-buttons have a temperature resolution of only 0.5 K. In the following sections, the thermocouple wire results are assumed to be more accurate than the I-button results.

The temperatures computed by ShipIR for run 8 (day run, sun-lit side) are shown as a color coded image of the scene in figure 4.17. The aspect angle and the color coding used in the

Figure 4.17 *A temperature map of the scene for run 8. The aspect and the color coding is the same as in figure 3.12. Note that calculated temperatures are shown, not equivalent temperatures.*

figure is the same as in figure 3.12. Comparing figure 4.17 to figure 3.12, one must take into account that figure 4.17 shows actual calculated temperatures while figure 3.12 shows equivalent blackbody temperatures. The difference is especially obvious for the sea surface. The Italian results (figures 3.14 and 3.15) show temperatures in the target plane, and can thus be more readily compared with the above result. However, the Italian temperature results assume both a transmission of 1.0 and an emissivity of 1.0, and should therefore not give completely accurate results. Also, it is not clear why the Italian images are so different from each other. For the ship, the different reflectivity (see figure 4.2) in the two wavelength bands may explain the difference. The sea emissivity, however, should be about the same in

the two bands, and the sea should therefore look the same for the same angle if the atmospheric transmission is the same.

A few temperature sensors have been chosen for comparison with the temperatures calculated by ShipIR. The names of these sensors, a description of their position and the ShipIR plate name corresponding to this position are given in table 4.21 for the port side and table 4.22 for the starboard side of the ship.

Plate name	Sensor	Description
sup1_P_P2	I102	Hull below RIB
sup2_P_P11	T21	Wall of deckhouse
sup2_P_P4	T1	Side of bridge
door_01_P1	I37	Door by ladder
door_02_P1	I38	Door near RIB
fore_rail_P_P3	I24	Bow railing
funnel_rail_P1	T14	Funnel rail
funnel_P21	T2/T3	Side of funnel
mpde_P5	K18	MPDE outlet

Table 4.21 A list of port side temperature sensors used in the comparison with temperatures calculated by ShipIR. Plate name is an identification used by ShipIR.

Plate name	Sensor	Description
sup2_S_P1	T20	Wall of deckhouse
funnel_rail_P2	T15	Funnel rail
funnel_P18	T4/T5	Side of funnel
mpde_S5	K21	MPDE outlet

Table 4.22 A list of starboard side temperature sensors used in the comparison with temperatures calculated by ShipIR. Plate name is an identification used by ShipIR.

The ShipIR plate names are given in the tables to identify the sensor locations. I-buttons are identified by a number preceded by an I, while the low temperature thermocouple wires are identified by a number preceded by a T, and the high temperature thermocouple wires are identified by a number preceded by a K. The location of the sensors used in this comparison is indicated in figures 4.18 (port) and 4.19 (starboard).

First, we look at run 8. Table 4.23 details the comparison between temperatures computed by ShipIR and temperatures measured by various sensors on the CFAV Quest for this run.

It is hard to identify a trend in the results. Some ShipIR temperatures are higher and some are lower than the measured temperatures, but overall, the agreement is quite good. The hot funnel and funnel outlet, however, are not well represented by the ShipIR calculation.

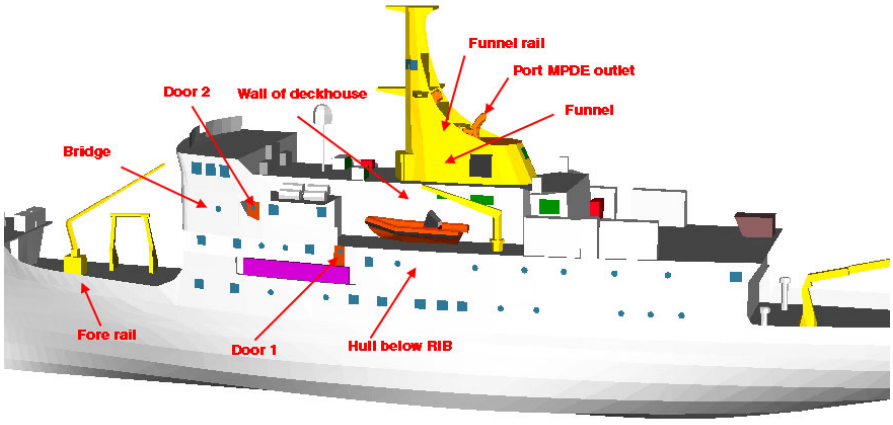

Figure 4.18 The approximate location of the port side temperature sensors used in the comparison with the temperatures computed by ShipIR is shown.

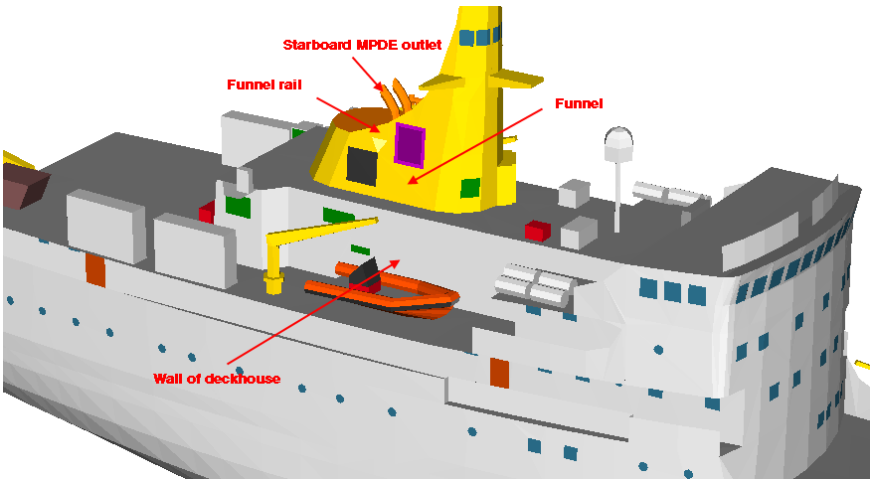

Figure 4.19 Approximate location of the starboard side temperature sensors used in the comparison with the plate temperatures computed by ShipIR.

Plate name	Sensor	ShipIR	Measured	Description
		($°C$)	($°C$)	
sup1_P_P2	I102	19.8	20.5	Hull below RIB
sup2_P_P11	T21	22.4	19.8	Wall of deckhouse
sup2_P_P4	T1	18.9	19.4	Side of bridge
door_01_P1	I37	19.3	19.0	Door by ladder
door_02_P1	I38	19.8	24.0	Door near RIB
fore_rail_P_P3	I24	19.5	19.5	Bow railing
funnel_rail_P1	T14	34.3	29.9	Funnel rail
funnel_P21	T2/T3	30.1	26.3	Side of funnel
mpde_P5	K18	111.3	121.4	MPDE outlet

Table 4.23 Comparison between ShipIR temperatures and measured temperatures for run 8 at various locations on CFAV Quest. $T_{air} = 19.6\ °C$ *and* $T_{sea} = 15.2\ °C$.

Run 32 is chosen for another sun-lit day run comparison. Table 4.24 gives the measured and the simulated temperatures for several locations on the ship.

Plate name	Sensor	ShipIR	Measured	Description
		($°C$)	($°C$)	
sup1_P_P2	I102	24.0	13.5	Hull below RIB
sup2_P_P11	T21	22.5	22.4	Wall of deckhouse
sup2_P_P4	T1	22.9	22.7	Side of bridge
door_01_P1	I37	19.1	16.0	Door by ladder
door_02_P1	I38	28.8	15.0	Door near RIB
fore_rail_P_P3	I24	20.9	14.0	Bow railing
funnel_rail_P1	T14	35.8	32.9	Funnel rail
funnel_P21	T2/T3	34.8	31.5	Side of funnel
mpde_P5	K18	116.2	122.7	MPDE outlet

Table 4.24 Comparison between ShipIR temperatures and measured temperatures for run 32 (day run, sun-lit port side) at various locations on CFAV Quest. $T_{air} = 19.3\ °C$ *and* $T_{sea} = 17.3\ °C$.

For run 32, the temperature discrepancies are larger than for run 8. The ShipIR temperatures are now too high for the doors, bow railing and hull, and slightly high for the funnel plates, while the deckhouse wall and side of bridge temperatures are in good agreement. The I102-result, which is several degrees lower than both air and sea temperature while the plate should be sun-lit, looks strange. The ShipIR value is very much higher than the measurement for this case. A comment can be made regarding the temperature of the two doors presented. Looking closely at the model, is it found that door 1 (see table 4.24) is in the shade while door 2 is sun-lit. This at least qualitatively explains the large temperature difference calculated by ShipIR. However, it does not explain why the measurements don't show the expected temperature difference, as the measured door 2

temperature is lower than the measured door 1 temperature!

Run 31 shows the starboard side of the ship. The run is a day run, but the measured side of the ship is in the shade. Table 4.25 gives the measured and simulated temperatures from

Plate name	Sensor	ShipIR	Measured	Description
		($°C$)	($°C$)	
sup2_S_P1	T20	18.4	19.6	Wall of deckhouse
funnel_rail_P2	T15	24.0	24.2	Funnel rail
funnel_P18	T4/T5	24.3	24.0	Side of funnel
mpde_S5	K21	124.9	122.5	MPDE outlet

Table 4.25 Comparison between ShipIR temperatures and measured temperatures for run 31 (day run, starboard side - shaded) at various locations on CFAV Quest. $T_{air} = 20.5\ °C$ and $T_{sea} = 17.3\ °C$.

several locations on the ship. The locations of the temperature sensors are indicated in figure 4.19. For this run, the agreement is quite good for all sensors included.

Solar heating makes the interpretation of the day runs complicated. Night runs should be easier to analyze in this respect with the major external heat source out of the picture. Tables 4.26 and 4.27 detail the temperature comparison for run 21 and 34. In both cases, simulations have been performed using air temperature and relative humidity measured on the ship as well as on shore.

Plate name	Sensor	ShipIR ($°C$)		Meas.	Description
		Shore	Ship	($°C$)	
sup1_P_P2	I102	11.4	13.2	12.5	Hull below RIB
sup2_P_P11	T21	12.0	13.9	15.7	Wall of deckhouse
sup2_P_P4	T1	11.4	13.2	16.0	Side of bridge
door_01_P1	I37	12.5	14.4	15.5	Door by ladder
door_02_P1	I38	12.3	14.2	14.0	Door near RIB
fore_rail_P_P3	I24	11.6	13.4	13.3	Bow railing
funnel_rail_P1	T14	20.3	22.2	23.3	Funnel rail
funnel_P21	T2/T3	17.5	19.4	21.3	Side of funnel
mpde_P5	K18	111.5	112.1	115.4	MPDE outlet

Table 4.26 Comparison between ShipIR temperatures and measured temperatures for run 34 at various locations on the port side of CFAV Quest. Two cases are analyzed, differing only in input meteorological parameters. The two cases are labeled Shore and Ship. The air temperature measured on the shore was 13.6 °C while the temperature measured on the ship was 15.6 °C. The sea temperature was 16.7 °C. All the meteorological parameters are given in tables 3.7 and 4.9.

Plate name	Sensor	ShipIR ($°C$)		Measured	Description
		Shore	Ship	($°C$)	
sup1_P_P2	I102	12.7	13.5	14.0	Hull below RIB
sup2_P_P11	T21	12.9	13.7	15.3	Wall of deckhouse
sup2_P_P4	T1	12.7	13.5	15.4	Side of bridge
door_01_P1	I37	13.4	14.3	16.5	Door by ladder
door_02_P1	I38	13.5	14.4	16.0	Door near RIB
fore_rail_P_P3	I24	12.8	13.6	15.0	Bow railing
funnel_rail_P1	T14	24.7	25.5	25.5	Funnel rail
funnel_P21	T2/T3	19.4	20.2	24.0	Side of funnel
mpde_P5	K18	116.6	116.9	124.2	MPDE outlet

Table 4.27 Comparison between ShipIR temperatures and measured temperatures for run 21 at various locations on the port side of CFAV Quest. $T_{sea} = 15.9\ °C$, $T_{air} = 14.9\ °C$ for the Shore scenario, and $T_{air} = 15.8\ °C$ for the Ship scenario.

For these runs, all the ShipIR temperatures of the ship hull and superstructure excluding the funnel areas are too low for the 'Shore' scenario, while the computed temperature of the hot funnel outlet is in quite good agreement with the measured temperature. The agreement is somewhat improved in the 'Ship' scenario. For run 21, the sea temperature is lower and the air temperature higher than for run 34. Most of the measured and computed temperatures are higher than for run 34 as expected from the higher air temperature.

Using shore meteorological data only, a comparison has been made for several C runs. The calculated temperatures are given in table 4.28, while the measured temperatures are given in table 4.29. The temperature comparison results for the C runs are also illustrated in

ShipIR ($°C$)				Description
10	14	19	32	Run number
22.5	27.0	26.8	24.1	Hull below RIB
22.4	25.8	26.5	22.6	Wall deckhouse
21.6	25.3	25.2	23.1	Side of bridge
18.2	18.1	18.6	19.1	Door by ladder
26.7	36.2	37.5	29.1	Door near RIB
19.8	20.3	21.2	21.0	Bow railing
37.5	46.2	46.7	35.9	Funnel rail
32.8	39.5	40.0	35.2	Side of funnel
118.0	121.2	121.6	117.7	MPDE outlet

Table 4.28 Temperatures computed by ShipIR for the C runs using Shore meteorological data and the single scattering option.

figures 4.20 and 4.21.

Sensor	ShipIR ($°C$)				Description
	10	14	19	32	Run number
I102	14.0	13.0	14.5	13.5	Hull below RIB
T21	21.1	22.0	22.1	22.3	Wall deckhouse
T1	21.1	21.3	21.7	22.6	Side of bridge
I37	16.5	16.0	17.0	15.8	Door by ladder
I38	15.5	15.0	16.5	15.0	Door near RIB
I24	14.5	14.0	16.0	14.0	Bow railing
T14	32.2	34.5	35.4	32.9	Funnel rail
T2/T3	29.5	35.9	34.4	31.4	Side of funnel
K18	121.5	131.1	123.9	122.7	MPDE outlet
T_{air}	18.4	15.6	17.1	19.3	Air temperature
T_{sea}	15.1	16.0	16.1	17.3	Sea temperature

Table 4.29 Measured temperatures for the port side of CFAV Quest for the C runs. Measured air and sea temperatures are also included for convenience.

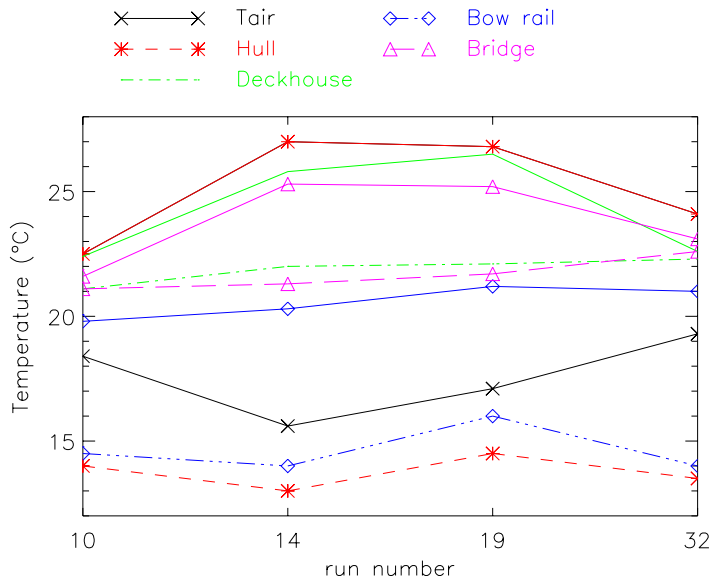

Figure 4.20 Comparison of calculated and measured temperatures for selected parts of the ship for several C runs. The ShipIR temperatures are shown using solid lines, while the line styles of the measured temperatures change.

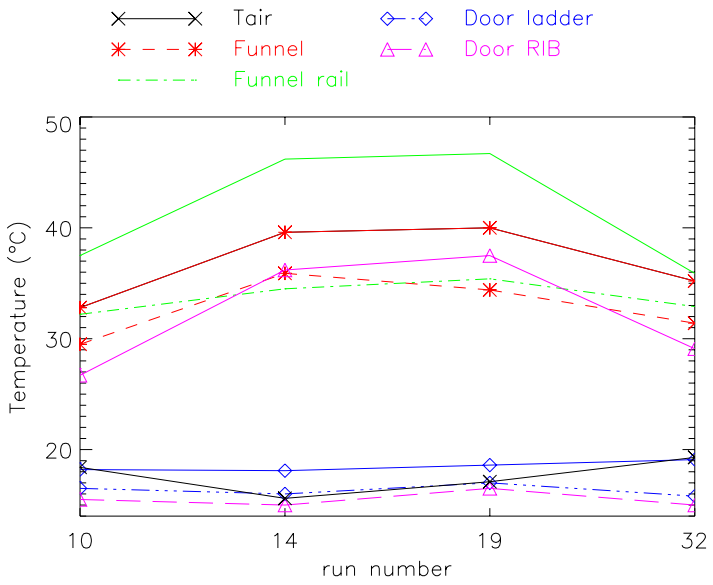

Figure 4.21 *Comparison of calculated and measured temperatures for selected parts of the ship for several C runs. The ShipIR temperatures are shown using solid lines, while the line styles of the measured temperatures change.*

The calculated temperatures are typically higher than the measured temperatures. There is not much correlation with the air temperature.

Using shore meteorological data only, a comparison has been made for both aspects for almost all the D runs. The calculated temperatures for the port side are given in table 4.30, while the measured temperatures are given in table 4.31. The night-time port side temperatures are plotted in figures 4.22 and 4.23.

The temperatures follow the variation in the air temperature quite closely. In figure 4.22, all the calculated temperatures are almost identical, but the corresponding measured temperatures differ by several degrees. All the measured temperatures in figures 4.22 and 4.23 are higher than the calculated temperatures. As the ShipIR calculation uses the temperatures measured by the shore station which is typically lower than the temperatures measured by the ship station, this makes sense. Still, the results in tables 4.26 and 4.27 indicate that even using temperatures measured by the ship weather station, most measured temperatures would be higher than the calculated temperatures.

For the starboard side, the calculated temperatures are given in table 4.32, while the measured temperatures are in table 4.33.

The night-time starboard side temperatures are plotted in figure 4.24. The trend is the same as for the port side temperatures. The calculated temperatures are lower than the measured temperatures, and the temperature variation from run to run basically follow the air temperature.

In conclusion, ShipIR seems to underestimate the temperatures of the hull and superstructure at night. The temperatures of the hull, bridge and deckhouse wall are

ShipIR (°C)									Description
11	12	15	16	20	21	26	27	34	Run number
12.2	11.9	10.5	11.2	13.3	12.7	13.0	13.2	11.4	Hull below RIB
12.9	12.4	10.8	11.5	13.6	12.9	13.3	13.4	12.0	Wall deckhouse
12.3	11.9	10.5	11.2	13.3	12.7	13.0	13.2	11.4	Side of bridge
13.4	12.9	11.4	12.2	14.4	13.4	14.1	14.1	12.5	Door by ladder
13.2	12.9	11.7	12.1	14.2	13.5	13.9	14.0	12.3	Door near RIB
12.4	12.1	10.5	11.3	13.4	12.8	13.0	13.2	11.6	Bow railing
21.2	20.6	26.2	23.0	26.8	24.7	28.7	28.0	20.3	Funnel rail
18.1	17.9	19.6	17.9	21.0	19.4	22.2	21.4	17.5	Side of funnel
111.6	110.6	116.4	116.0	116.9	116.6	117.2	117.0	111.5	MPDE outlet

Table 4.30 Temperatures computed by ShipIR for the port side of CFAV Quest for the night runs using Shore meteorological data.

Sensor	ShipIR (°C)									Description
	11	12	15	16	20	21	26	27	34	Run number
I102	13.0	12.5	12.5	12.5	14.0	14.0	14.5	14.0	12.5	Hull below RIB
T21	15.9	15.5	14.1	14.0	15.3	15.3	16.0	16.1	15.7	Wall deckhouse
T1	16.3	15.8	14.7	14.5	15.8	15.4	16.6	16.4	16.0	Side of bridge
I37	15.5	15.0	15.5	15.0	16.5	16.5	17.5	17.0	15.5	Door by ladder
I38	14.5	14.0	14.5	14.0	16.0	16.0	16.5	16.0	14.0	Door near RIB
I24	14.0	13.0	13.5	13.0	15.5	15.0	15.5	15.0	13.3	Bow railing
T14	23.9	24.0	26.2	24.6	26.6	25.5	26.0	27.5	23.3	Funnel rail
T2/T3	21.4	21.4	24.0	23.3	24.9	24.0	24.7	24.8	21.3	Side of funnel
K18	120.4	118.6	126.2	123.7	121.2	124.2	125.3	129.8	115.4	MPDE outlet
T_{air}	14.5	14.2	14.6	13.6	15.8	14.9	16.6	15.8	13.6	Air temperature
T_{sea}	15.3	15.4	15.9	15.9	16.0	15.9	16.4	16.4	16.7	Sea temperature

Table 4.31 Measured temperatures for the port side of CFAV Quest for the night runs. Measured air and sea temperatures are also included for convenience.

ShipIR (°C)									Description
11	12	15	16	20	21	26	27	34	Run number
11.6	11.2	13.4	12.1	14.6	12.8	15.6	14.8	10.4	Wall deckhouse
17.2	16.8	16.1	15.6	18.3	17.3	18.1	17.7	16.7	Funnel rail
18.8	18.5	17.9	17.3	19.8	20.3	20.2	19.7	18.2	Side of funnel
117.9	117.8	109.6	117.4	118.6	116.5	114.9	117.2	117.6	MPDE outlet

Table 4.32 Temperatures computed by ShipIR for the starboard side of the ship for night runs using Shore meteorological data.

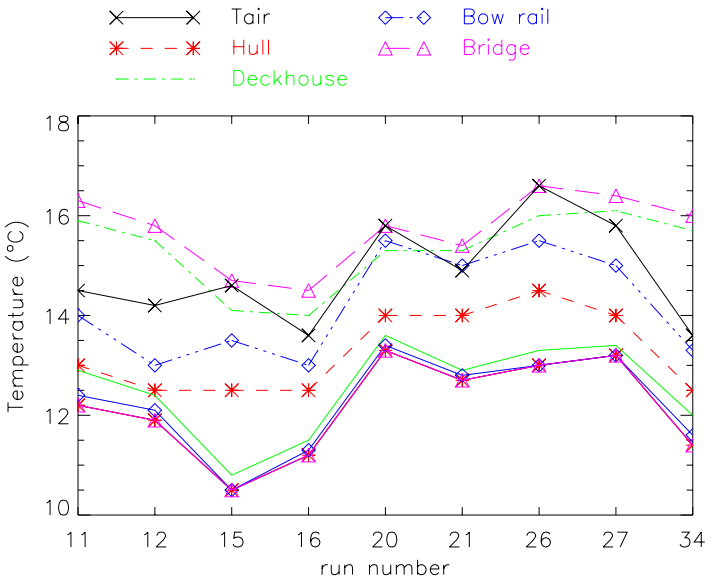

Figure 4.22 *Calculated and measured temperatures for some the port side of the ship for the night runs. The ShipIR temperatures are shown using solid lines, while the line styles of the measured temperatures change.*

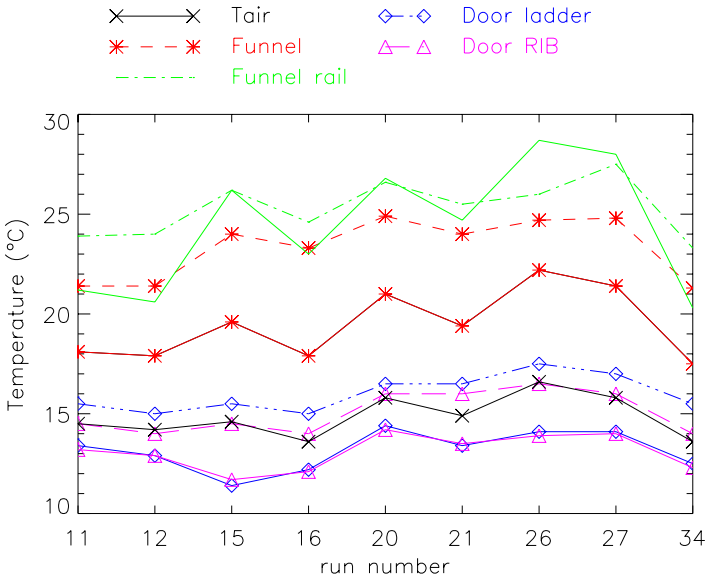

Figure 4.23 *Calculated and measured temperatures for the port side of the ship. This figure contains the warmer areas. The ShipIR temperatures are shown using solid lines, while the line styles of the measured temperatures change.*

Sensor	ShipIR ($°C$)									Description
	11	12	15	16	20	21	26	27	34	Run number
T20	16.4	15.6	14.7	14.3	16.0	15.6	16.5	16.3	16.0	Wall deckhouse
T15	20.3	20.1	17.6	17.0	18.6	18.5	19.1	19.9	19.8	Funnel rail
T4/T5	22.3	21.6	22.8	22.3	23.3	22.9	23.6	23.9	21.4	Side of funnel
K21	127.2	122.8	127.0	128.1	122.8	129.8	127.1	127.6	119.2	MPDE outlet
T_{air}	14.5	14.2	14.6	13.6	15.8	14.9	16.6	15.8	13.6	Air temperature
T_{sea}	15.3	15.4	15.9	15.9	16.0	15.9	16.4	16.4	16.7	Sea temperature

Table 4.33 Measured temperatures for the starboard side of the ship for the night runs. Measured air and sea temperatures are also included for convenience.

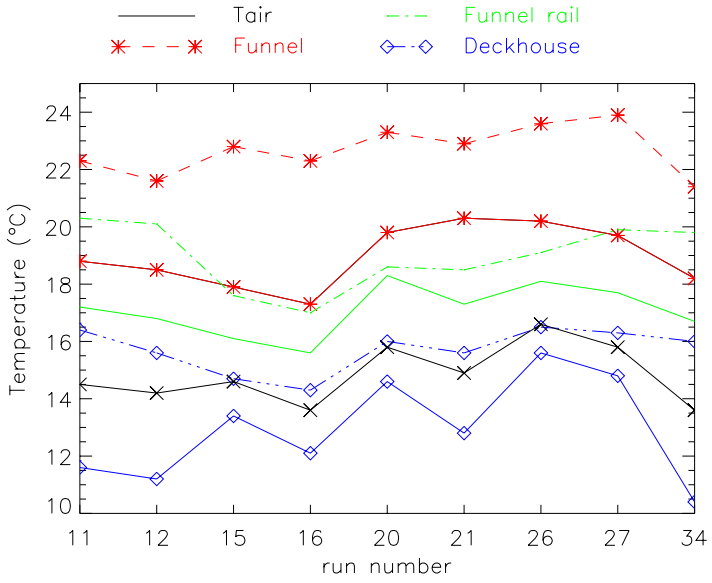

Figure 4.24 Calculated and measured temperatures for the starboard side of the ship. The ShipIR temperatures are shown using solid lines, while the line styles of the measured temperatures change.

typically several degrees lower than the air temperature, while the measurements show temperatures higher than the air temperature. This trend agrees with the low contrast computed in the MW band for the night runs. Not surprisingly, the choice of meteorological data is important for the night runs since the air and sea temperatures are essentially the only sources to heat the ship plates. Slightly better results are obtained when using the Ship temperatures.

The situation is not so clear for the day runs. The door near the RIB shows unreasonably large day-time discrepancies. This may not be the best example, though, due to poorly defined optical properties of the doors (13). The best agreement is found for the shaded side of the ship (run 31).

4.3 Discussion

As explained in section 3.2, the LW camera used during the measurements is not performing predictably during day time (large drift), and therefore all LW band day-time results must be regarded with caution. Due to the lack of an accurate relative response for the LW camera, even the LW night-time results cannot be expected to be very accurate, see chapter 3.4. Therefore, the agreement or lack of agreement between measurements and simulations in the LW band will not be further discussed.

For the MW day runs result, only one A-type run and one B-type run have been studied. This is due to lack of good image data or due to sub-optimal weather conditions (clouds).

Both the B-type day run (run 8, less than 30 % difference between measurement and modeling), and the A-type day run (run 31, 21 % lower than the measurement) show quite good agreement for the apparent radiant intensity contrast. Due to the low number of runs, it is not easy to conclude from these results.

Four C runs have been studied. The C runs have a predicted contrast about 50 % higher than the measured contrast except for run 10 where the predictions are about 20 % higher than the measurements. Solar irradiation is rapidly decreasing during the C runs, and this raises a question of whether the ship is in sufficient thermal equilibrium and a question about what meteorological parameters to use for the simulations. We have chosen to use an average value of the last 15 minutes before the measurement was performed for the solar irradiation.

The shaded-side day run temperature comparison shows very good agreement, while the sun-lit B run temperature comparison shows more mixed results with no clear trend towards higher or lower temperatures seen.

For the C runs, the predicted plate temperatures are consistently higher than the measured temperatures, with an exception for the outlet which is only slightly warmer than the predictions.

For the MW band night-time D runs studied, the starboard aspect typically shows higher contrast than the port aspect. This is in accordance with the measurements. It is found that this may be due to a prevailing westerly wind. The difference in contrast predicted by ShipIR for the night runs for the port and starboard side of the ship can be attributed to a net wind warming. Turning off the wind in the simulations results in very similar contrasts and

surface temperatures for the two sides of the ship. There are also some differences between the two ship sides which may results in slightly higher contrast on the starboard side as discussed in chapter 3.3. However, the starboard side of the ship may not be in thermal equilibrium at the time of measurement since the ship turns shortly before the measurement is taken. The relative port side–starboard side agreement between measurements and simulations may therefore be fortuitous. In almost all the night runs, the computed contrast (for both aspects) is significantly lower than the measured contrast. This seems to correspond with predicted plate temperatures being too low. The only exception is for two runs with clouds. Also, apart from the two cloudy runs (runs 11 and 12), the trend in the contrast from run to run seems to be quite similar for the measurements and the simulations.

The contrast difference from run to run depends on several factors such as changes in meteorological data with associated changes in background and target temperatures and transmissivity. Changes in aspect angles and distances from run to run complicate the picture further. Therefore, no attempt has been made to investigate the difference in contrast between different runs.

The predicted plate temperatures for the night runs are consistently lower than the measured temperatures for the 'Shore' scenarios. Using the higher air temperature measured by the ship seems to improve the plate temperature agreement somewhat, but to a much lesser extent improves the contrast agreement.

Possibly, the low contrast predicted for the night runs is due to a problem with the temperatures computed by ShipIR, or due to a problem with the input meteorological data. The sensitivity to different input meteorological data has to some extent been investigated through the use of several different scenarios for runs 21 and 34. The discrepancy between measurements and simulations is clearly larger than the differences in results obtained through the use of these scenarios. There is also a much wider spread in the measured temperatures for the hull and superstructure parts of the ship than given by the ShipIR results. This cannot simply be explained by the use of too low input temperatures.

Another possible explanation for the findings is an incomplete target model. If the ship is not so perfectly insulating as assumed, this may explain too high C run temperature predictions and too low D run temperature predictions.

5 CONCLUSIONS

The SIMVEX trial was a joint NATO trial arranged by the NATO RTO/SET/TG16 group. The trial was very well planned, and was carried out according to the plan. Previous trials and the expertise from different group members made this possible. The trial was held at Osborne Head, near Halifax, Nova Scotia, Canada. The NESTRA range proved to be a very good place to perform the measurements, with facilities to accomplish communication between participating countries (both voice and data), locations for all the measurement teams, storage rooms for equipment, all this in a guarded facility. Canada also provided the test ship CFAV Quest, which was instrumented with different sensors. The ship had no other objectives during the trial, and did exactly as we wanted. An extensive ShipIR target file was made of the ship, which is essential for model validation. All these factors made

this a very successful trial.

The quality of the measurements performed by FFI varies to some degree. The spectral measurements made with the Bomem DA5 spectroradiometer seems to be of a very high quality, these results will be presented in a separate report (7). The IR imagery is not of the desired quality. This is mainly due to the fact that the infrared MW camera we planned to use, broke down before the trial and was not returned from repair in time. The uncertainty for the MilCam camera is somewhat higher than wanted (see section 3.4). The LW camera in use, an Amber Sentinel camera, did not perform very well, and at the present time this camera is not very well characterized. The results from the measurements with the Sentinel LW camera should thus not be used for validation, however some results from this camera are included in the report. The meteorological data collected by FFI during the trial are believed to be of high quality. It is difficult to make good meteorological recordings. The wind sensor was placed at a much higher position than the other sensors to make sure that the sensor was not influenced by near-by buildings. Unfortunately one of our weather stations was hit by a log from the sea, and suffered severe damage.

This trial has shown that it is very important that all the equipment to be used is well characterized. This is of course important for all the equipment, but especially important for the infrared cameras in use. Knowledge of the cameras makes it possible to perform an error analysis, and thus valuable information for the model validation process.

When modeling of the atmosphere is involved it is very important to have the best possible meteorological data. In addition, it is important to have registration of meteorological data in several places. In this trial, FFI had one meteorological station at the shore site, and one was placed near the shoreline. On board the ship DRDCV mounted one meteorological station, these stations indicate local variations that play a certain role in the simulations. Local variations happen even though the distance between the shore site and the ship is only 1000 meter when the measurement is performed. Some of these effects are due to variation between land and sea. In the modeling of the atmosphere near the sea surface, an aerosol model called Navy Maritime (NAM) is used. One of the inputs to this model is an “air-mass” parameter, this is a parameter showing the influence of land generated aerosols at the sea. This is one of the parameters that is difficult to evaluate.

ShipIR calculations have been performed for several SIMVEX runs. Determined by the available imagery and the weather conditions, the effort has concentrated on the day-time C runs and night-time D runs. ShipIR clearly overpredicts both apparent radiant intensity contrast and temperatures for the day-time C runs, while there is a clear underprediction for the night-time D-runs. There are several possible explanations for this. First, the target model may be incomplete. The ship is assumed to be perfectly insulated which may not be completely true. Second, the input meteorological data may not be completely representing the equilibrium situation on the ship. As pointed out in section 4.3, the solar irradiation is changing rapidly during the C-runs due to the setting of the sun. This introduces some uncertainty about the equilibrium assumption in ShipIR. When several measurement stations are available as in this trial, it is hard to figure out which data set to use. Also, there may be errors in the meteorological measurements influencing the results. Third, there may be errors in ShipIR. An investigation of the background predictions will be performed using the measured spectral data, and the results will be presented in another report (7).

5.1 Future work

FFI is analyzing the spectral data obtained with the Bomem DA5 FTIR spectroradiometer during the SIMVEX trial. These data will be used to analyze the plume, certain parts of the ship, and the sea and sky background. These data could be used to verify such parts of the ShipIR model.

Future work will consist of new validations of ShipIR, this includes simulations with new versions of ShipIR and performing new measurements. A new measurement should be of a “war ship” with gas turbine engines. Such a measurement could be performed during the NATO SWG/4 EW trial in 2003. FFI plans to participate in this trial with new infrared cameras. If there is a good target file available for one (or more) of the participating ships such a validation could be performed.

Measurement of the new Norwegian frigate, Fridtjof Nansen class, when the ship is delivered is of great interest.

REFERENCES

(1) Stark E, Brendhagen E, Lippert E, Bingen E (2000): (U) Spectral ir signatures of ships and decoys measured by FFI during NATO SWG/4 EW Trial 1999, FFI/RAPPORT-2000/02789, Forsvarets forskningsinstitutt (Confidential).

(2) Mermelstein M D, Snail K A, Priest R G (2000): Spectral and radiometric calibration of midwave and longwave infrared cameras, *Optical Engeneering* **39**, 2, 347–352.

(3) Anderson G P (1996): The Modtran 2/3 Report and LOWTRAN 7 Model, F19628-91-C-0132, Air Force Research Laboratory, USA.

(4) Fraedrich D (2001): Image analysis for SIMVEX, presented at NATO RTO/SET/TG16 meeting spring 2001.

(5) Vaitekunas D (2001): DAVIS instrumentation plan for the SIMVEX trial, A117-001, Rev 1, W.R. Davis Engineering Limited, Ottawa, Ontario (Canada).

(6) Stark E, Steenfeldt-Foss P, Brendhagen E, Almklov B (2001): SIMVEX 2001 Trial - FFI test plan for infrared measurements, FFI/NOTAT-2001/04023, Forsvarets forskningsinstitutt.

(7) Brendhagen E, Heen L T (2002): SIMVEX 2001 Trial - Spectral IR measurements (under preparation), FFI/RAPPORT-2002/xxxxx, Forsvarets forskningsinstitutt.

(8) Cini A (2001): Nato trials, italian contribution, presented at NATO RTO/SET/TG16 meeting fall 2001.

(9) Holst G C (2000): Common sense approach to thermal imaging, SPIE Optical Engineering Press.

(10) Fraedrich D (2001), Calibration error, Private email communication.

(11) Coleman H W, Glenn Steele Jr W (1989): Experimentation and uncertainty analysis for engineers, John Wiley & Sons.

(12) Vaitekunas D (2002): Technical Manual for ShipIR/NTCS (V2.9), W.R. Davis Engineering Limited, Ottawa, Ontario (Canada).

(13) Miller C (2002), Ir properties of doors, Private email communication.

(14) Pollock D H, (Eds) (1993): The Infrared & Electro-Optical Systems Handbook, Countermeasure Systems, Volume 7, Infrared Information Analysis Center.

APPENDIX

A EQUIVALENT BLACKBODY TEMPERATURE

In section 2.1 the equivalent blackbody temperature is found by solving equation (2.10) numerically:

$$\int_0^\infty N_{bb}(\lambda, T_{eq})\,\tau_{atm}(\lambda, x_t)\,r_s(\lambda)\,d\lambda = \frac{S_{tgt} - S_0}{K} - \int_0^\infty N_{atm}(\lambda, x_t)\,r_s(\lambda)\,d\lambda \tag{A.1}$$

Equation (A.1) may also be written as:

$$\int_0^\infty \left\{N_{bb}(\lambda, T_{eq}) - N_{bb}(\lambda, T_{atm})\right\}\,\tau_{atm}(\lambda, x_t)\,r_s(\lambda)\,d\lambda = \frac{S_{tgt} - S_0}{K} - \int_0^\infty N_{bb}(\lambda, T_{atm})\,r_s(\lambda)\,d\lambda \tag{A.2}$$

If the blackbody temperature is close to the atmospheric temperature ($T_{eq} \approx T_{atm}$) equation (A.2) can be written as:

$$\left(T_{eq} - T_{atm}\right) \int_0^\infty \left(\frac{\partial N_{bb}(\lambda, T)}{\partial T}\right)_{T_{atm}} \tau_{atm}(\lambda, x_t)\,r_s(\lambda)\,d\lambda \approx \frac{S_{tgt} - S_0}{K} - \int_0^\infty N_{bb}(\lambda, T_{atm})\,r_s(\lambda)\,d\lambda \tag{A.3}$$

The equivalent blackbody temperature, T_{eq}, can now be found:

$$T_{eq} \approx T_{atm} + \frac{\frac{S_{tgt}-S_0}{K} - \int_0^\infty N_{bb}(\lambda, T_{atm})\,r_s(\lambda)\,d\lambda}{\int_0^\infty \left(\frac{\partial N_{bb}(\lambda,T)}{\partial T}\right)_{T_{atm}} \tau_{atm}(\lambda, x_t)\,r_s(\lambda)\,d\lambda} \tag{A.4}$$

This method is useful if the the necessary computing power to solve equation 2.10 is not present.

B RUN LIST

SIMVEX RUN	FFI RUN	Type	Date	Time (Z)	Day/Night	Cloud Cover
1	36, 37	Panel	11		Day	?
2	43, 46	Panel	11		Day	?
3	52	Panel	12		Day	?
4	58, 61	Panel	12		Day	?
5	85	C	13	21:02:47	Day	Broken
6	90	C	13	22:21:06	Day	Broken
7	93 94	D	13	23:27:02	Night	Broken
8	99	B	14	16:56:12	Day	Few
9	104	A	14	18:32:26	Day	Few
10	110	C	14	21:00:00	Day	Scattered
11	116 118	D	14	23:30:43 23:38:15	Night	Broken
12	122 123	D	15	00:18:03 00:25:27	Night	Broken
13	128	A	15	18:33:19	Day	Few
14	134	C	15	21:08:35	Day	Few
15	140 141	D	15	23:28:42 23:36:39	Night	Few
16	146 147	D	16	00:16:08 00:24:17	Night	Few
17	152	B	16	17:04:30	Day	Few
18	169	A	16	18:37:38	Day	Few
19	175	C	16	21:06:04	Day	Clear
20	182 183	D	16	23:27:06 23:35:28	Night	Few
21	189 190	D	17	00:14:55 00:22:28	Night	Few
22	196	B	17	17:07:35	Day	Broken
23	203 – 212	Shore plume	17	17:55 – 19:23	Day	Broken
24	219	C	17	21:06:33	Day	Broken
25	225 226	Shore plume	17	21:45:02 21:53:35	Day	Broken

SIMVEX RUN	FFI RUN	Type	Date	Time (Z)	Day/Night	Cloud Cover
26	237 238	D	17	23:25:54 23:38:01	Night	Broken
27	245 246	D	18	00:18:23 00:26:35	Night	Broken
28		Off-shore plume	18	13:00 – 14:20	Day	Broken
29	254	B	18	17:05:52	Day	Broken/ overcast
30		Off-shore plume	19	15:47 – 16:28	Day	Clear
31	259	A	19	18:34:15	Day	Clear
32	265	C	19	20:51:19	Day	Clear
33		DRDCV panel	19	21:02 – 21:34	Day	Clear
34	293 294	D	19	23:31:24 23:39:15	Night	Clear
35	301 302	D	20	00:24:26 00:32:13	Night	Clear
36	309	B	20	17:05:39	Day	Broken
37	315	Shore plume	20	21:03:56	Day	Broken
38	321	C	20	21:03:56	Day	Broken/ overcast
39	328 329	D	20	23:30:08 23:38:37	Night	Broken/ overcast
40	336 337	D	21	00:25:45 00:33:57	Night	Broken

C METEOROLOGY

Norway was responsible for measuring and logging meteorological data at Osborne Head during the SIMVEX trials. In this appendix a summary on sensors, technical specifications, sensor placement, and comments to equipment and measurements are given.

All meteorological data are available as digital data. In figures C.3 – C.6 some plots of meteorological data from the NESTRA station for the entire trial are given.

C.1 Instrumentation

Norway had two weather stations; a main station placed at NESTRA (NESTRA Station), and a secondary station placed (below) close to the waterline (Waterline Station). In addition there was a sensor for measuring the sea temperature. Register interval for both stations was one minute. The waterline station was destroyed at midnight between September 18 and 19.

C.1.1 NESTRA Weather Station

The NESTRA weather station consisted of sensors from various manufacturers. The sensors (except the anemometer) were placed inside and on top of the Norwegian instrumentation container. The anemometer was placed on top of a nearby tower, see figures C.1 and C.2. Sensor specifications for the NESTRA weather station are given in table C.1.

Data	Manufacturer	Model	Resolution	Accuracy
Air temperature[1]	Vaisala	HMP35D		$0.3°C$
Relative humidity[1]	Vaisala	HMP35D		0–90% RH: 2% 90–100% RH: 3%
Air temperature[2]	Vaisala	HMP45D		$0.3°C$
Relative humidity[2]	Vaisala	HMP45D		0–90% RH: 2% 90–100% RH: 3%
Barometric pressure	Vaisala	PTB220A	0.1 hPa	0.3 hPa
Wind velocity	Gill	2-axis Ultrasonic	0.01 m/s	5%
Wind direction	Gill	2-axis Ultrasonic	1°	4°
Rainfall intensity	Aanderaa	3064	0.02 mm	0.02 mm
Solar radiation	Kipp & Zonen	SP Lite		Spectral: 5% Cosine: 10%
Sea temperature	Scand Inst.	SIN 642		$0.1°C$ (0–15 $°C$)
Data logger	HP (Agilent)	HP34970A	Better than sensors	

Table C.1 Specifications for sensors on FFI NESTRA Weather Station.

Comments on the measurements at the NESTRA weather station:

[1] Sensor mounted inside a “conventional” multi-plate radiation shield.

[2] Sensor mounted inside a radiation shield with forced ventilation (Qualimetrics Model 8190).

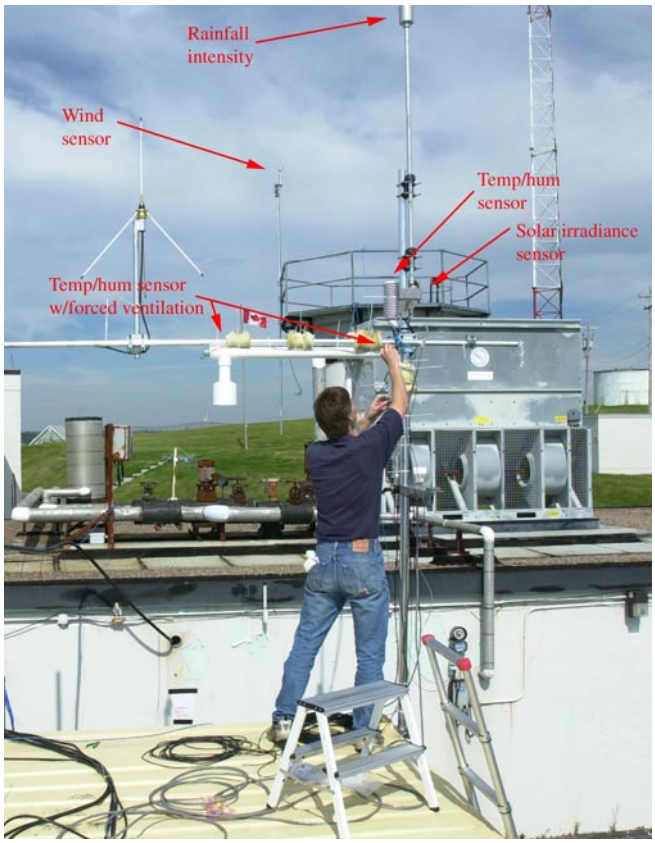

Figure C.1 Meteorological sensors mounted on top of container. Wind sensor is mounted on tower further away from the container.

Figure C.2 Sensor for wind speed and direction measurements. This is an ultra-sonic wind sensor without any moving parts.

Humidity: Some mornings long ”recovery time” due to heavy condensation during the night.

Temperature: The forced ventilated radiation shield was used to minimize errors under conditions with high solar irradiation and low wind speed. Reasonable results obtained after moving the air intake for the radiation shield away from the container roof. This movement took place on September 13, approximately 1445 UTC. Accurate temperature measurements can be difficult.

Wind: The recorded wind data are 5 seconds average.

Placement of sensors: All heights are referred to mean sea level (msl). Container placement was 23.5 meter above msl. The heights of the different sensors are given in table C.2.

Sensor	Placement (above msl)
Air temperature	27.9 m
Rel humidity	27.9 m
Air temperature (with fan)	27.9 m
Rel humidity (with fan)	27.9 m
Barometric pressure	23.7 m
Wind velocity	33.6 m
Wind direction	33.6 m
Rainfall intensity	30.1 m
Solar irradiation	29.1 m
Sea temperature	70 m (from shore line) at 20 cm depth

Table C.2 Placement of sensors at the NESTRA weather station.

The data from the sea temperature sensor was logged on the waterline station until the breakdown of the station. The signal cable was then extended and logging continued on the NESTRA station.

C.1.2 Waterline Weather Station

In an attempt to get meteorological data close to the sea surface, a weather station was placed close to waterline at the SW end of the breakwater dam below NESTRA. This was a compact station, model MWS 9, Reinhardt GmbH, Germany, containing seven sensors and internal data logger. A picture of the station is presented in figure C.7. Sensor specifications are given in table C.3. At midnight, between September 18 and 19, this station was destroyed by the combination of a log in the water and the remains of a hurricane.

Humidity: Reduced accuracy for values above 90% RH.

Wind: Inaccurate values due to the steep slope behind the weather station.

The waterline station was placed about 3 meters above mean sea level.

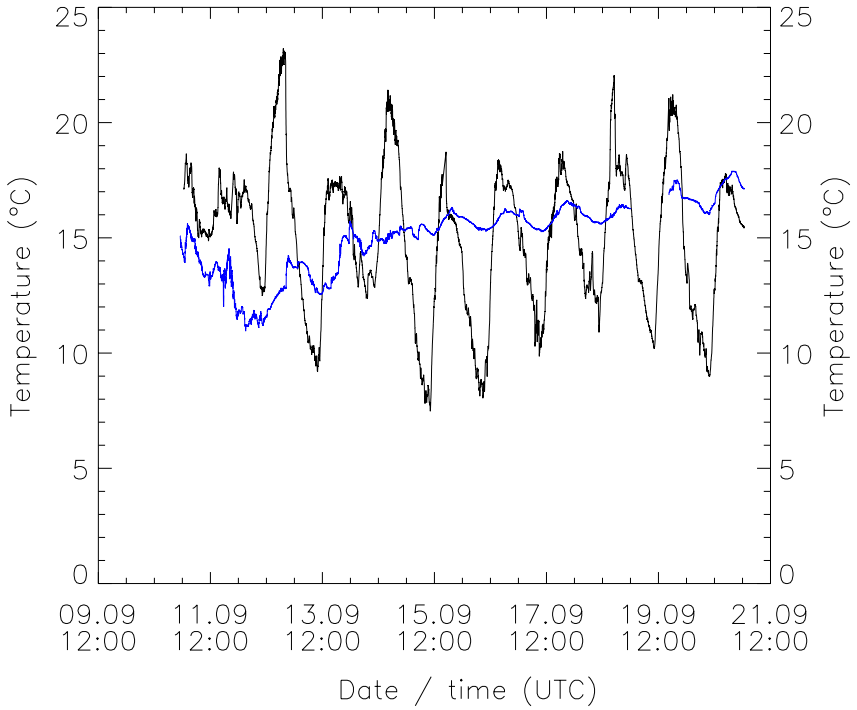

Figure C.3 Air (black line) and sea (blue line) temperature.

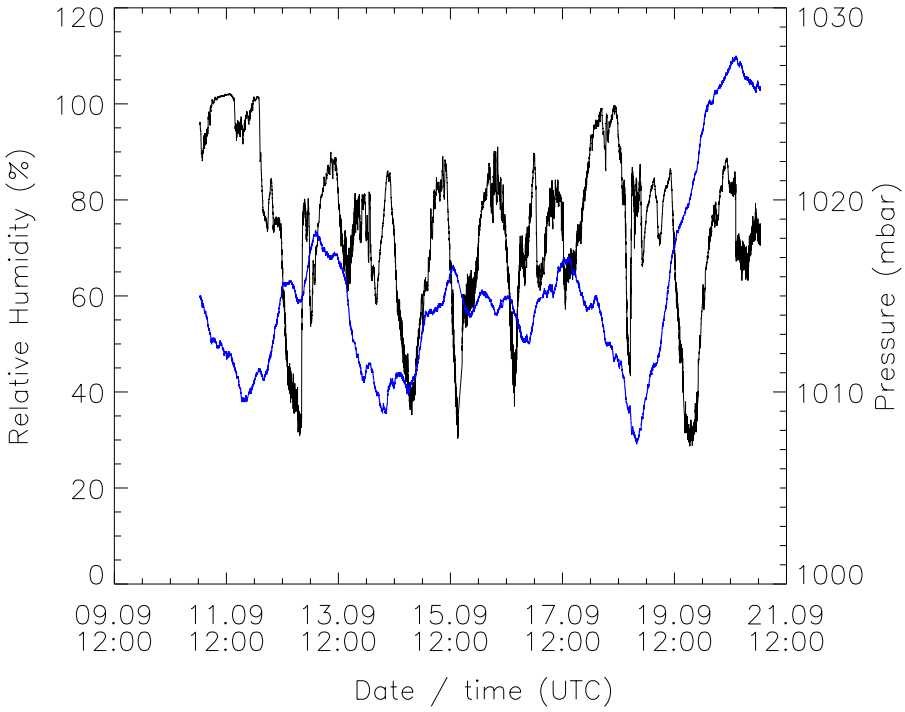

Figure C.4 Relative humidity (black line) and pressure (blue line).

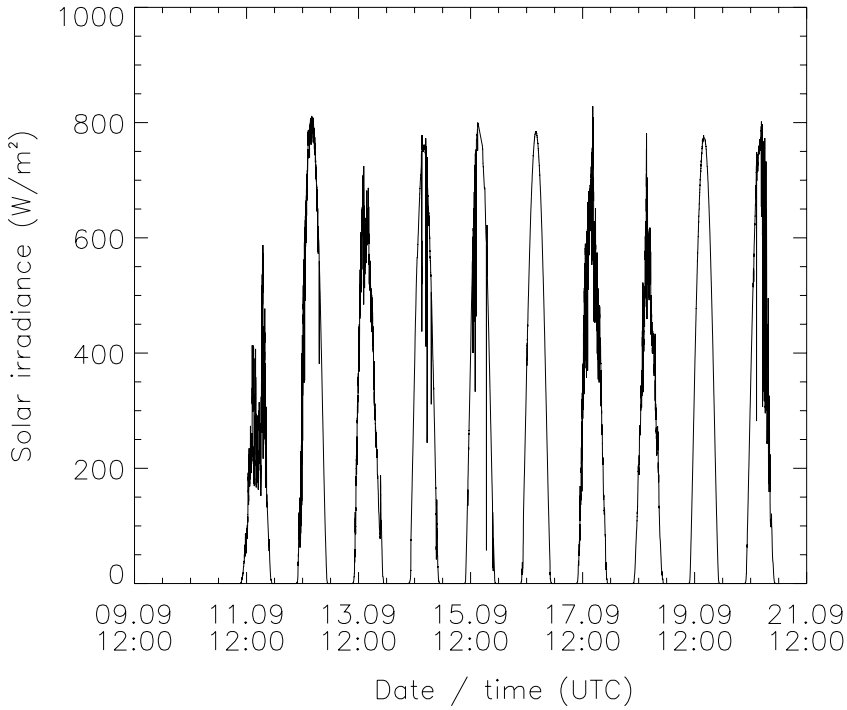

Figure C.5 Solar irradiance.

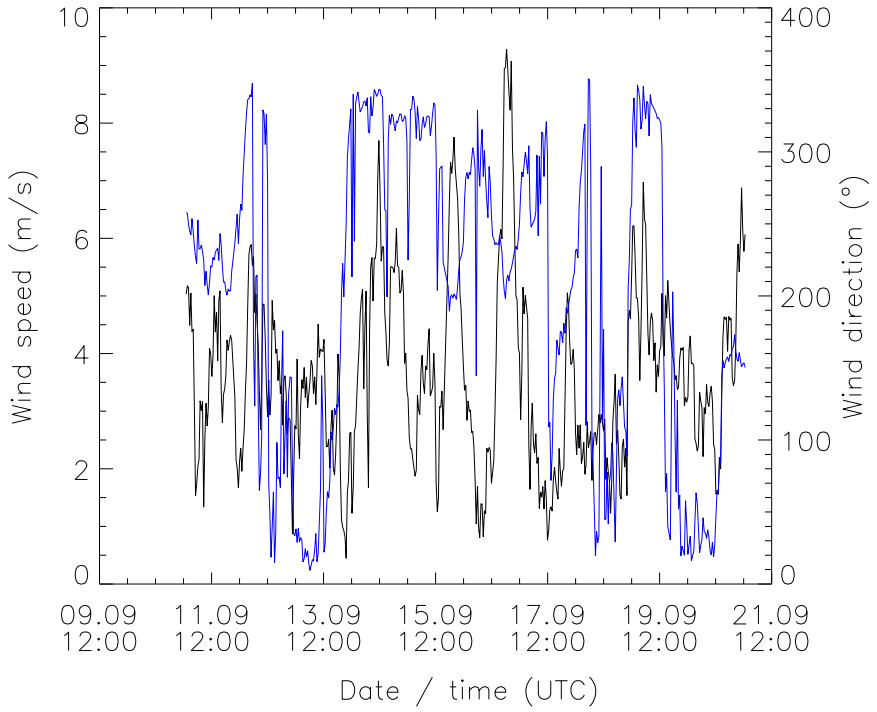

Figure C.6 Wind speed (black line) and direction (blue line) (30 min average).

Figure C.7 Reinhardt meteorology station near the waterline.

Data	Resolution	Accuracy
Air temperature	$0.1°C$	$0.3°C$
Relative humidity	0.1%	2%
Barometric pressure		0.8 hPa
Wind velocity, response above 0.5 m/s	0.03 m/s	0.5 m/s
Wind direction, blind region 350–359°	0.1°	2.5°
Rainfall intensity	0.1 mm	0.2 mm
Solar irradiation	$1W/m^2$	$40W/m^2$

Table C.3 Specifications for sensors on Reinhardt MWS 9 meteorological station placed near waterline.

C.2 Manual observations and meteorological data

During the trial some manual observations of the cloud cover were made. These observations are presented in table C.4. For most of the manual observation visible photographs of the sky exists. An example is shown in figure C.8.

Date	Time (UTC)	Cloud cover	Comments
12	15:00	1/8	
12	18:00	1/8	
13	18:00	7/8	Clear sky towards north
13	22:30	4/8	Light clouds, scattered
14	17:30	$< 1/8$	
14	20:15	$\ll 1/8$	
14	21:15	$< 1/8$	
14	22:45	6/8	Scattered
15	17:45	$< 1/8$	Scattered
15	20:20	$\ll 1/8$	Scattered
15	22:40	$< 1/8$	Scattered
16	18:10	$< 1/8$	Scattered clouds towards east
16	20:25	0/8	Almost clear sky
16	22:45	$< 1/8$	A few clouds towards west and south-west
17	16:30	6/8	Partly light cloud cover
17	20:00	4/8	Light cloud cover
17	22:40	7/8	Light cloud cover, scattered areas with clear sky
18	16:30	$> 7/8$	Light cloud cover
19	18:00	0/8	Clear sky except a few clouds SE horizon
19	20:10	0/8	
19	22:00	0/8	
20	16:40	2/8	Scattered
20	17:15	6/8	Scattered areas with clear sky
20	19:05	6/8	Scattered areas with clear sky variable thickness and height of clouds
20	20:35	7/8	Scattered areas with clear sky variable thickness and height of clouds
20	21:20	$> 7/8$	Variable thickness and height

Table C.4 Manual cloud cover observations during the trial.

The meteorological data used in the ShipIR/NTCS simulations in chapter 4 are presented in tables C.5 – C.8. The numbers in parentheses in table C.6 are 15 minute averages.

Figure C.8 Visible images of cloud cover, 14.09.2002, 17:20 (UTC), run 8.

Parameter	Data
Air temperature	$20.5°C$
Relative humidity	29.5%
Wind speed	$3.7\,m/s$
Wind direction	7°
Wind speed (24 hrs average)	$3.7\,m/s$
Pressure	$1020.1\,mBar$
Sea temperature	$17.3°C$
Solar irradiance	$603.8\,W/m^2$
Aerosol model	NAM
AMP	6

Table C.5 Meteorological data for type A run 31, 19.09.2001, 18:34 (UTC).

Run	10	14	19	32
Date	14	15	16	19
Time (UTC)	20:57:46	21:06:27	21:04:21	20:49:59
T_{air} $(°C)$	18.4	15.6	17.1	19.3
RH $(\%)$	41.8	58.5	68.0	34.3
Wind speed (m/s)	4.0 (5.1)	7.0 (6.6)	8.6 (7.4)	3.6 (4.4)
Wind dir. $(°)$	319 (329)	206 (205)	227 (224)	25 (25)
Wind 24hrs (m/s)	4.4	3.9	4.1	4.5
Pressure $(mBar)$	1010.9	1014.1	1012.6	1021.3
T_{sea} $(°C)$	15.1	16.0	16.1	17.3
I_{sun} (W/m^2)	192.8 (215.2)	190.2 (211.8)	185.9 (208.1)	222.3 (244.7)
AMP	9	2	2	4

Table C.6 Meteorological data for type C runs 10, 14, 19, and 32. The numbers in parentheses are 15 minute averages.

Run	11	12	15	16
Date	14	15	15	16
Time (UTC)	23:28:33	00:15:49	23:26:28	00:14:20
T_{air} $(°C)$	14.5	14.2	14.6	13.6
RH $(\%)$	59.0	53.2	65.1	73.3
Wind speed (m/s)	2.9	3.5	4.8	4.0
Wind dir. $(°)$	357	350	234	270
Wind 24hrs (m/s)	4.7	4.8	4.0	4.0
Pressure $(mBar)$	1012.8	1013.4	1014.6	1014.9
T_{sea} $(°C)$	15.3	15.4	15.9	15.9
I_{sun} (W/m^2)	0	0	0	0
AMP	9	8	2	5

Table C.7 Meteorological data for type D runs 11, 12, 15, and 16.

Run	20	21	26	27
Date	16	17	17	18
Time (UTC)	23:25:41	00:13	23:24:24	00:16:43
T_{air} $(°C)$	15.8	14.9	16.6	15.8
RH $(\%)$	86.1	86.6	87.4	93.1
Wind speed (m/s)	2.1	2.8	3.9	2.9
Wind dir. $(°)$	241	272	217	227
Wind 24hrs (m/s)	4.1	4.1	2.7	2.6
Pressure $(mBar)$	1013.5	1014.2	1014.3	1014.6
T_{sea} $(°C)$	16.0	15.9	16.4	16.4
I_{sun} (W/m^2)	0	0	0	0
AMP	3	3	2	2

Table C.8 Meteorological data for type D runs 20, 21, 26, and 27.

C.3 Meteorological data run 8

In this section detailed plots of the meteorological data from run 8 are presented. The dotted line in all of the figures indicates the distance from shore site to ship. The passing of the waypoint is also indicated.

In figure C.9 the different temperature measurements are presented. There is clearly a difference in temperature measurements from the shore site to the ship measurements. The meteorological data from CFAV Quest come from a meteorological station placed on board the ship by DRDCV. This plot indicates a horizontal profile for the temperature during this run. The air temperature used in the analysis (table 3.5) is based on an average between the shore-site and CFAV Quest. The sea temperature is relatively stable for such a short period of time, but shows a tendency of increasing temperature. This was the tendency for the entire period, see figure C.3.

In figure C.10 the relative humidity is presented. There is a slight difference between the ship measurements and the shore site measurements. The relative humidity used in the analysis is also based on an average between the ship and shore measurements.

Figure C.11 shows the calculated absolute humidity. The absolute humidity is calculated using the following exponential fitted curve:

$$ahum(100\%) = \chi \exp\left(18.9766 - 14.9595\chi - 2.43882\chi^2\right) \tag{C.1}$$

where $\chi = 273.15/T$, and the temperature T is given in Kelvin. The unit of the absolute humidity is g/m^3.

The solar irradiance measured is presented in figure C.12. There is some variation in the measured solar irradiance. Parts of this variation are due to the fact that it was not a totally clear sky during run 8, see figure C.8. In addition is seems that the sensor on board CFAV Quest is influenced by the surroundings, this is also shown in figure C.17.

In figure C.13 the pressure at the different meteorological stations is shown. There is also a

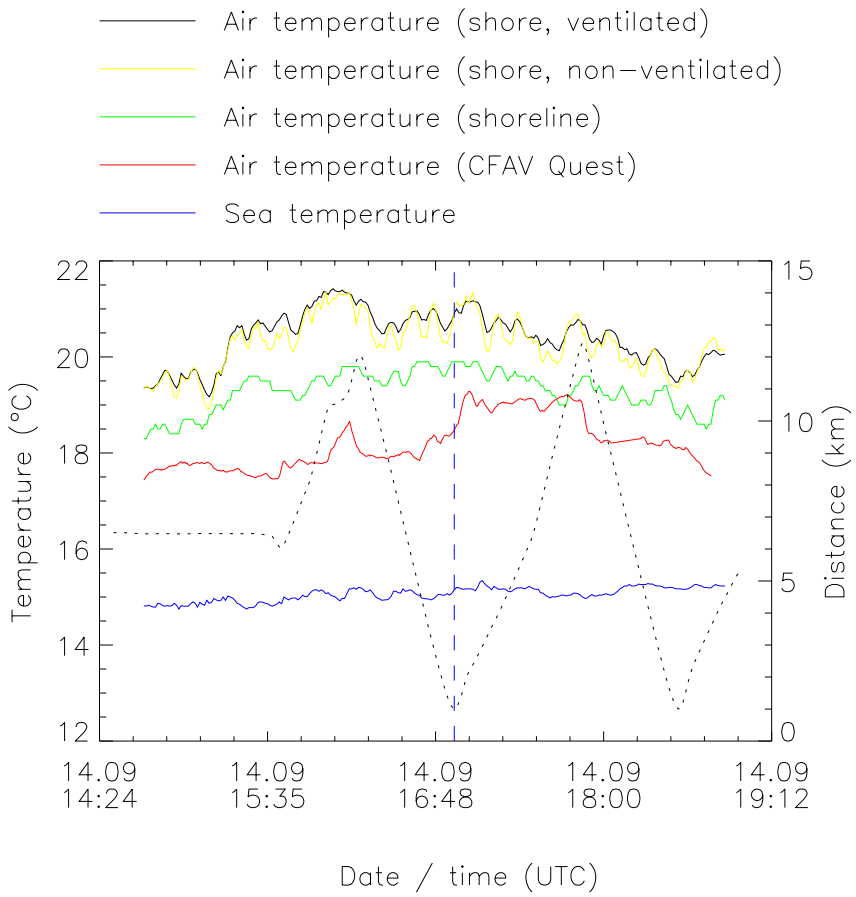

Figure C.9 Temperature measurements, run 8.

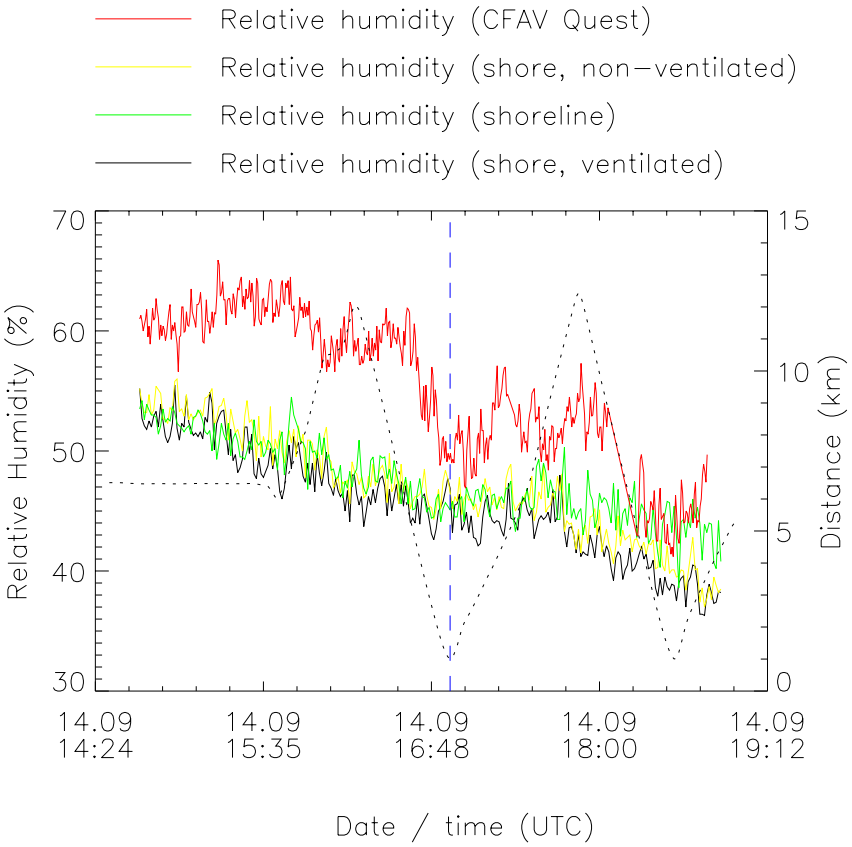

Figure C.10 Relative humidity measurements, run 8.

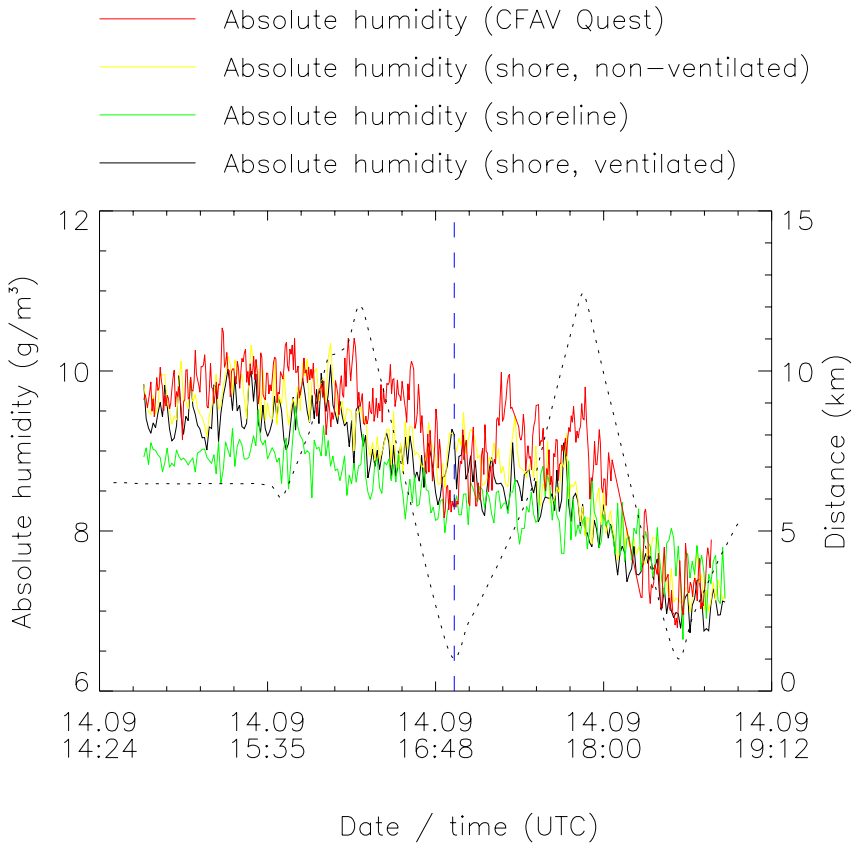

Figure C.11 Absolute humidity calculations, run 8.

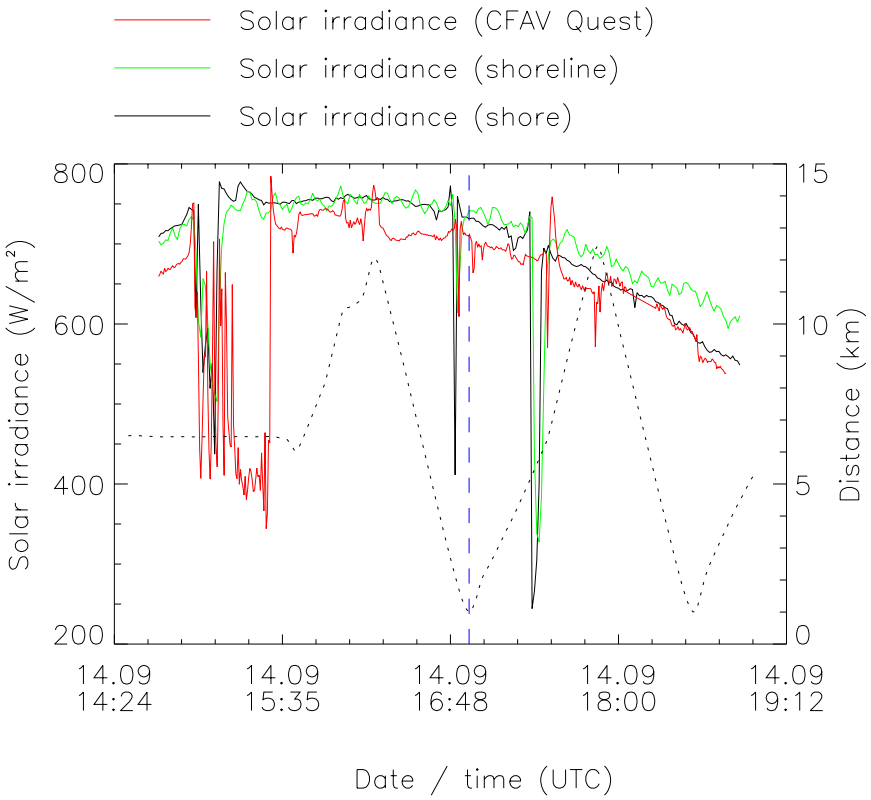

Figure C.12 Solar irradiance measurements, run 8.

calculated pressure line, where the pressure at 23.7 meter is transformed to 3 meter, using the following equation:

$$P(z) = P_1 \exp\left(\frac{-g(z - z_1)}{R\,T_1}\right) \tag{C.2}$$

where

- z - New height
- z_1 - Height for measurements
- P_1 - Pressure measured at height z_1
- T_1 - Temperature in Kelvin measured at height z_1
- R - Dry air gas constant, $R = 287\ J/kg/K$
- g - 9.81 m/s

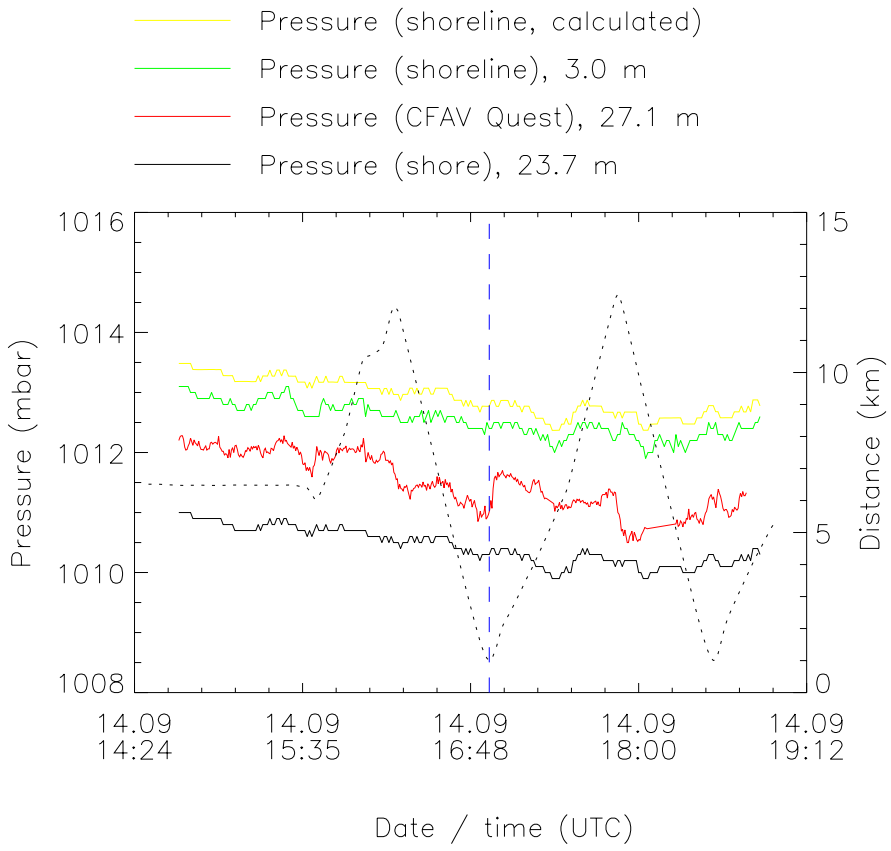

Figure C.13 Pressure measurements, run 8.

C.4 Meteorological data run 34

Figures C.14 – C.18 show the same data as the figures in section C.3. The data from the waterline station are missing due to the breakdown of the station.

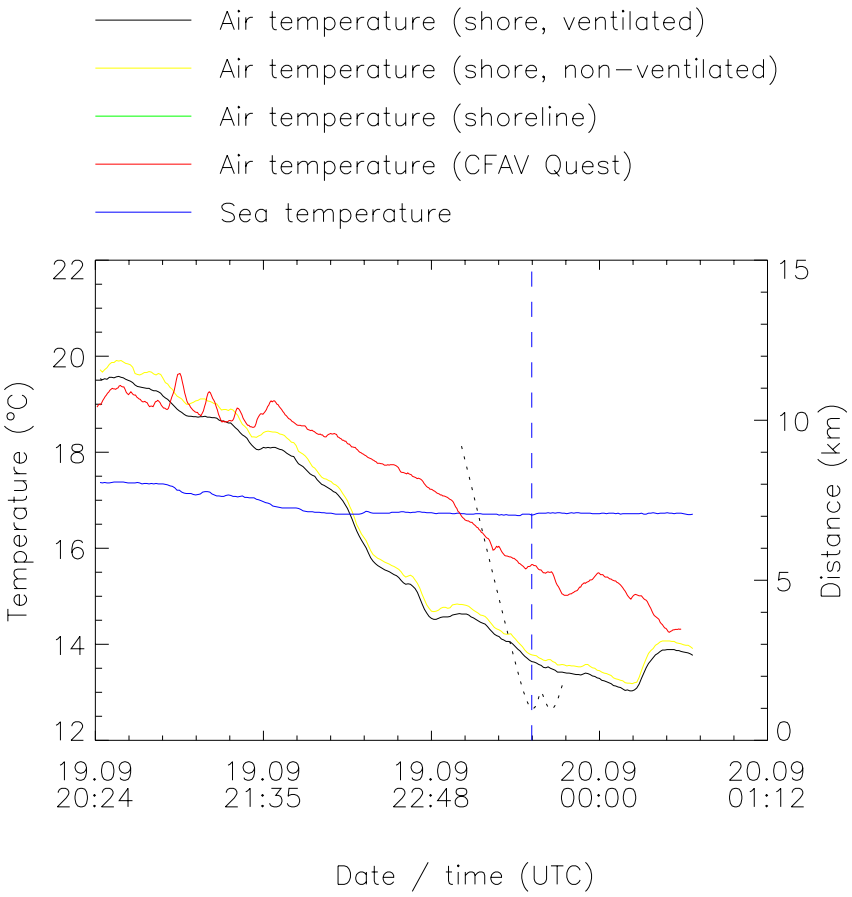

Figure C.14 Temperature measurements, run 34.

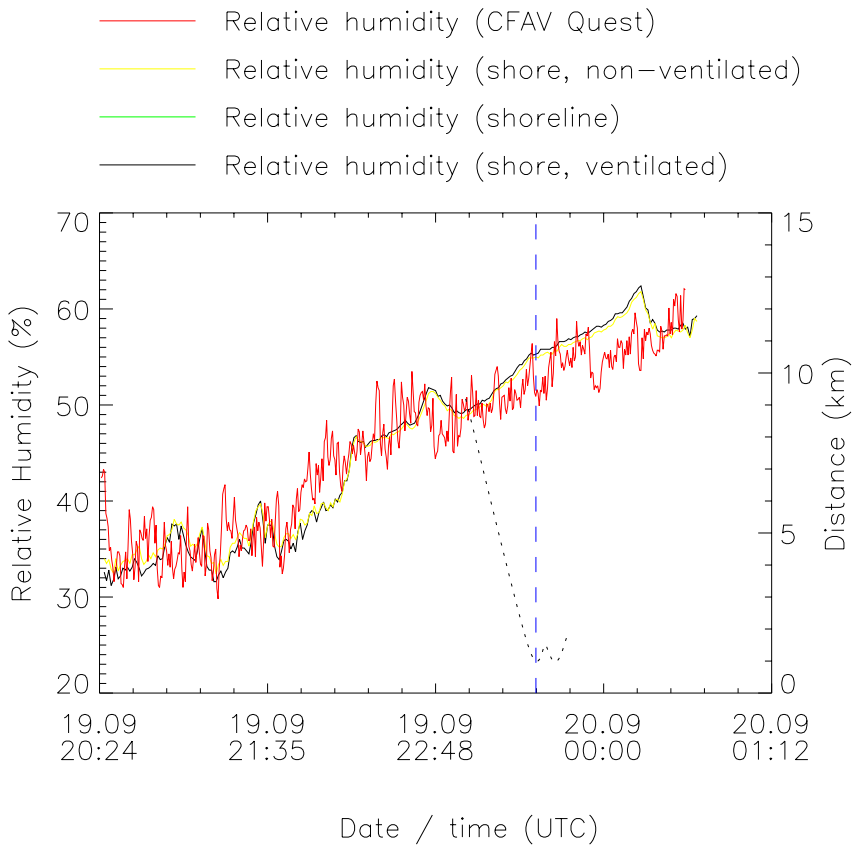

Figure C.15 Relative humidity measurements, run 34.

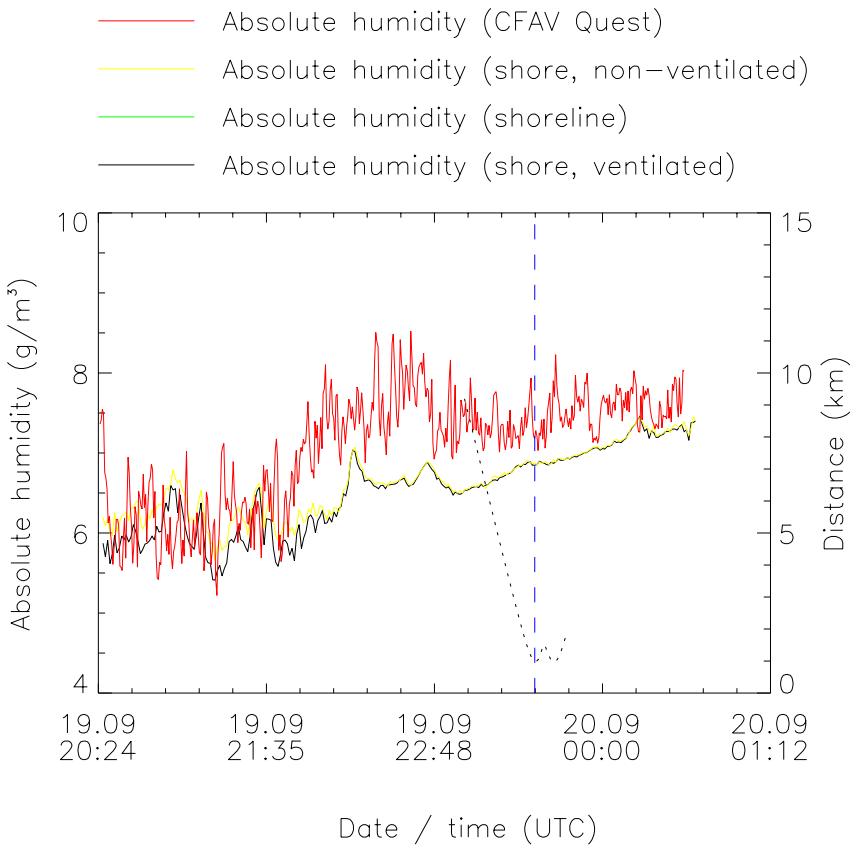

Figure C.16 Absolute humidity calculations, run 34.

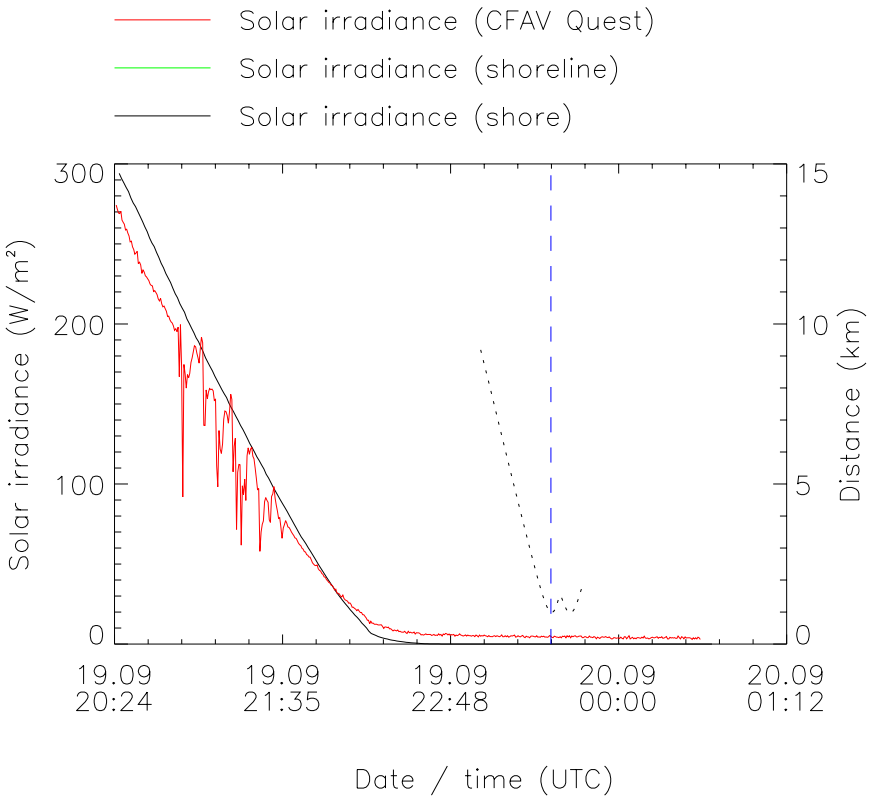

Figure C.17 Solar irradiance measurements, run 34.

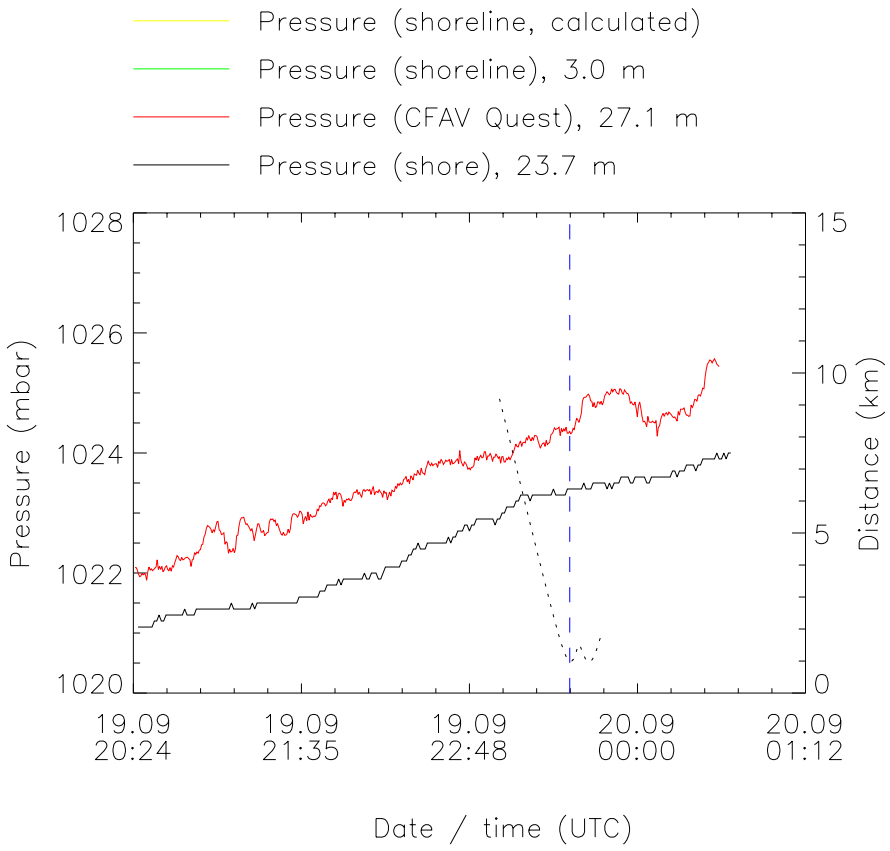

Figure C.18 Pressure measurements, run 34.

D SHIP PAINT REFLECTION MEASUREMENT

An image of the ship is presented in figure 1.1. From the image we see that the ship is painted in two colors, white and dark yellow (ocher). Paint samples of the two colors are provided on pieces of metal from Naval Research Laboratory (USA). Figure D.1 shows an image of the samples.

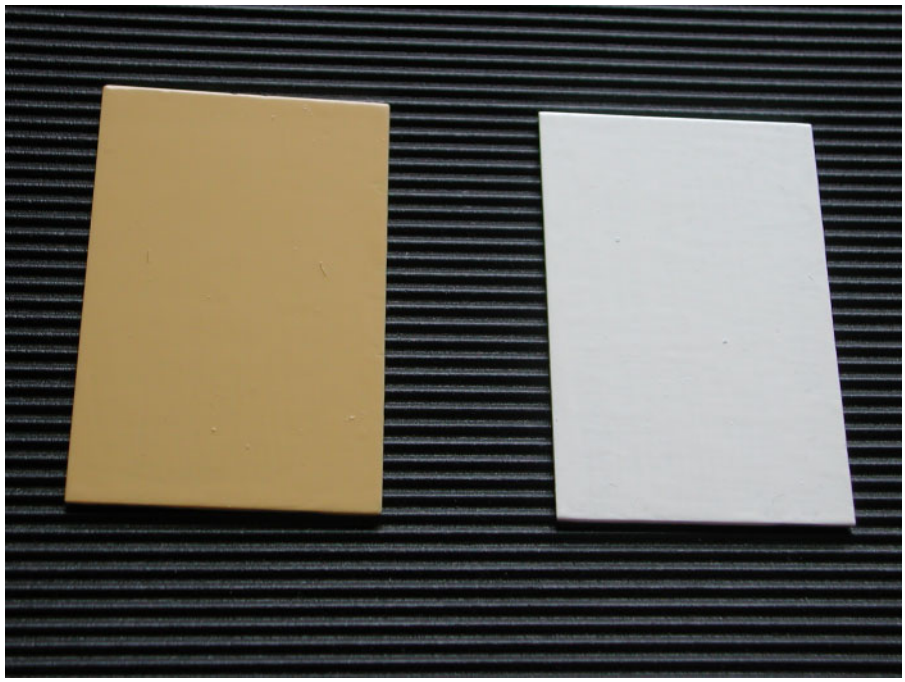

Figure D.1 Samples of the paint used on CFAV Quest

For the two paint samples total reflectance (diffuse + specular) is measured using an integrating sphere. In addition the specular reflectance is measured using an FTIR instrument.

D.1 Theory

Energy conservation on a flat surface tells us that (14)

$$\alpha + \rho + \tau = 1 \tag{D.1}$$

where

- α - absorbed fraction
- ρ - reflected fraction
- τ - transmitted fraction

Kirchoff's law states that $\alpha = \epsilon$, where ϵ is the emissivity defines as the ratio of the radiant emittance of the surface to the radiant emittance of a blackbody at the same temperature. Then for an opaque surface, $\tau = 0$ and

$$\epsilon = 1 - \rho \tag{D.2}$$

Perfectly diffuse surfaces obey Lambert's law: Reflected radiance is independent of angle. The general case is well treated with the concept of a BRDF (bi-directional reflectance distribution function), defined for a flat surface, dA, as:

$$f_r(\Theta_i, \phi_i, \Theta_r, \phi_r) \equiv \frac{dL_r(\Theta_r, \phi_r)}{dE_i(\Theta_i, \phi_i)} \tag{D.3}$$

where Θ and ϕ define ray directions, see figure D.2, and dE_i is the incident irradiance on dA and dL_r the reflected radiance from dA. The BRDF function is a ration of reflected radiance to incident irradiance, thus the units of BRDF is sr^{-1}, and can assume infinite values.

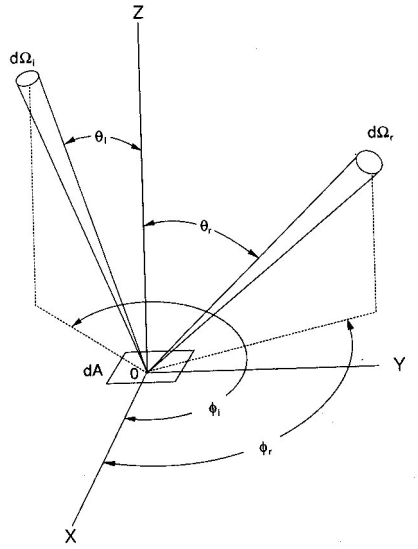

Figure D.2 Definition of incident and reflected directions

The total directional reflectance is related to BRDF but is defined as the ratio of two similar quantities, this ratio gives (14):

$$\rho_d(\Theta_i, \phi_i) = \int_{\text{hemisphere}} f_r \cos\Theta_r \, d\Omega_r \tag{D.4}$$

where

$d\Omega_r$ - element of solid angle in spherical coordinates

Helmholtz's reciprocity theorem shows no difference between incident and reflected directions:

$$\rho_d(\Theta_r, \phi_r) = \rho_d(\Theta_i, \phi_i) = \rho_d(\Theta, \phi) \tag{D.5}$$

The directional emissivity can be written as

$$\epsilon_d(\Theta, \phi) = 1 - \rho_d(\Theta, \phi) = 1 - \int_{\text{hemisphere}} f_r \cos\Theta \, d\Omega \tag{D.6}$$

For a perfectly diffuse surface ($\rho_d(\Theta, \phi) = \rho$) the BRDF is:

$$f_r = \frac{\rho}{\pi} \tag{D.7}$$

The directional emissivity for a perfectly diffuse surface viewed from any angle, or for perfectly specular surfaces viewed at angle (Θ, ϕ) is:

$$\text{diffuse:} \quad \epsilon_d = 1 - \rho \tag{D.8}$$

$$\text{specular:} \quad \epsilon_d = 1 - \rho_d(\Theta, \phi) \tag{D.9}$$

D.2 Total reflection

The total reflection (both specular and diffuse) is measured using an infrared spectroradiometer with an integrating sphere from Optronic Laboratories, model 746D.

Figure D.3 Optronics Laboratories infrared spectroradiometer model 746D

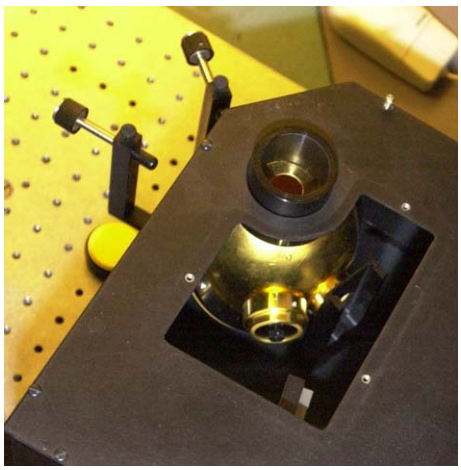

Figure D.4 Integrating sphere

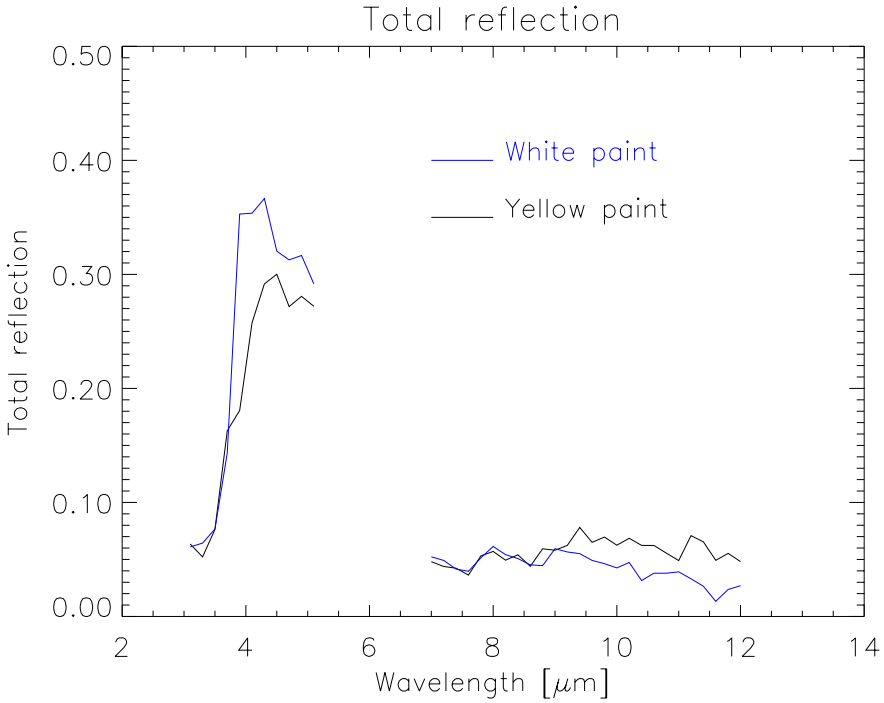

Figure D.5 Total reflection measured with integrating sphere

D.3 Specular reflection

The specular reflection is measured using an FTIR instrument, Perkin Elmer Spectrum GX Optica.

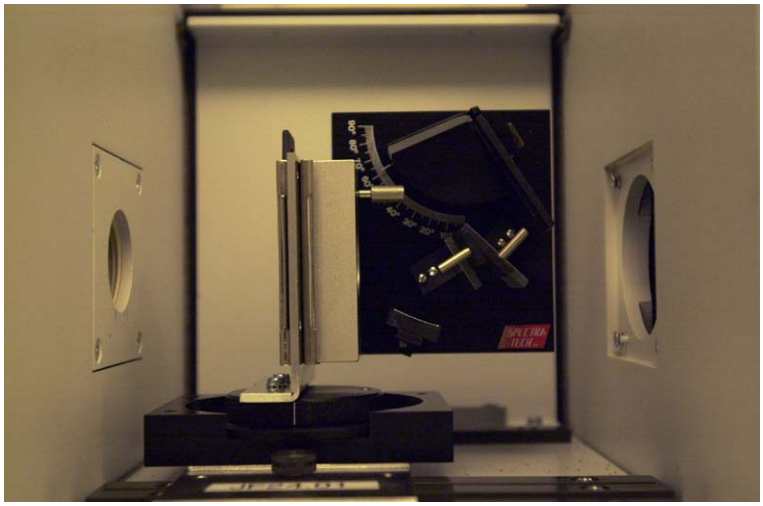

Figure D.6 Perkin Elmer Spectrum GX Optica, sample chamber close-up

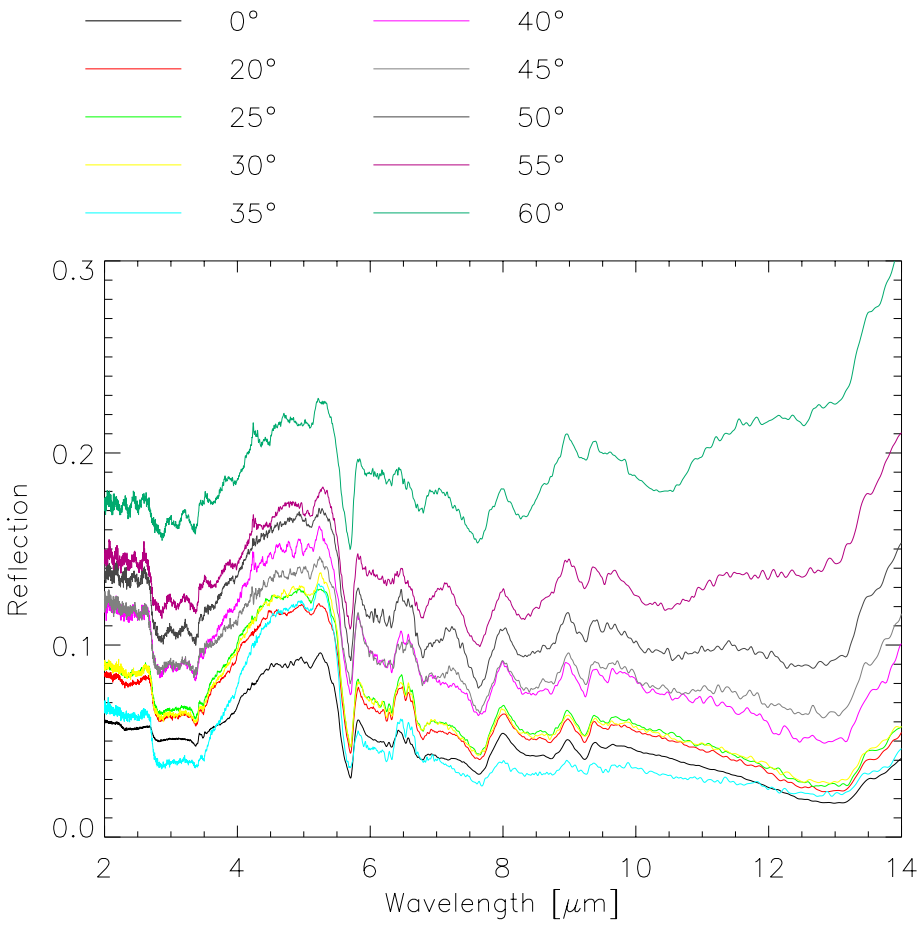

Figure D.7 Specular reflection measured on the white sample

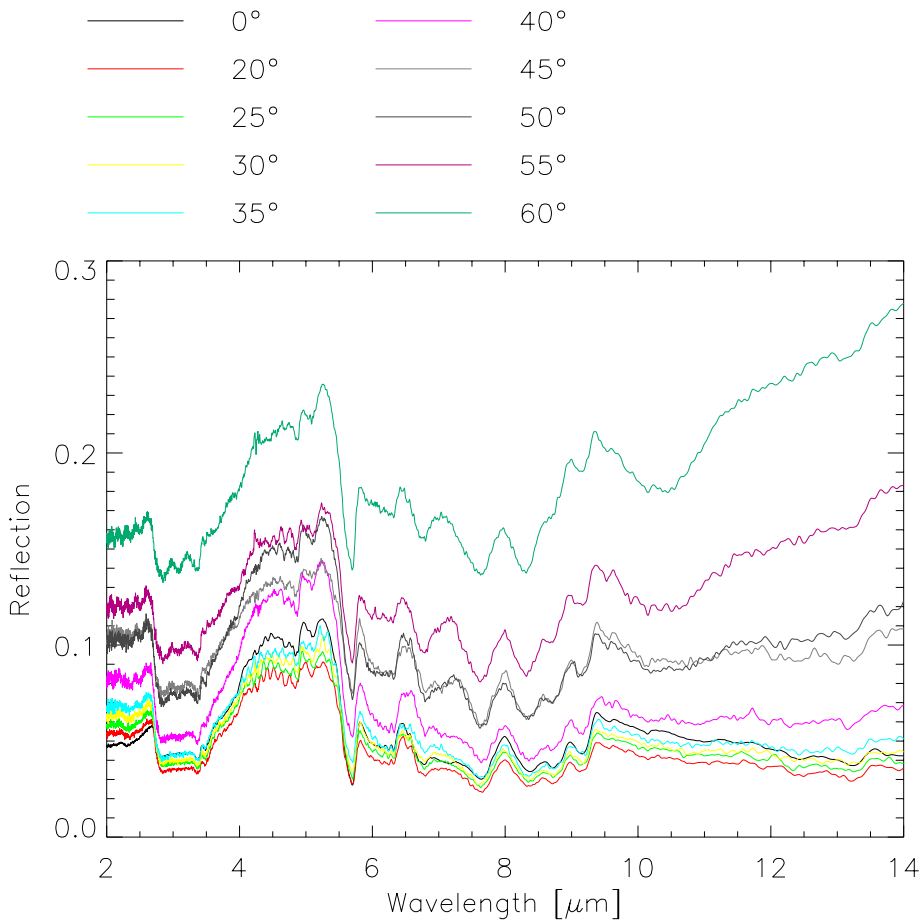

Figure D.8 Specular reflection measured on the yellow sample

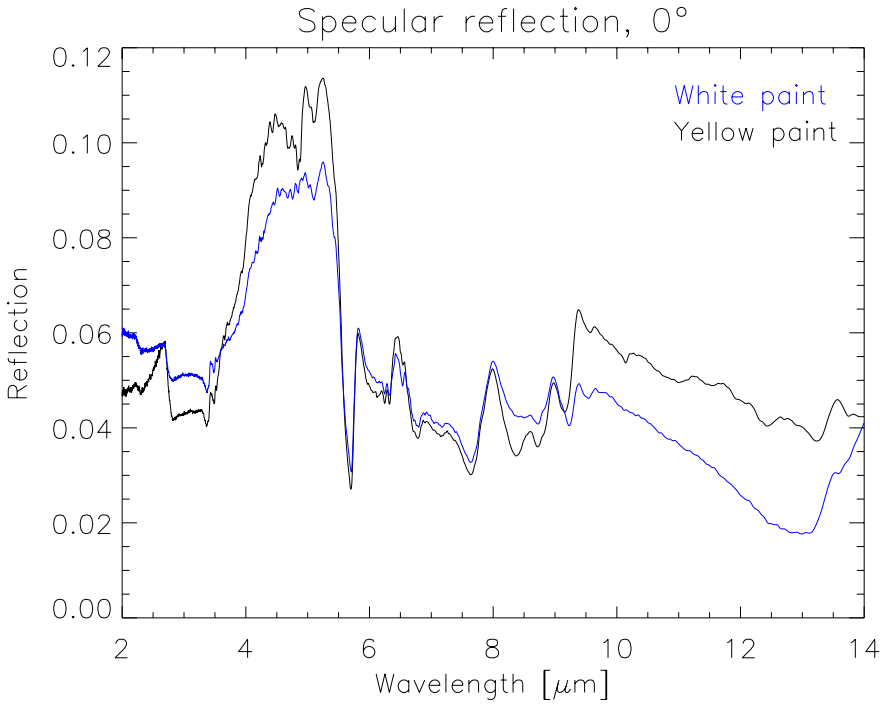

Figure D.9 Specular reflection at 0° angle

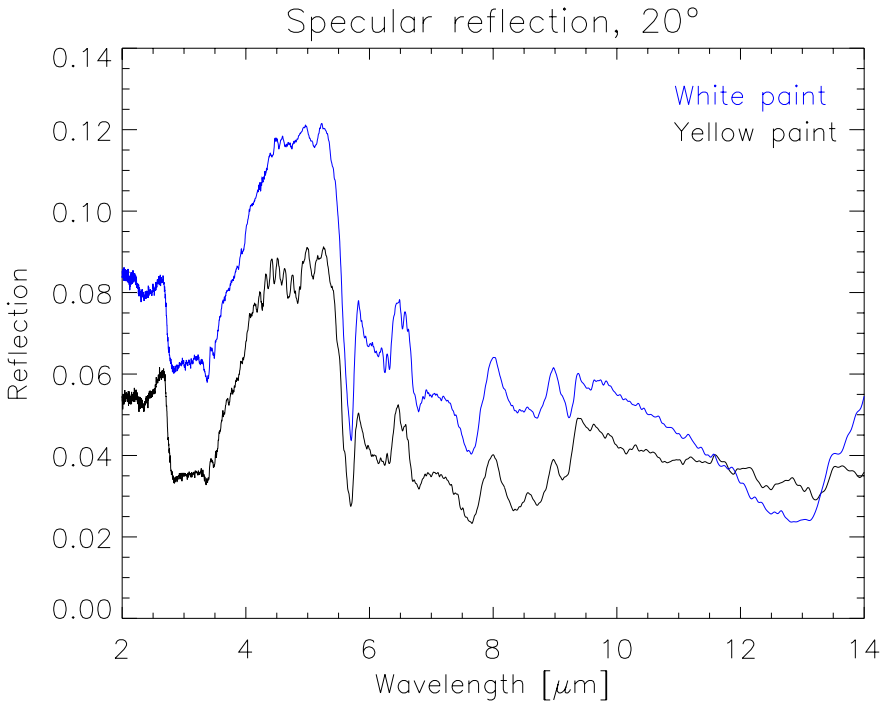

Figure D.10 Specular reflection at 20° angle

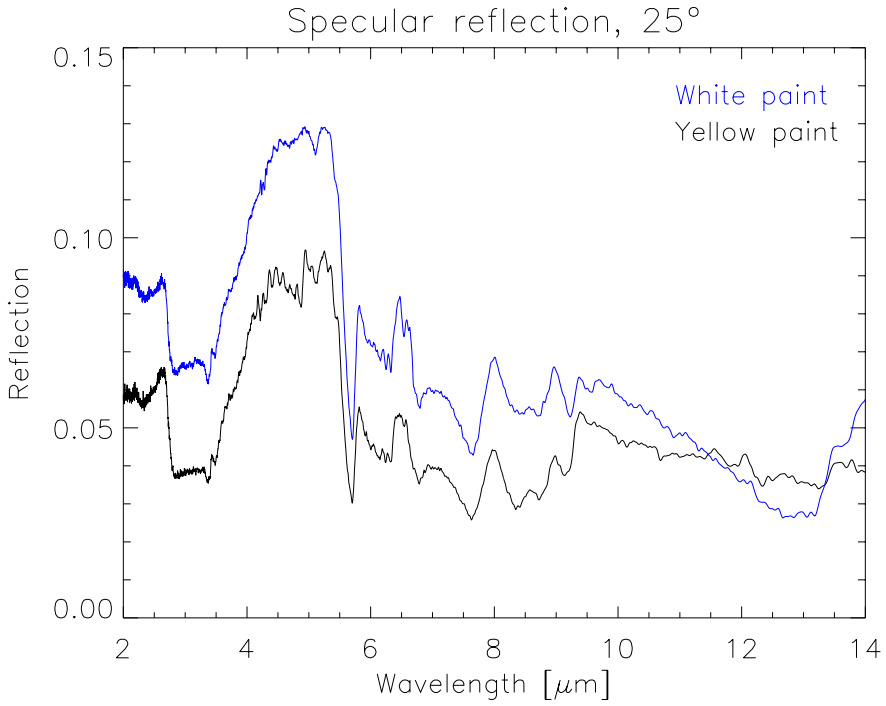

Figure D.11 Specular reflection at 25° angle

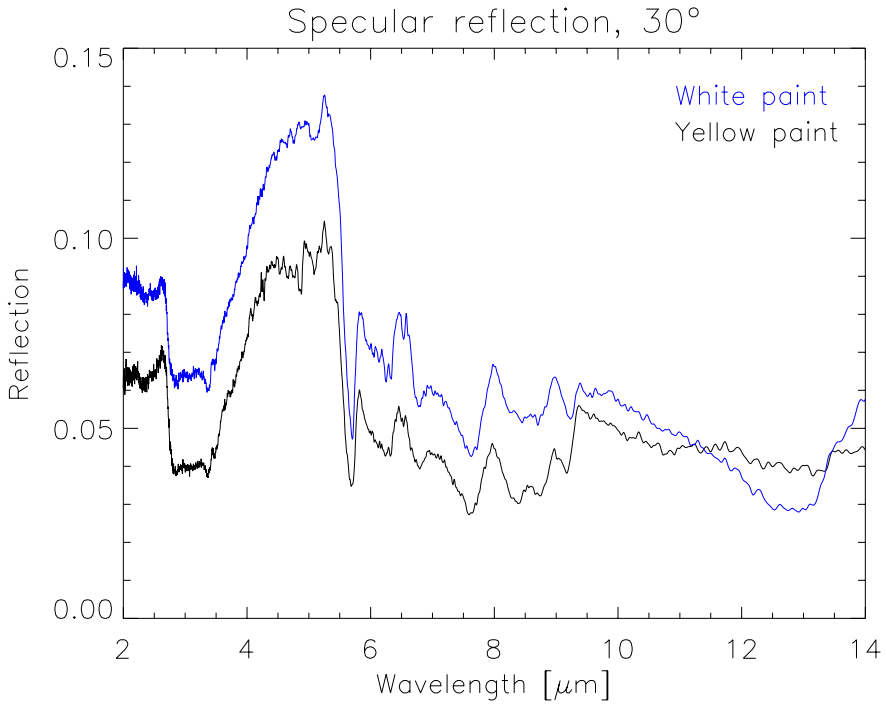

Figure D.12 Specular reflection at 30° angle

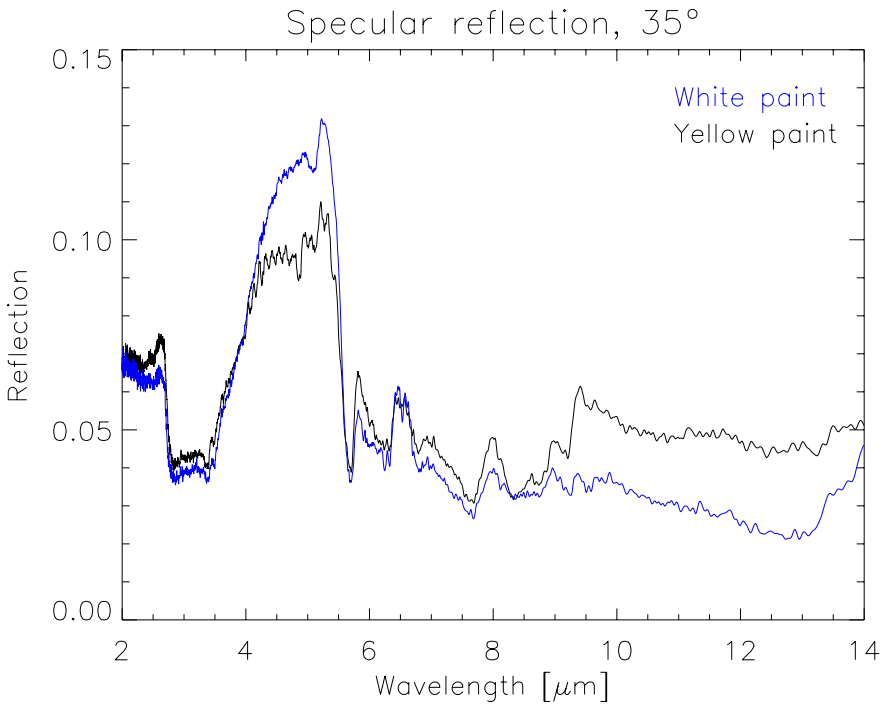

Figure D.13 Specular reflection at 35° angle

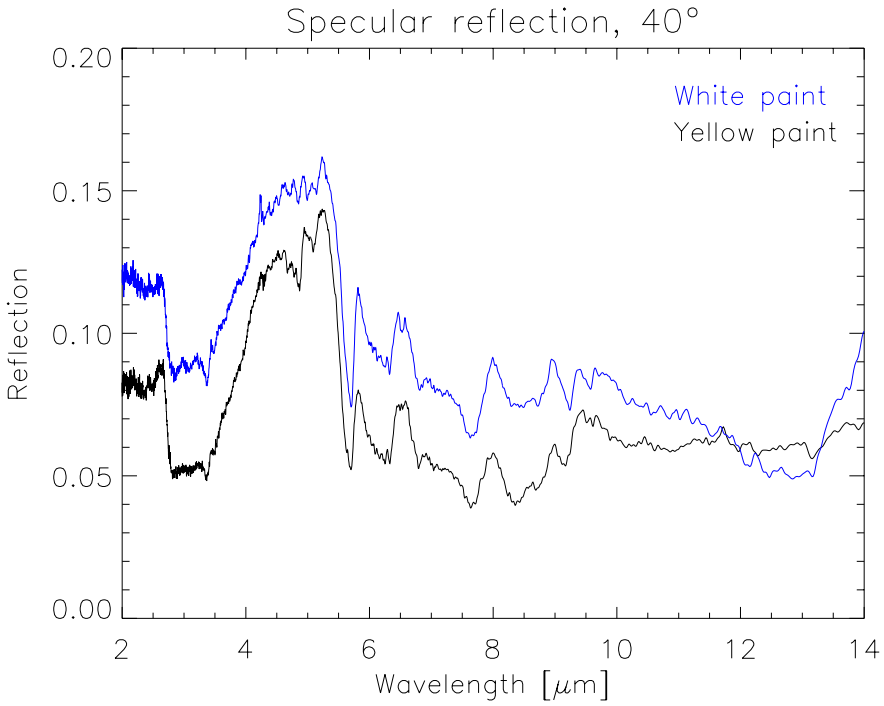

Figure D.14 Specular reflection at 40° angle

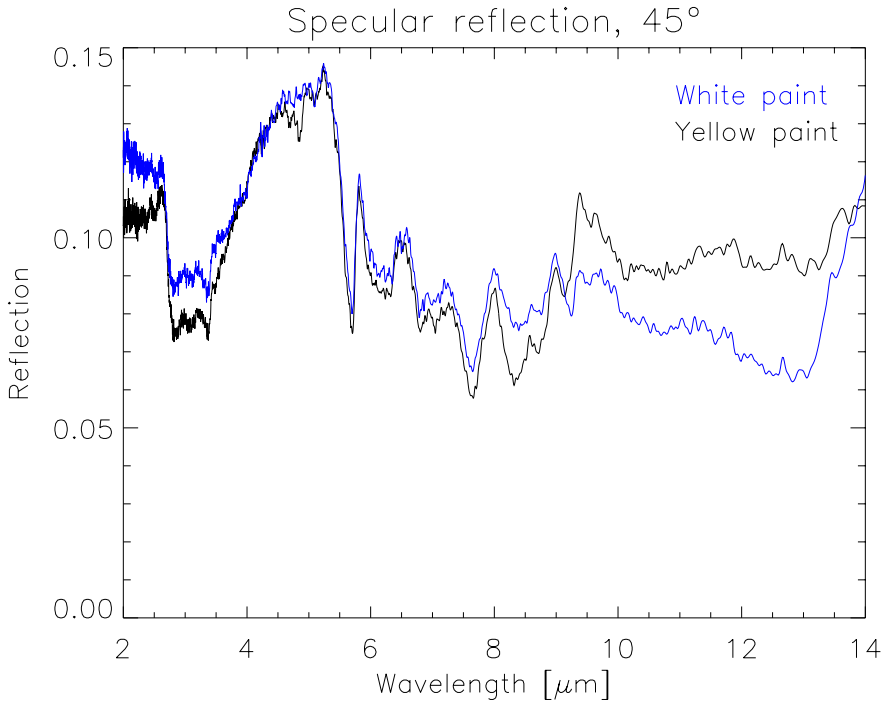

Figure D.15 Specular reflection at 45° angle

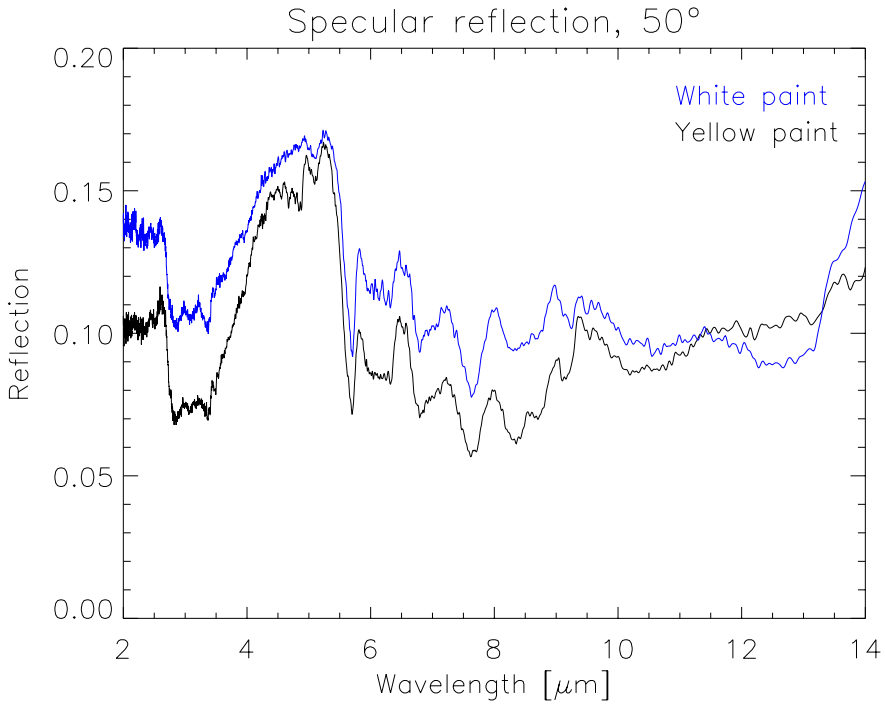

Figure D.16 Specular reflection at 50° angle

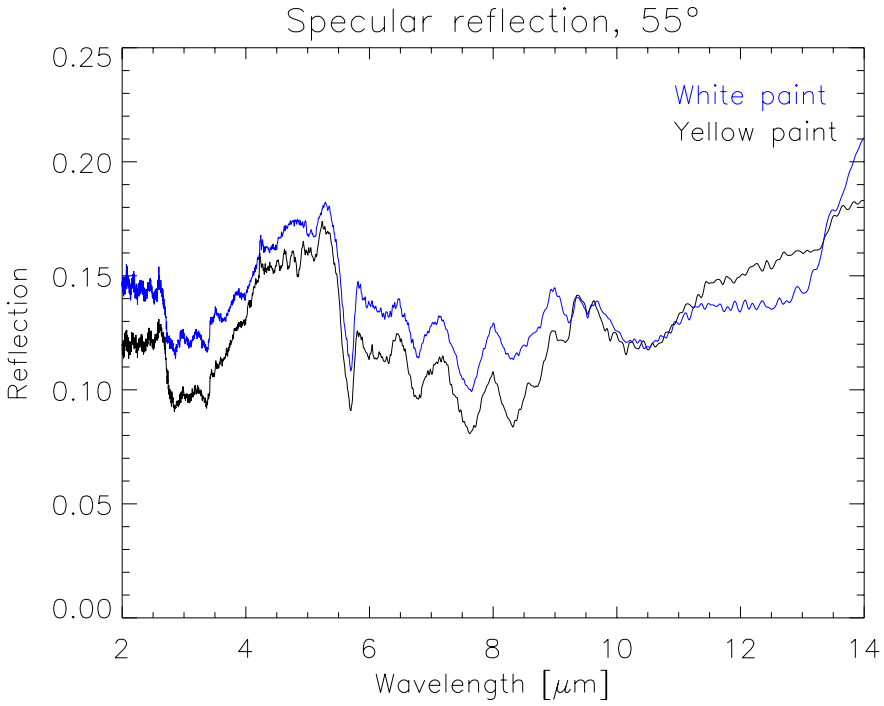

Figure D.17 Specular reflection at 55° angle

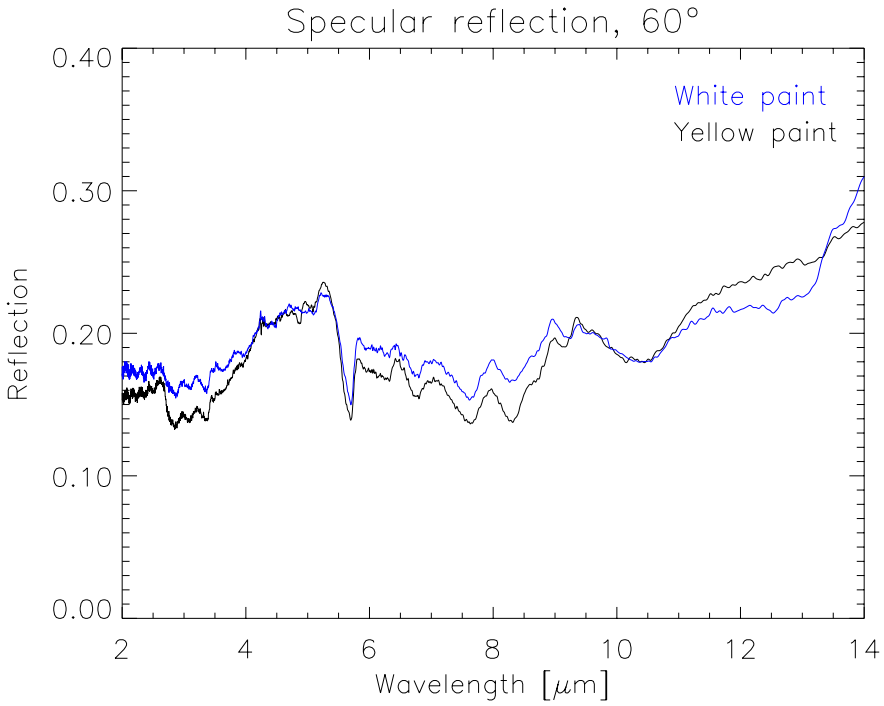

Figure D.18 Specular reflection at 60° angle

E LIST OF FIGURES AND LIST OF TABLES

LIST OF FIGURES

LIST OF TABLES

DISTRIBUTION LIST

FFIE **Dato:** 12th June 2002

RAPPORT TYPE (KRYSS AV)	RAPPORT NR	REFERANSE	RAPPORTENS DATO
X RAPP ☐ NOTAT ☐ RR	2002/02568	FFIE/801/131	12th June 2002
RAPPORTENS BESKYTTELSESGRAD: Ugradert		ANTALL EKS UTSTEDT: 75	ANTALL SIDER: 131
RAPPORTENS TITTEL: SIMVEX 2001 TRIAL - RADIANT INTENSITY CONTRAST		FORFATTER(E): STARK Espen, HEEN Lars Trygve, WIKAN Kjell	
FORDELINGEN GODKJENT AV FORSKNINGSSJEF:		FORDELINGEN GODKJENT AV AVDELINGSSJEF:	

EKSTERN FORDELING

ANTALL	EKS NR	TIL
1		FO/SST-Plan
1		v/Kom Jon Meyer
1		FLO/Sjø-T-VP
1		v/Kk Ove Rio
1		FO/LST-LTI
1		v/Oblt Inge Kampenes
1		KNM T/SMOPS
1		v/Kk Trond Hermansen
1		v/Kpt Lt Rune Crowo
1		FLO/Luft
1		v/Maj Geir Ove Nielsen
1		FO/E
1		v/Rådgiver Asgeir Berg
1		FLO/Sjø-P6026
1		v/Oing Jan Aasen
1		KDA
1		v/Halfdan Glørud
1		v/Birger C Kommedal
17		NATO RTO/SET/TG16
		www.ffi.no

INTERN FORDELING

ANTALL	EKS NR	TIL
14		FFIBIBL
1		Adm direktør/stabssjef
1		FFIBM
1		FFIE
1		FFISYS
1		FFIN
1		Stian Løvold, FFIE
1		Egil Bingen, FFIE
1		Espen Stark, FFIE
1		Øyvind Sjøvik, FFIE
1		Lars T Heen, FFIE
1		Kjell Wikan, FFIE
1		Erik Brendhagen, FFIE
1		Pål Steenfeldt-Foss, FFIE
1		Eirik Ralm, FFIE
1		Bernt Almklov, FFIE
1		Erling M Sunde, FFIE
1		Torbjørn Skauli, FFIE
1		Knut Stenersen, FFIE
1		Randi Haakenaasen, FFIE
1		Harald Hovland, FFIE
1		Frode B Olsen, FFIE
1		Morten Søderblom, FFIE
1		Emil Brodersen, FFIE
1		Oddvar Selnes, FFIE
2		Arkiv, FFIE
		wwwi

FFI-K1 Retningslinjer forfordeling og forsendelse er gitt i Oraklet, Bind I, Bestemmelser om publikasjoner for Forsvarets forskningsinstitutt, pkt 2 og 5. Benytt ny side om nødvendig.